Net Burgers Density Vector Fields in Crystal Plasticity: Characteristic Length Scales and Constitutive Validation

Abdulhamit Saraç

Submitted in partial fulfillment of the
Requirements for the degree
of Doctor of Philosophy
of the Graduate School of Arts and Sciences

Columbia University

2014

ABSTRACT

Net Burgers Density Vector Fields in Crystal Plasticity: Characteristic Length Scales and Constitutive Validation

Abdulhamit Saraç

This PhD thesis consists of five complementary chapters. Chapters 2 through 4 constitute the basis of research papers to be published subsequently. These three chapters summarize the state of a single crystal undergoing elastoplastic deformation. The studies presented in this thesis primarily deal with experimental and computational concepts that enable the calculation, measurement and extraction of the spatially resolved net Burgers density vector and the geometrically necessary dislocation densities (GNDs), which reveal the small scale continuum characteristics of a single crystal in the elastoplastic state. The calculation methodology of a new validation parameter, β, which is the orientation of the net Burgers density vector, is given in chapter 2. This new parameter, β, enables us to validate the elastic-plastic constitutive relations. Since the existing methods used for validation cannot give direct information about the state of the material, the β-variable is introduced for elastic-plastic constitutive models. β-fields, which are essentially contour maps of β-variables on two dimensional spatial coordinates, are used to monitor the activity regions of effective slip systems.

Chapters 2 through 4 present a comprehensive analysis of the spatially resolved net Burgers density vector, along with the length scale characterization of dislocation structures and validation of constitutive relations. The studies presented in this work are the outcome of experimental and computational research. The experimental work consists of the indentation of a nickel single crystal deformed through a quasi-statically applied line load parallel to the [110] crystallographic orientation. The line load was applied onto (001) surface of the single crystal by a tungsten carbide wedge indenter with a 90° included angle. A two-dimensional deformation field on an indented single crystal, in which the only non-zero lattice rotation occurs in the plane of deformation and only three effective in-plane slip systems are activated,

was investigated. The mid-section of the deformed single crystal was exposed by EDM and polished electrochemically. The in-plane lattice rotations were measured by high-resolution electron backscattered diffraction (HR-EBSD). The Nye's dislocation density components, lattice curvatures, GNDs and net Burgers density vectors were calculated. Therefore, the β-variable and the β-fields are calculated both experimentally, analytically and numerically in Chapter 2. A qualitative comparison of the three methods showed that the β-field obtained from experimental measurements agrees with those obtained from analytical and numerical methods. The directions of the net Burgers density vector, which are used to determine the boundaries of the slip activity regions, are also given in Chapter 2.

Chapter 3 mainly deals with the hardening parameters associated with strain hardening rules utilized in finite element simulations, and investigates the sensitivity of the β-variable to parameters such as latent hardening ratio, initial hardening modulus and saturation strength. The study revealed that a change in the saturation strength has a significant effect on both magnitude of the β-variable and the boundary of the slip activity regions.

Chapter 4 presents a length scale analysis associated with dislocation structures such as cell size and cell wall width. The methods presented in this chapter employ the SEM-based continuum method and Fourier Analysis. As-measured GNDs are extracted along the local crystallographic traces, and a quasi-periodic arrangement of dislocation structures is obtained. The extracted GND functions are truncated, interpolated, and filtered. Finally, Fourier Transform is applied to obtain a relationship between cell size and cell wall width of the dislocation structures. The results are compared with those obtained by TEM micrographs. Whereas TEM micrographs characterize the dislocation structures in small scale, the method that is presented in this chapter provides multi scale characterization, which is an order of magnitude larger.

Concluding remarks and recommendations for future studies are given in Chapter 5.

Contents

List of Figures

List of Tables

Acknowledgments

I thank my advisor, Professor Jeffrey Kysar, for giving me the opportunity to work in the Small Scale Mechanics Laboratory. Professor Kysar has provided continual support since I first began working on single crystal plasticity; his approach to challenging problems and the available resources in the Laboratory greatly enhanced my experimental and computational knowledge. I also thank my friends and colleagues Dr. Oya Okman, Dr. Muin Oztop, Dr. Mehmet Yilmaz, Dr. Ryan Cooper, Dr. Carl Dahlberg, Nastaran Ghazi, Dr. Hirobumi Watanabe, Chris DiMarco, Jaewon Moon, and Anna Ekberg, for sharing wonderful experiences, and the department of Mechanical Engineering at Columbia University.

I gratefully acknowledge the Ministry of National Education of Turkey for the financial support they have provided, and I thank my family for their lifelong support and encouragement.

Dedicated to My Family.

"Man's mind, once stretched by a new idea, never regains its original dimensions" Oliver Wendell Holmes

Chapter 1

Introduction

Existing validation methods in small scale mechanics comprise several tests: tensile, compression, torsion of thin wires [23], microindentation [68, 12], nanoindentation into a metal crystal [48, 49], nanoindentation on thin films [66], microbending of free standing films [69] and microhardness measurements [9, 18, 61]. These tests give the average response of a system via stress vs. strain history, force vs. displacement, torsion vs. twist, and moment vs. curvature relations. Since these existing methods cannot give direct information about the state of the material, the β-variable is introduced for the validation of elastic-plastic constitutive models and for the monitoring of slip system activities. The activity regions of the effective slip systems can be detected through the β-fields, which are essentially contour maps of β-variables on two dimensional spatial coordinates.

The spatially resolved net Burgers density vector obtained by SEM-based continuum methods is detailed in Chapter 2. This was investigated both experimentally and numerically by quantifying the β-variable and β-fields. The calculation of the net Burgers density vector starts with an accurate measurement of the non-zero lattice rotations in the plane of deformation, where only three effective in-plane slip systems are activated. High-resolution electron backscattered diffraction (HR-EBSD) is used to establish high accuracy in the measurement of lattice rotations on the deformed single crystal. The lattice curvature tensor was then

calculated by evaluating the spatial gradient of the in-plane lattice rotations. The gradient calculations were performed by numerically differentiating the in-plane lattice rotations with respect to the local crystallographic spatial coordinates. Two non-zero components of Nye's dislocation density tensor were obtained through the non-zero components of the lattice curvature tensor. Nye's dislocation density tensor serves as a link between plastic and elastic deformation states, and is the continuum manifestation of the Burgers circuit. Finally, the magnitude and orientation of the net Burgers density vector were obtained using the Nye's dislocation density tensor and the out-of-plane unit normal. Thence, the β-variable and the β-fields, were determined experimentally. Finite element simulations based on single crystal plasticity and strain hardening rules were performed to obtain β-fields that enable monitoring of the slip system activity regions. The hardening rules are given by two distinct hardening models, which are represented by PAN and BW. The β-fields obtained from the simulations were compared with those obtained experimentally, and consistency was observed between experimental and simulation results.

A parametric analysis was performed in Chapter 3 as a follow-up study, given in Chapter 2, to determine how the validation parameter β depends on the hardening parameters, in other words, how β is sensitive to the hardening parameters defined by the strain hardening rules. The effects of latent hardening ratio, initial hardening modulus and the saturation strength on the β-variable were investigated. Whereas Chapter 2 deals with the full analysis of the β-variable and the β-fields, Chapter 3 presents a finer analysis of the β-fields under the small scale yielding conditions. The effects of hardening parameters on the β-variable, the amount of plastic strain, the slip rate and the stress space were investigated in order to fully determine the deformation state of the single crystal subjected to extreme plastic deformation. Variations of the β-variable, plastic strains and the stresses are monitored along the ninety-degree arc lengths to obtain finer information about the state of the material. The analysis performed in Chapter 3 shows that the latent hardening ratio has no significant effect on the β-fields; especially, there is no change in the β-variable within regions near

the indenter tip that underwent extreme plastic deformation. The boundaries of the slip system activity regions in the β-fields shift as the initial hardening modulus and saturation strength vary. The effects of saturation strength on the magnitude of the β-variable and on the boundaries of the slip activity regions were observed. A ten-degree yield surface analysis was applied to understand the elastic and plastic deformation state of the material data points by employing the stress space. The potentially active slip systems obtained from the yield surface analysis were found to be consistent with those obtained from the analysis of the β-fields.

The length scale dependence of plastic deformation has been investigated by several researchers in light of the concept of geometrically necessary dislocation densities (GNDs) [5, 27, 20, 30, 31, 54, 14, 19, 29, 6, 33, 50, 56, 2, 11, 65, 1, 13, 32, 57, 3, 42, 53, 21, 22, 58]. GNDs are the dislocations, which are necessary to form a curvature of the crystal lattice and long-range stress fields by maintaining the compatibility of deformation fields in elastic-plastic materials. Since stress depends on the strain history and the spatial gradient of the strain, the lattice distortions introduce a characteristic length scale into macroscopic plastic deformation field.

To establish a connection between the dislocation formation and the macroscopic plastic deformation field, a length scale for the dislocation substructures of the nickel single crystal was investigated in Chapter 4. SEM-based continuum methods and Fourier Transform methods were used in the analysis. The nickel single crystal, which is deformed by applying a compressive line load through a wedge indenter, was investigated. Chapter 4 presents an investigation of characteristic length scale by following the same experimental procedures and data as used in Chapter 2 and Chapter 3. In addition to the calculation of the Nye's dislocation density components in Chapter 2, geometrically necessary dislocation densities (GNDs) are introduced in Chapter 4. SEM-based continuum methods were developed using the essential relations between Nye's dislocation density tensor and GND density.

The non-zero components of the Nye's dislocation density tensor were measured expe-

rimentally by taking advantage of high accuracy measurements (with the spatial resolution of 2500 nm, 500 nm and 100 nm) of High-Resolution Electron Backscatter Diffraction (HR-EBSD). GND densities were then measured for each effective in-plane slip system. The continuum fields of GND densities, which indicate quasi-periodic arrangements, and the spatial distribution of the net Burgers density vector were obtained. Three GND density functions associated with three effective slip systems were then extracted along the local crystallographic traces in the directions of the effective slip systems. The extraction of the data was performed with the help of the β-fields that were obtained in Chapter 2. As-measured GND density functions were truncated, interpolated and filtered properly before applying Fourier Transform. Finally, Fourier Transform was performed to calculate the dislocation cell size, dislocation spacing, and dislocation cell wall width. The relationships between dislocation cell size and peak GND density, dislocation cell size and dislocation spacing, and dislocation cell size and cell wall width were investigated. A linear relationship was obtained between these variables, and a length scale was defined. The length scale is compared qualitatively and quantitatively with the previously proposed TEM-based discrete methods. The results found in Chapter 4 using SEM-based continuum methods and Fourier Transform agree with those found by TEM-based discrete methods. The comparison shows that whereas TEM-based discrete methods characterize the dislocation densities only in a small length scale, the SEM-based continuum method is ideal for multiple scale characterization ranging from 2500 nm to 100 nm spatial resolution.

Chapter 2

Spatially Resolved Net Burgers Density Vector in a Deformed Single Crystal

2.1 Introduction

Existing methods, which are used for validation purpose such as tensile tests, compression tests, torsion tests, nanoindentation and hardness measurements, give the average response of a system. The average response of a system is mainly determined by the force vs. displacement curve or the stress-strain history. However, the actual deformed state of the material, in other words, the spatially resolved defects in the material cannot be obtained directly through these techniques.

Our objective is to define a new variable, β, for validation of elastic-plastic constitutive models in order to obtain direct information associated with the state of the material. To do so, a newly developed SEM and High Resolution Electron Back Scattered Diffraction (HR-EBSD) method was used to measure in-plane lattice rotations. The gradient of in-plane lattice rotation field gives the non-zero components of the lattice curvature tensor, which correspond to non-zero components of Nye's dislocation density tensor. Nye's dislocation tensor, which is a linear transformation of a unit tangent line vector to the net Burgers

density vector, serves as a linkage between elastic and plastic deformation. The orientation of the net Burgers density vector determines the newly defined β-quantity, and the spatially resolved β-fields, which quantifies the spatially resolved defect densities for a material in its deformed state. β-fields are also utilized to determine and characterize the slip system activities. The effects of the hardening parameters, which are introduced by two different hardening models, on the β-field were analyzed, and used experimental data as a benchmark.

The paper is organized as follows. The theoretical background of the net Burgers density vector including the calculation of its magnitude and orientation is discussed in Section 2.2. Section 2.3, experimental background, mainly deals with the deformed and undeformed configuration of the specimen, experimental setup and understanding of the crystallographic and effective in-plane slip systems. The representation and orientation of effective slip systems are summarized and illustrated in Section 2.3. The finite element model with relevant parameters is briefly described in Section 2.4. Two different hardening models, which are used in the finite element simulations, are described. The hardening parameters associated with the hardening models are defined and listed in Subsection 2.4.1. The β-fields pertaining to the experiment and finite element simulations, which employ different hardening models, are presented and discussed in Section 2.5. Concluding remarks are given in Section 2.6.

2.2 Theoretical Background

Metals are known to have crystal structures defined by periodic arrangement of atoms. A small representation of the periodic arrangement of metal atoms on the sub-micron scale, is shown in Fig. 2.1(a). The circuit enclose a region starting from point **S** and finishing at point **F**. By introducing an extra half plane of atoms the lattice equilibrium positions will change, as shown in Fig. 2.1(b), and the circuit becomes disconnected. In order to close the circuit, a vector, **b**, is drawn starting from **S** to **F**. This vector is called Burgers vector, and it represents the amount of slip due to a single dislocation (i.e. the atomic half plane).

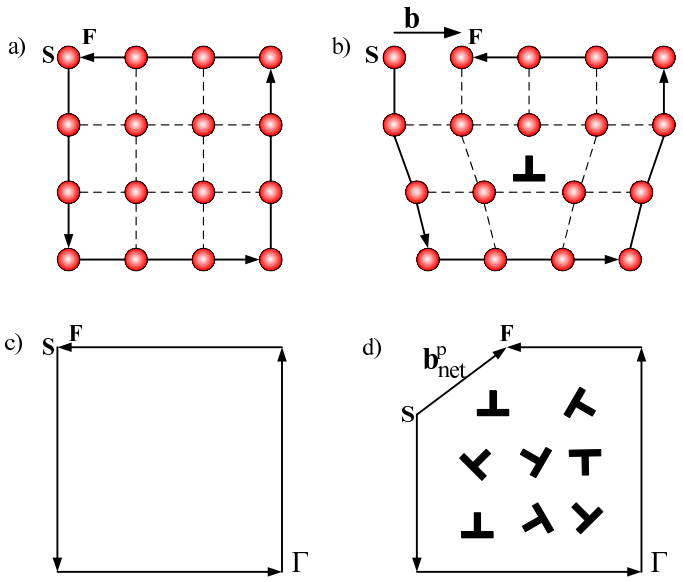

Figure 2.1: Crystal lattice and the Burgers circuits: (a) Crystal lattice without any dislocation, (b) Crystal lattice with a single dislocation and the Burgers vector, $\mathbf{b}$, (c) Crystal body bounded by Γ circuit, (d) Crystal body with multiple dislocations and the net Burgers vector, $\mathbf{b}^p_{net}$.

When we zoom out to take a larger area into consideration, we enclose it by circuit Γ and introduce several dislocations, as illustrated in Fig. 2.1(c). As a result, the gap between **S** and **F** is closed by the net Burgers vector. It is shown in Fig. 2.1(d) as $\mathbf{b}^p_{net}$ which represents the net signed dislocations. The net Burgers vector density, also called the *net closure failure density*, is obtained by normalizing the net Burgers vector by A, which is the area within Γ. The net Burgers vector density, $B = \frac{b^p_{net}}{A}$, is measurable using discrete methods via TEM. The net Burgers density vector can be quantified as

$$\mathbf{B} = \alpha \cdot \boldsymbol{\ell}, \tag{2.1}$$

where α is Nye's tensor (also called dislocation density tensor), and $\boldsymbol{\ell}$ is the out-of-plane unit normal vector when the Burgers circuit, Γ, is taken in a right-hand sense. The dislocation density tensor is a measure of incompatibility serving as a link between the elastic deformation and plastic deformation of the crystal. It can be expressed in terms of the elastic

deformation

$$\alpha_{ji} = -\kappa_{ij} + \delta_{ij}\kappa_{kk} + e_{ipk}\epsilon^{el}_{jk,p}, \tag{2.2}$$

where κ_{ij} is the lattice curvature tensor, δ_{ij} is the Kronecker delta, e_{ipk} is the permutation tensor, $\epsilon^{el}_{jk}$is the elastic strain of the crystal lattice, and $\epsilon^{el}_{jk,p}$ is the elastic strain gradient. The magnitude of the components of the elastic strain gradient is significantly less than the magnitude of the lattice curvatures in Eq. (2.2). As a result, the elastic strain gradient is negligible considering a plane strain deformation state and finite deformation kinematics, as shown by Kysar et al. [46]. The lattice curvatures are basically the lattice rotation gradients which can be calculated via numerical differentiation of the lattice rotation measurements with respect to the global or reference coordinate frame, and can be denoted as

$$\kappa_{ij} = \frac{\partial \omega_i}{\partial x_j} \qquad i, j = 1, 2, 3. \tag{2.3}$$

The lattice rotations about x_1-, x_2-, and x_3-axes are represented by ω_1, ω_2, and ω_3, respectively. For the plane strain deformation state we make the approximation to assume out-of-plane lattice rotations, ω_1 and ω_2, are negligible comparing to ω_3, that is $\omega_1 = \omega_2 = 0$. The nonzero components of the lattice curvature tensor are obtained from the in-plane lattice rotation, ω_3. Lattice orientations are measurable via High Resolution Electron Backscatter Diffraction (HR-EBSD) or other methods such as X-ray microbeam diffraction, Orientation Imaging Microscopy [4] and Transmission Electron Microscopy [17]. Then, the matrix representation of the non-symmetric lattice curvature tensor will be

$$\kappa = \begin{bmatrix} 0 & 0 & 0 \\ 0 & 0 & 0 \\ \kappa_{31} & \kappa_{32} & 0 \end{bmatrix}, \tag{2.4}$$

where $\kappa_{31} = \frac{\partial \omega_3}{\partial x_1}$ and $\kappa_{32} = \frac{\partial \omega_3}{\partial x_2}$, respectively. It is obvious that the trace of the lattice curvature tensor, κ_{kk}, is zero. By considering the plane strain deformation state, Eq. (2.2),

which is also called elastic incompatibility equation, can be reduced to Eq. (2.5), which is expressed as

$$\alpha_{ji} \approx -\kappa_{ij}. \tag{2.5}$$

Consequently, the non-zero components of the dislocation density tensor in the reference coordinate frame are $\alpha_{13} \approx -\kappa_{31}$ and $\alpha_{23} \approx -\kappa_{32}$. These components are measurable through continuum methods via SEM. Then, the Nye's dislocation density tensor can now be written in the reference coordinate frame as

$$\alpha = \begin{bmatrix} 0 & 0 & -\kappa_{31} \\ 0 & 0 & -\kappa_{32} \\ 0 & 0 & 0 \end{bmatrix}. \tag{2.6}$$

By applying a coordinate transformation to Eq. (2.6) one can obtain the Nye's dislocation density tensor in a local crystallographic coordinate frame as

$$\alpha^{'}_{ij} = m_{ik} m_{jl} \alpha_{kl}, \tag{2.7}$$

where α_{kl} is the Nye's dislocation density tensor in the reference coordinate frame, and m_{ij} is the coordinate transformation tensor which has the following matrix representation

$$m = \begin{bmatrix} \cos\omega_3 & \sin\omega_3 & 0 \\ -\sin\omega_3 & \cos\omega_3 & 0 \\ 0 & 0 & 1 \end{bmatrix}.$$

Following the transformation law for second-rank tensors described by Eq. (2.7), the non-zero components of the Nye's dislocation density tensor in the local crystallographic coordinate frame, $\alpha^{'}_{ij}$ can be expressed as

$$\alpha'_{13} = \alpha_{13}\cos\omega_3 + \alpha_{23}\sin\omega_3 \tag{2.8a}$$

$$\alpha'_{23} = -\alpha_{13}\sin\omega_3 + \alpha_{23}\cos\omega_3. \tag{2.8b}$$

We now turn our attention back to the Eq. (2.1) to determine the magnitude and the direction of net Burgers density vector, $\mathbf{B}$, which will be defined in the local crystallographic coordinate frame. In this case, the out-of-plane unit normal vector is in the direction of $x_3^{'}-$ axis, that is $\boldsymbol{\ell}=\hat{\boldsymbol{e}}_{\mathbf{3}}^{\boldsymbol{\prime}}$. By substituting Eq. (2.8) and $\boldsymbol{\ell}$ into the Eq. (2.1), the net Burgers density vector can be quantified as

$$\mathbf{B} = \begin{bmatrix} 0 & 0 & \alpha_{13}^{'} \\ 0 & 0 & \alpha_{23}^{'} \\ 0 & 0 & 0 \end{bmatrix} \begin{bmatrix} 0 \\ 0 \\ 1 \end{bmatrix} = \begin{bmatrix} \alpha_{13}^{'} \\ \alpha_{23}^{'} \\ 0 \end{bmatrix},$$

and can be written in vector form as

$$\mathbf{B} = \alpha_{13}^{'}\hat{\mathbf{e}}_{\mathbf{1}}^{\prime} + \alpha_{23}^{'}\hat{\mathbf{e}}_{\mathbf{2}}^{\prime}. \tag{2.9}$$

Hence, the magnitude of the net Burgers density vector is $B = \sqrt{(\alpha_{13}^{'})^2 + (\alpha_{23}^{'})^2}$, and it has the units of length/area or 1/lengths. The orientation angle of the net Burgers density vector can be defined as

$$\beta = \arctan(\frac{\alpha_{23}^{'}}{\alpha_{13}^{'}}). \tag{2.10}$$

This newly introduced quantity is called the β-variable, and is used to monitor the activity of effective slip systems in the deformed region. The plots illustrating these characteristic regions are called the β-fields. Orientation of the effective in-plane slip systems and the net Burgers density vector in local crystallographic coordinate frame is shown in Fig. 2.2. The range of β and potentially active effective slip systems in those specific ranges are listed in Table 2.1.

2.3 Experimental Background

A high purity rectangular parallelepiped nickel single crystal with 1 cm edges was used as a specimen. In order to indent the specimen a line load parallel to the [110] direction of the crystal specimen was applied into the (001) surface of the specimen by a tungsten carbide

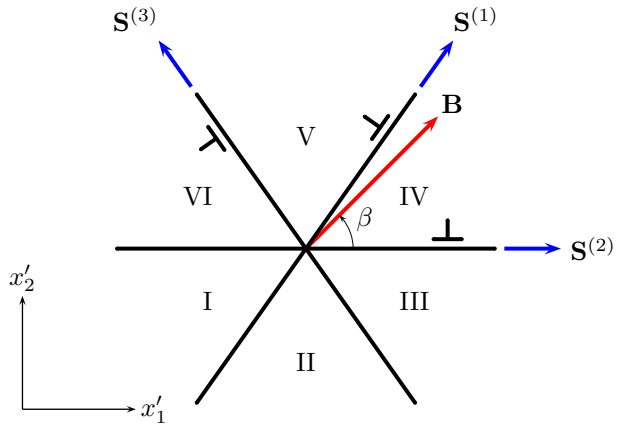

Figure 2.2: Orientation of effective in-plane slip systems and net Burgers density vector in local crystallographic coordinate frame. Coordinate frame is divided into six sectors that represent the ranges of β.

Table 2.1: The range of β and potentially active effective slip systems in that specific range. This table provides information to interpret the β-fields. If β equals to the characteristic slip orientation angles such as $-125.3°$, $-54.7°$, $0°$, $54.7°$, $125.3°$ and $180°$, then a single slip system is expected to be activated; if β is in a sector, then two slip systems are expected to be activated.

Sector	Range of β	Potentially active effective slip systems
I	$-180° < \beta < -125.3°$	-1,-2
	$\beta = -125.3°$	-1
II	$-125.3° < \beta < -54.7°$	-1,-3
	$\beta = -54.7°$	-3
III	$-54.7° < \beta < 0°$	-2,-3
	$\beta = 0°$	2
IV	$0° < \beta < 54.7°$	1,2
	$\beta = 54.7°$	1
V	$54.7° < \beta < 125.3°$	1,3
	$\beta = 125.3°$	3
VI	$125.3° < \beta < 180°$	2,3
	$\beta = 180°$	-2

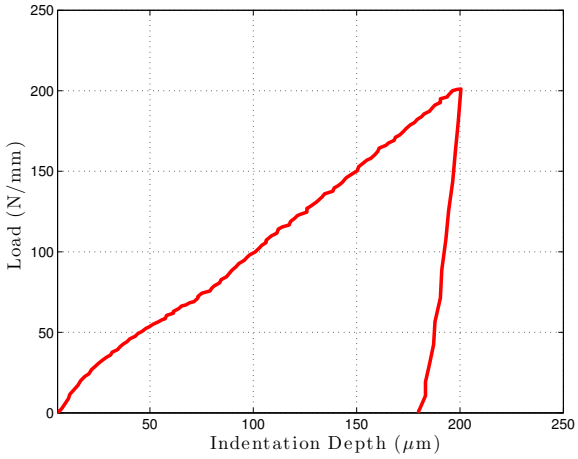

Figure 2.3: Force as a function of displacement.

wedge indenter with an included angle of 90°. The nominal total depth of indentation was $\sim$ 200μm, and after unloading the final indentation depth was measured as $\sim$ 160μm, which is very small compared to the dimensions of the specimen so as to maintain small scale yielding conditions. The force vs. displacement relation was measured during the indentation process as shown in Fig. 2.3.

The *crystallographic slip systems* in an FCC single crystal are known to be in the [110] directions and on {111} close packed planes. The smallest possible perfect dislocation Burgers vector is $\frac{1}{2}[110]$ and its magnitude is $b = a/\sqrt{2}$, where a is the lattice parameter (e.g. Hirth and Lothe [35]). The *effective in-plane slip systems* is preferably used in this study to distinguish the *crystallographic slip systems* from the slip systems created in (110) plane under the load which is applied parallel to the [110] direction. The orientations of *crystallographic slip systems* and *effective in-plane slip systems* are explained by Kysar et al. [46] and Kysar et al. [45].

Prior to the deformation analysis, the relation between the *crystallographic slip systems* and the *effective in-plane slip systems* must be well understood. Rice [64] showed that under the application of a line load in [110] directions into the surface of (001)-planes, and under the assumption of having the same critical resolved shear stress (τ_{CRSS}), *crystallographic slip systems* $(1\bar{1}1)[\bar{1}01]$ and $(1\bar{1}1)[011]$ will be activated in equal amounts by experiencing

the same resolved shear stress. These coplanar slip systems combine to form an effective slip system on the $(1\bar{1}1)$ plane in the direction of $[\bar{1}12]$. The resulting effective slip system is called *Slip System 1*, and the unit slip vector of the *Slip System 1* is denoted as $\mathbf{S}^{(1)}$, which is oriented at an angle of $\phi_1 = 54.7°$. *Crystallographic slip systems* $(111)[\bar{1}10]$ and $(\bar{1}\bar{1}1)[\bar{1}10]$ experience the same resolved shear stress under the identical conditions described above. These collinear slip systems combine to form an effective slip system, *Slip System 2*, on effective (001) planes and $[\bar{1}10]$ slip direction. The unit vector of *Slip System 2* is denoted as $\mathbf{S}^{(2)}$ and is oriented at an angle of $\phi_2 = 0°$. Similarly, the $(1\bar{1}\bar{1})[101]$ and $(1\bar{1}\bar{1})[0\bar{1}1]$ *crystallographic slip systems* experience the same resolved shear stress, and combine to form the effective in-plane slip system which is called *Slip System 3*. This effective slip system is activated on $(1\bar{1}\bar{1})$ plane and in the direction of $[1\bar{1}2]$. The unit vector of *Slip System 3* is denoted as $\mathbf{S}^{(3)}$ and is oriented at an angle of $\phi_3 = 125.3°$. Activation of the remaining slip systems on the (110)-planes will occur only due to any misalignment of the experimental set up, or subsequent large out-of-plane deformation and will slip in a very small amount relative to the slip systems described above. Therefore, these *crystallographic slip systems* are considered to have no contribution during plane strain plastic deformation (e.g. Kysar et al. [45] and Kysar et al. [46]). The single crystal specimen before and after the indentation process and the *effective in-plane slip systems* are illustrated in Fig. 2.4.

The unit slip vectors, $\mathbf{S}^{(\alpha)}$, slip orientations $\phi^{(\alpha)}$, and geometric parameters, $\lambda^{(\alpha)}$ are listed in Table 2.2. The relation between the unit slip vector in each effective slip system, $\mathbf{S}^{(\alpha)}$ and the unit slip plane normal to each effective slip plane, $\mathbf{N}^{(\alpha)}$ is defined as $\mathbf{N}^{(\alpha)} = \mathbf{T}^{(\alpha)} \times \mathbf{S}^{(\alpha)}$, where $\mathbf{T}^{(\alpha)}$ is the unit tangent line vector for each of the three effective in-plane dislocations is taken in the positive $x_3^{'}$-axis direction. The directions of $\mathbf{S}^{(\alpha)}$ are relative to the local crystallographic coordinate frame. The magnitude of the crystallographic Burgers vector, b, is the same for each effective slip system.

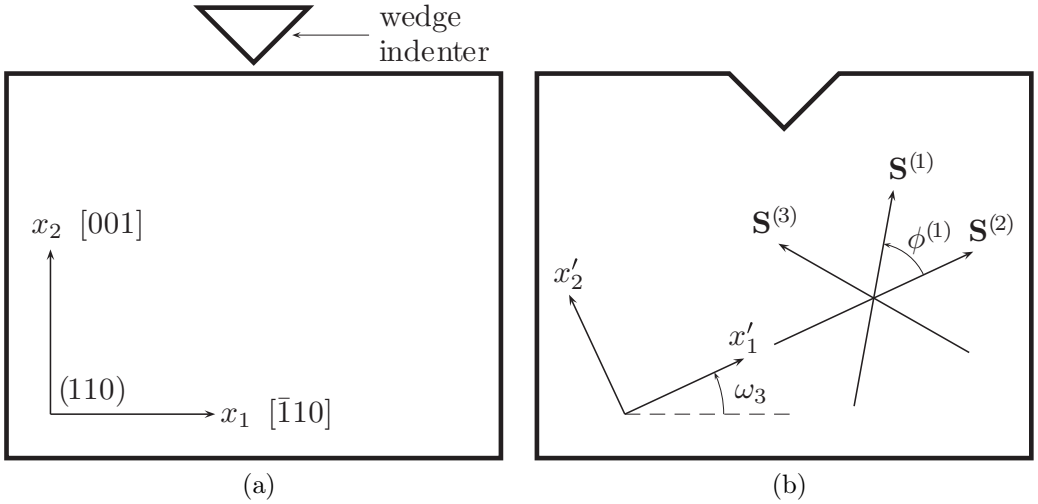

Figure 2.4: The single crystal specimen before and after the indentation process: (a) Orientation of nickel single crystal specimen in reference (global) coordinate frame, (b) Orientation of effective slip systems in local crystallographic coordinate frame.

Table 2.2: Unit slip vectors and orientations of effective plane strain slip systems in FCC crystal expressed in local coordinate frame. The effective unit tangent vector is $\mathbf{T}^{(\alpha)} = \hat{\mathbf{e}}_3'$ for each effective slip system.

Slip system: α	Unit slip vector: $\mathbf{S}^{(\alpha)}$	Orientation of slip systems: $\phi^{(\alpha)}$	Geometric parameter: $\lambda^{(\alpha)}$
1	$\mathbf{S}^{(1)} = \sqrt{\frac{1}{3}}\hat{\mathbf{e}}_1' + \sqrt{\frac{2}{3}}\hat{\mathbf{e}}_2'$	$\phi^{(1)} = 54.7^\circ$	$\frac{2}{\sqrt{3}}$
2	$\mathbf{S}^{(2)} = \hat{\mathbf{e}}_1'$	$\phi^{(2)} = 0^\circ$	$\sqrt{3}$
3	$\mathbf{S}^{(3)} = -\sqrt{\frac{1}{3}}\hat{\mathbf{e}}_1' + \sqrt{\frac{2}{3}}\hat{\mathbf{e}}_2'$	$\phi^{(3)} = 125.3^\circ$	$\frac{2}{\sqrt{3}}$

2.4 Finite Element Simulation

A series of finite element simulations were performed to analyze the elastic-plastic behavior of a nickel single crystal which is deformed through a wedge indentation process. The finite element analysis was carried out using a commercial software package (ABAQUS/Standard, v.6.10) by employing a UMAT, user-material subroutine, for single crystal plasticity written by Huang [37] and modified by Kysar [43]. The objectives of the finite element analysis are to determine the slip system activities in the deformed domain, obtain the β-field to characterize the spatial distribution of the net Burgers density vector, and analyze the influence of the different hardening parameters on the β-field. The hardening parameters are introduced by two hardening models that will be explained in detail under Subsection 2.4.1.

Only the portion of the specimen to the right of the midline was modeled by using plane strain bi-linear four-noded quadrilateral elements. The geometry of the wedge indenter and the undeformed single crystal specimen is illustrated in Fig. 2.5(a). A 90°-angle wedge indenter with a 100 μm radius of curvature at the tip was modeled as a line segment. A small portion of the deformed mesh immediately under the wedge indenter is shown in Fig. 2.5(b). Nodal displacements in the x_2-direction were constrained to be zero at the base of the specimen, and the nodal displacements in the x_1- direction were constrained to be zero on the midline.

Anisotropic elastic properties for nickel (C_{11} = 246.5 GPa, C_{12} = 147.3 GPa, and the C_{44} = 124.7 GPa) were used (Hirth and Lothe [35]). Two phenomenological hardening models with the hardening parameters listed in Table 2.3 and Table 2.4 were employed in the finite element simulations. The indenter was modeled as a rigid body and displaced quasi-statically into the meshed region. The coefficient of friction between the indenter and the material surface was set to 1.

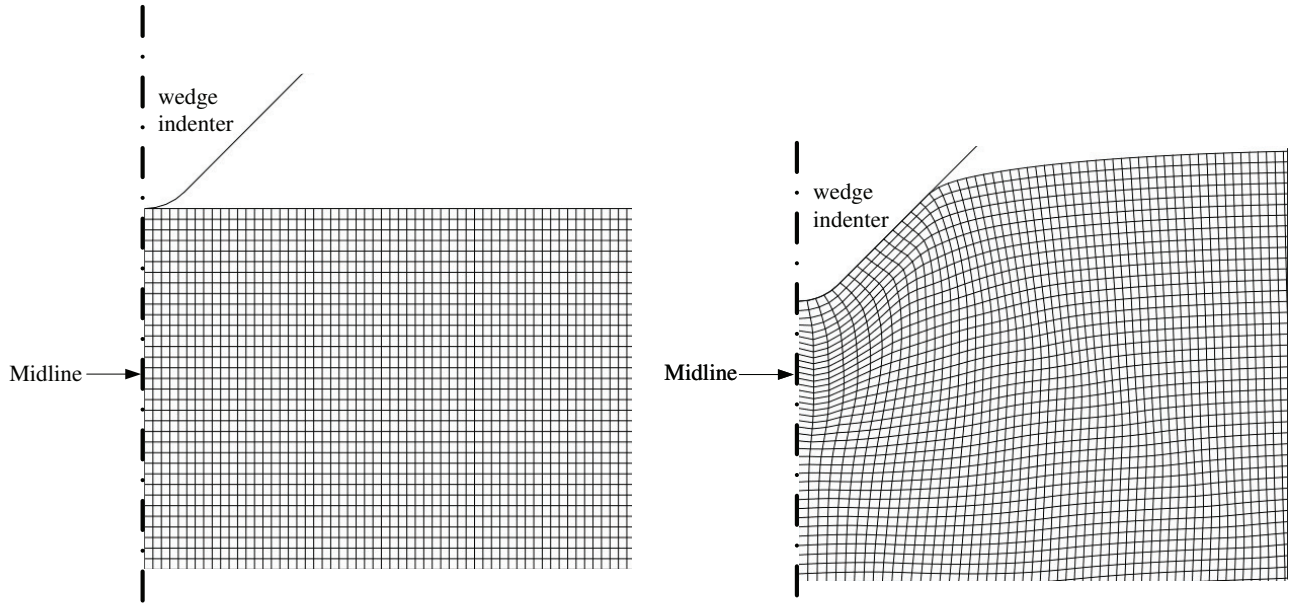

Figure 2.5: Finite element mesh: (a) geometry of mesh and rigid indenter; (b) deformed mesh after the indentation process

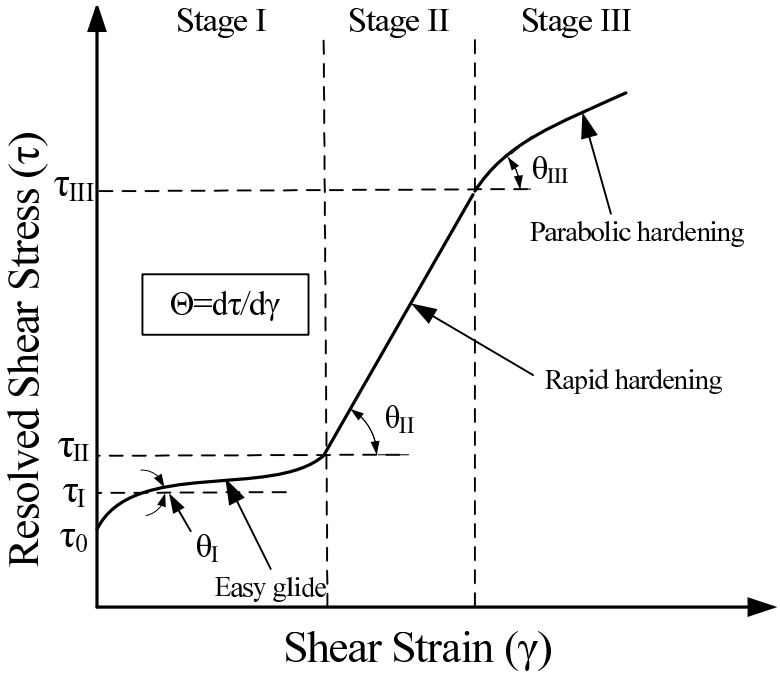

Figure 2.6: Hardening stages in an FCC single crystal based upon Wu et al. [70]: Easy glide, Rapid hardening and Parabolic hardening

2.4.1 Hardening Models

Hill [34] showed that the hardening rate of each slip system is a function of the slip rate on all systems. In other words, the hardening rate, $\dot{\tau}$, on each slip system α is described by

$$\dot{\tau}^{(\alpha)} = \sum_{\beta=1}^{N} h_{\alpha\beta}\dot{\gamma}^{(\beta)}, \tag{2.11}$$

where N is the total number of slip systems, $\dot{\gamma}$ is the slip rate and $h_{\alpha\beta}$ is the hardening moduli matrix which is determined by different hardening models. The first phenomenological hardening model used in the present work was introduced by Pierce, Asaro, and Needleman [59], which will be referred to as the PAN hardening model. The second one was introduced by Bassani and Wu [10], which will be referred to as the BW hardening model.

The PAN model proposes two hardening moduli,

$$h_{\alpha\alpha} = h(\gamma) = h_0 \operatorname{sech}^2 \left| \frac{h_0\gamma}{\tau_s - \tau_0} \right|, \tag{2.12a}$$

$$h_{\alpha\beta} = qh(\gamma) \quad (\alpha \neq \beta), \tag{2.12b}$$

where $h_{\alpha\alpha}$ term is known as the *self-hardening modulus*, h_0 is the initial hardening modulus, τ_s is the saturation strength, τ_0 is the initial yield stress (i.e. $\tau_0 = \tau^{(\alpha)}(0)$). The term $h_{\alpha\beta}$ (for $\alpha \neq \beta$) is known as the *latent hardening modulus*, and q is the latent hardening ratio, which is the ratio of the latent hardening rate to the self hardening rate of a slip system. The total accumulated strain on all slip systems, the total slip, is given by

$$\gamma = \sum_{\alpha=1}^{N} \int_0^t |\dot{\gamma}^{(\alpha)}| dt. \tag{2.13}$$

Bassani and Wu [10] proposed a hardening model, which describes the three hardening stages of an FCC single crystal as shown in Fig. 2.6. The self hardening (active hardening) and latent hardening moduli are expressed by the BW model as

$$h_{\alpha\alpha} = F(\gamma^{(\alpha)})\, G(\gamma^{(\beta)}; \beta = 1,\, N,\, \beta \neq \alpha), \tag{2.14a}$$

$$F(\gamma^{(\alpha)}) = \left[(h_0 - h_s)\mathrm{sech}^2 \left|\frac{(h_0 - h_s)\gamma^{(\alpha)}}{\tau_s - \tau_0}\right| + h_s\right], \tag{2.14b}$$

$$G(\gamma^{(\beta)}; \beta \neq \alpha) = 1 + \sum_{\beta \neq \alpha} f_{\alpha\beta} \tanh(\frac{\gamma^{(\beta)}}{\gamma_0}), \tag{2.14c}$$

$$h_{\alpha\beta} = q h_{\alpha\alpha} \quad (\alpha \neq \beta), \tag{2.14d}$$

where h_s is the hardening modulus during easy glide, $F(\gamma^{(\alpha)})$ is the instantaneous hardening modulus under single slip, and G is the function taking into account the effect of cross-hardening or interaction of slip systems. It can be inferred from the equation above that during the easy glide stage, $G = 1$ and the slip hardening behavior is represented by the function F. In the rapid hardening stage, due to the interaction between the primary and secondary slip, the forest hardening occurs and this hardening behavior is represented by the function G. γ_0 is the strain level after which the interaction between slip system α and slip system β reaches the peak strength. $f_{\alpha\beta}$ denotes the strength of the slip interaction between the slip systems. For FCC single crystals there are five distinct slip interactions. The first type of interaction is the interaction which does not result in any junction, in other words, the net Burgers vector from two slip system interaction is parallel to the original one. The second type of interaction is the so called Hirth lock, and the third type of interaction forms coplanar junctions, where the net Burgers vector is the sum of the two Burgers vector representing slip systems in interaction. The fourth and fifth type of interactions are formed by glissile and sessile (also referred to as Lomer-Cottrell lock) junctions, respectively (Bassani and Wu [10]).

The latent hardening ratio, q, can be measured through different methods. The first measurement method, which is a combination of two successive tensile tests, is summarized by Franciosi et al. [25], Wu et al. [70], and Asaro [8]. A uniaxial tensile load is applied to

Table 2.3: The hardening parameters used in finite element simulations in which material is assumed to show PAN hardening behavior. Latent hardening ratio (q) varies between 1 and 1.6. Saturation stress (τ_s) and initial hardening modulus (h_0) are given in terms of initial yield stress (τ_0), which is taken as 1 MPa for each simulation.

Simulation #	q	τ_s/τ_0	h_0/τ_0
1	1.0	5	10
2	1.0	5	1
3	1.0	2	10
4	1.0	2	1
5	1.2	5	10
6	1.4	5	10
7	1.6	5	10

Table 2.4: The hardening parameters used in finite element simulations in which material is assumed to show BW hardening behavior. Latent hardening ratio (q) is taken as 0 for each simulation. The hardening parameters used in simulations #5 and #6 are recommended by Kysar [44] and Bassani and Wu [10], respectively.

Simulation #	q	τ_s/τ_0	h_0/τ_0	h_s/τ_0	γ_0	f_0
1	0	2	2	1	0.001	7.2
2	0	5	11	1	0.001	7.2
3	0	2	11	1	0.001	7.2
4	0	5	2	1	0.001	7.2
5	0	1.24	0.7	38.7	0.001	7.2
6	0	1.3	1.5	90	0.001	8

an annealed high purity single crystal specimen, which is referred to as parent specimen. The specimen is deformed such that a small amount of plastic straining results. After imposing this plastic prestrain, smaller samples in different orientations are cut from the parent specimen and secondary tensile tests are applied to the new specimens. Whereas only one slip system, referred to as the primary slip system, is assumed to be activated during the primary test, new slip systems, which are previously latent, are activated during the secondary test. The initial yield stress associated with the primary test can then be obtained from the resolved shear stress-shear strain history. A method of back extrapolation is used to determine the initial yield stress in the secondary test. Therefore, the latent hardening ratio is the ratio of the initial yield stress of the secondary test to the initial yield stress of the primary test.

The second method to measure the latent hardening ratio is by means of X-ray diffraction and continual microscopical examination, which was proposed by Piercy et al. [60]. In-situ X-ray diffraction is used to determine the crystallographic orientation of the tensile axis at the onset of the activation of a conjugate slip system (or a secondary system). The change of the slope on the load-extension curve reveals the onset of a conjugate slip system. The resolved shear stress on the conjugate and primary system is calculated to determine the latent hardening ratio, which is the rate of critical resolved shear stress on the conjugate system to the critical resolved shear stress on the primary system.

The recommended values of the latent hardening ratio is in the range of $1 \leq q \leq 1.6$ for the PAN hardening model. The special case of Taylor, or isotropic, hardening is given by $q = 1.0$. In this case, due to the isotropic hardening, the hexagonal yield locus expands equally in all directions in stress space. If $q > 1.0$, then latent slip systems harden faster than the active slip systems (Kocks [39]). The facets of the yield locus correspond to a single slip and the vertices correspond to a double slip. $q = 0$ is referred to as diagonal hardening, and it is the recommended value for the BW model. Diagonal hardening effect can be observed either at vertex or on a facet of the yield locus. In the case of diagonal hardening observed

at a vertex, the three facets of the yield locus extend to form a triple point, which represents a triple slip. The diagonal hardening can be observed on a facet as the offset of two facets of the initial yield locus (Cuitino and Ortiz [15]).

2.5 Results and Discussion

This section consists of five subsections which mainly present the experimental and finite element simulation results. Crystal lattice rotations and the β-fields obtained after the deformation of a nickel single crystal by a wedge indenter are illustrated in Section 2.5.1. The data presented in this section is in the form of the as-measured experimental fields. The smoothing, or averaging was not applied to the data.

To be able to compare the experimental fields to finite element simulations we introduce filtering of the experimental data in Section 2.5.2. After applying the filtering process, a direct comparison between filtered and raw data is shown. We use a 2D Fourier transform to show that the small scale variations are no longer present in the filtered data.

In section 2.5.3, we compare the experimental $\beta-$fields to the $\beta-$fields obtained from the PAN simulations. Depending upon the simulation parameters, some of the $\beta-$field patterns coming from the PAN simulations do not fit the experimental $\beta-$fields. These figures are also presented in this section so as to show how the $\beta-$fields are sensitive to the hardening parameters that are used in finite element simulations. In the end of this section, a new approach, which illustrates the directions of the net Burgers density vector across the deformed surface through streamtraces, is presented. The directions are shown through the streamtraces for both finite element analysis and the experimental data in order to fully analyze the spatially resolved net Burgers density vector. Similarly, in section 2.5.4, the procedure is repeated for the BW finite element simulations.

In Section 3.2, a finer analysis is performed. The filtered experimental results are compared to simulation results along arcs with different radii, which are 1.5, 2.0, 2.5 and 3.0 times

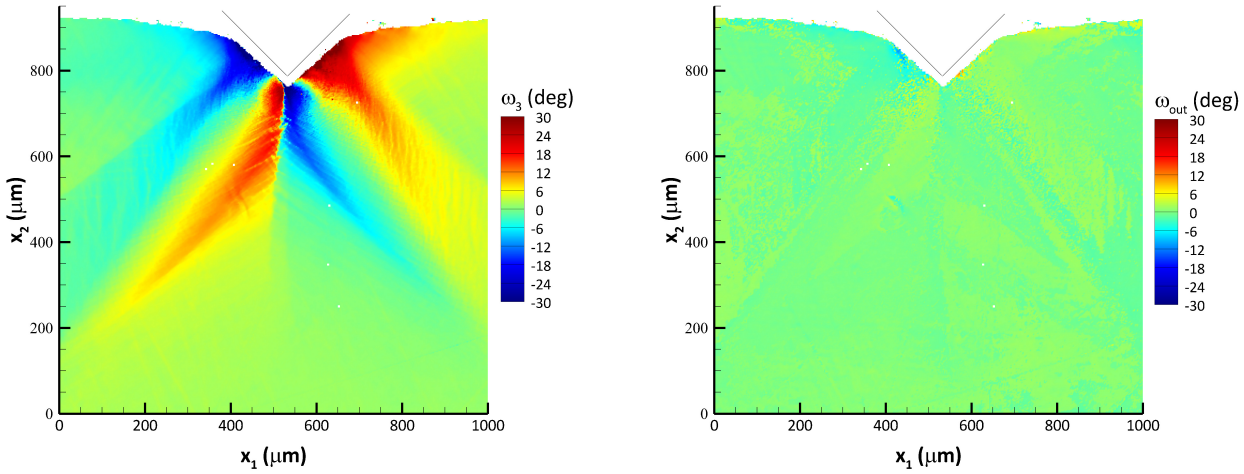

(a) (b)

Figure 2.7: Experimentally obtained crystal lattice rotations: (a) In-plane lattice rotation, ω_3, (rotation about x_3-axis); (b) Out-of-plane lattice rotation, ω_{out}

the maximum indentation depth to capture the small scale mechanical behavior.

2.5.1 Experimental Findings

A full description of the indentation process is explained in Section 2.3. After indentation process, the lattice rotation measurements were performed so as to capture the lattice rotation field. To do so, a mid-section of the single crystal, which is perpendicular to [110] direction, was exposed with the wire EDM. The newly exposed surface was then electrochemically polished in order to analyze the plane strain deformation state on this surface using High Resolution Electron Back-scattered Diffraction (HR-EBSD) with a $2.5\mu m$ spatial resolution. HR-EBSD equipment and the measurement method can be find in [46]. The rotations about x_1-, x_2-, and x_3-axes, which are represented by ω_1, ω_2, and ω_3, respectively, were obtained. The measured in-plane lattice rotation, ω_3, is illustrated in Fig. 2.7(a). The rotation field of ω_3 varies between $-30°$ and $+30°$ as shown in Fig. 2.7(a). It can also be observed that the rotation field is antisymmetric about the midline, which is the vertical axis passes through the indenter tip, and there is a jump discontinuity on the midline.

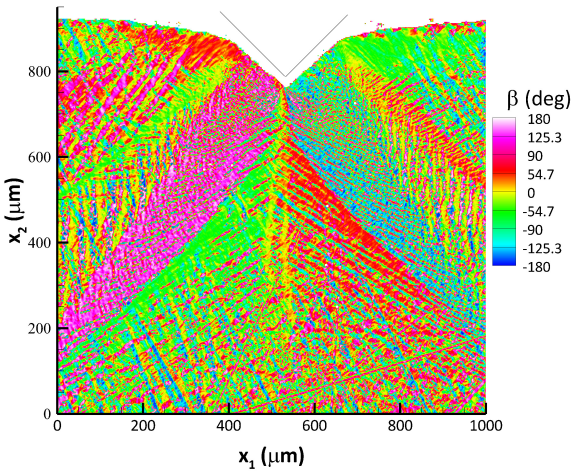

Figure 2.8: $\beta-$field after elastic-plastic deformation of the nickel single crystal through a wedge indentation process. Maximum depth of indentation, a, is 160 μm.

In-plane lattice rotation is the counterclockwise rotation about x_3-axis as described in Section 2.2 and the counterclockwise rotation was considered as a positive sense of rotation. ω_1 and ω_2 were measured as zero, which shows that $\omega_1 = \omega_2 = 0$ is a very good approximation for the plane strain deformation state. The out-of-plane lattice rotation, ω_{out} is defined as the angle between x_3' ([110] direction of the local crystallographic coordinate frame) and the normal of the newly exposed surface of the specimen. The measured out-of-plane lattice rotation is almost zero across the surface as shown in Fig. 2.7(b).

The β-field obtained from the measurement of the lattice rotation field is shown in Fig. 2.8. Experimentally obtained β-variables vary between $-180°$and $180°$. The coordinate frame of β-field is divided into six sectors as shown in Fig. 2.2 and Table 2.1 by taking into account of the characteristic orientation angles of effective slip systems, which are $-180°$, $-125.3°$, $-54.7°$, $0°$, $54.7°$, $125.3°$ and $180°$. One can easily analyze the β-field using Table. 2.1 to monitor the activity of the slip systems. Each color correspond to an activity region of a slip system. The regions, which are away from the indenter tip, do not experience extreme plastic deformation under the assumption of plane-strain deformation state. As shown in Fig. 2.8, the colors on the β-field look discrete so that it is hard to determine

the boundaries of the slip activity regions. In other words, the activity of the slip systems cannot be monitored using color legend provided with the β-field. In order to avoid this, a filtering process was applied to the experimental β-field to determine the boundaries of the slip activity regions, which are represented by different color schemes.

2.5.2 Filtering of Experimental Data

In order to eliminate the small variations on the experimental β-field and to detect the boundaries of the slip activity regions, a filtering process was applied. This enables us to make a finer analysis to compare the experimental β-field to the β-field obtained from Finite Element Simulations. Two-dimensional Fast Fourier Transform and various types of 2D filtering methods were performed using MATLAB commercial software to find the correct filtering method and the correct set of filtering parameters. Finally, 2D Low Pass Filtering and 2D Median Filtering were decided to use, and implemented to experimental β-field to remove the small variations and striations on the β-field. Various types of filtering parameters were adjusted so as to obtain continuous experimental β-field which can be used as a benchmark against finite element simulation results. The β-fields before and after the 2D filtering process are illustrated in Fig. 2.9. 2D Median Filtering method gave significant results comparing to the 2D Low Pass Filtering method. 2D Median Filtering creates matrices in two dimensions which are m by n neighborhood around the raw data points. The new output data points generate the median values in this m by n matrices. The field of new output data points form 2D filtered experimental β-field as shown in Fig. 2.9b. Two-dimensional Fast Fourier Transform of filtered and unfiltered data are also illustrated in Fig. 2.9c and Fig. 2.9d to see the effect of the spatial frequencies in vertical and horizontal directions. Fig. 2.9c shows that the spatial frequencies have significant effect in both vertical and horizontal directions. Whereas the low spatial frequency variations represent the boundary value problem, high spatial frequency variations represent the discreteness of the material coming from the spatially resolved defect densities. After removing high frequency spatial variations via filtering

process, the boundaries of the slip activity regions, which are represented by different colors, can be detected as shown in Fig. 2.9(b).

2.5.3 Comparison of the Experimental and PAN Simulation Results

Experimental $\beta-$field was compared to Pierce, Asaro and Needleman (PAN) Finite Element Simulation results in order to verify the β-quantity which monitors the activity of slip systems in a deformed zone. In this subsection, the parameters were selected by considering the hardening relations defined by PAN Hardening Model. The list of the parameters used in the simulations is given in Table 2.3. While the experimental β-field has good agreement with the simulations #1, #5, #6 and #7 as shown in Fig. 2.10, it has no agreement with the simulations #2, #3 and #4 as illustrated in Fig. 2.11.

Simulation #6 and simulation #7 have identical τ_s/τ_0 and h_0/τ_0 ratio, which are 5 and 10, respectively. The latent hardening ratios (q) are slightly different from each other as shown in Fig. 2.10. These latent hardening ratios are the recommended values for nickel single crystal as discussed in Section 2.4.1. Observing the color maps shown in Fig. 2.10(b) and Fig. 2.10(c), one can easily determine from left to right that the dominant color pattern is red, blue, yellow, red and green, successively. The contour maps ($\beta-$fields) can be interpreted using legend values in degrees. Dominant red color represents 54.7°, which is the characteristic angle of *Slip System 1*, in other words, *Slip System 1* is active in the red zone. Blue region is represented by the angle ranging between $-125.3°$ and $-180°$, which means that *Slip System -1* and *Slip System -2* are active in this region. Similarly, yellow region is represented by 0°, and this angle indicates that only the *Slip System 2* is active in the region. For green region, *Slip System -3* is dominantly active, and the field close to the (001) surface, which is away from the indentation tip, indicates an elastic deformation that will be analyzed later.

In order to obtain vector representation of the net Burgers Density Vector, a streamtrace analysis was performed using Tecplot 360 Commercial Software. Experimental $\alpha_{13}^{'}$ and $\alpha_{23}^{'}$, which are $x_1^{'}$and $x_2^{'}$ components of $\mathbf{B}$, were recalculated by applying a filtering process in

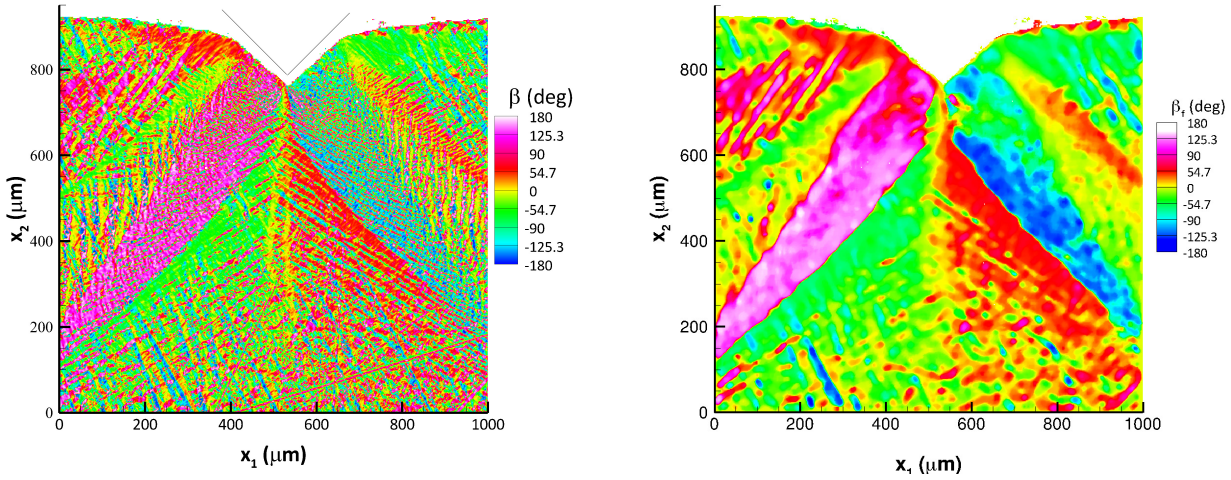

(a)

(b)

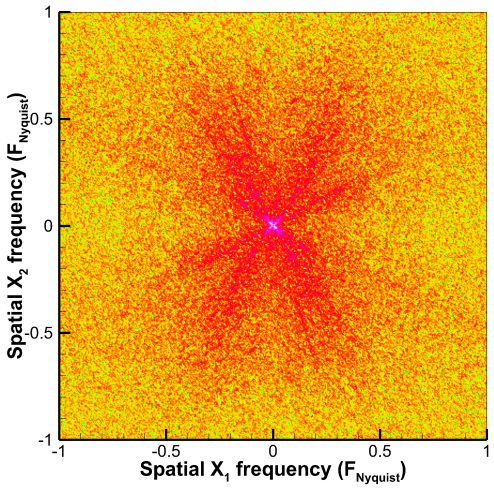

(c)

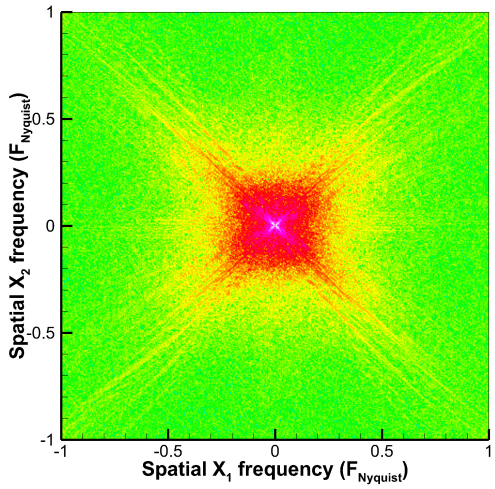

(d)

Figure 2.9: Two-dimensional (2D) filtering of experimental β-field: (a) Unfiltered experimental β-field; (b) 2D filtered experimental β-field; (c) 2D Fourier Transform of unfiltered β-field; (d) 2D Fourier Transform of filtered β-field.

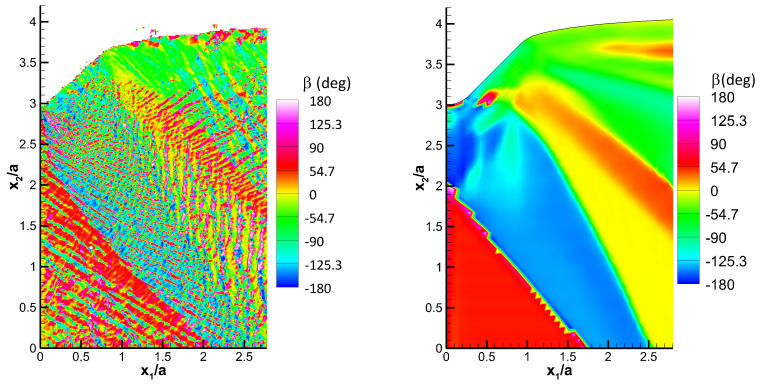

(a)

(b)

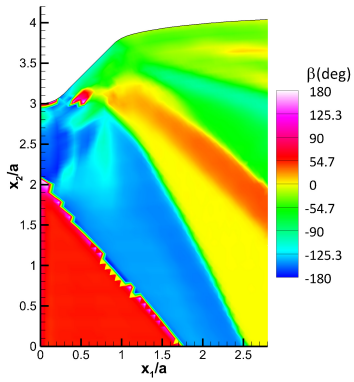

(c)

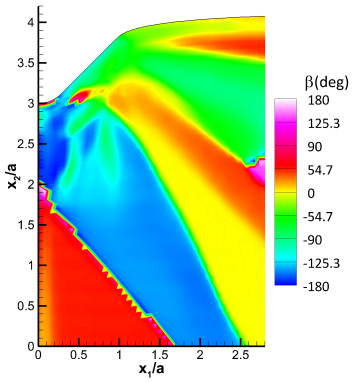

(d)

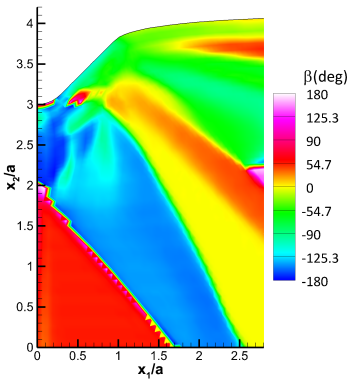

(e)

Figure 2.10: Comparison of the experimental β-field and the β-field associated with Finite Element Simulations employing PAN Hardening Model: (a) Right half portion of experimental β-field. The axes are normalized by a, maximum depth of indentation; (b) PAN Simulation#6, parameters: $q = 1.4$, $\tau_s/\tau_0 = 5$, $h_0/\tau_0 = 10$; (c) PAN Simulation#7, parameters: $q = 1.6$, $\tau_s/\tau_0 = 5$, $h_0/\tau_0 = 10$; (d) PAN Simulation#1, parameters: $q = 1.0$, $\tau_s/\tau_0 = 5$, $h_0/\tau_0 = 10$; (e) PAN Simulation#5, parameters: $q = 1.2$, $\tau_s/\tau_0 = 5$, $h_0/\tau_0 = 10$.

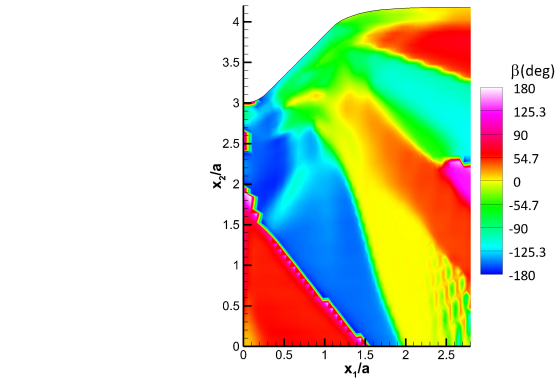

(a)

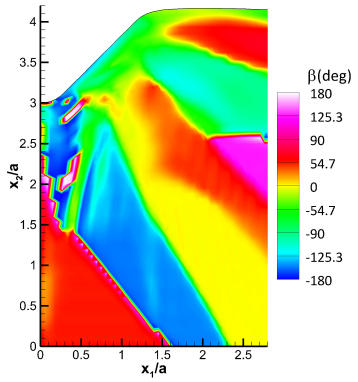

(b)

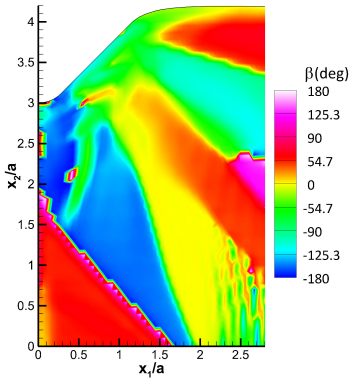

(c)

Figure 2.11: $\beta-$fields obtained from PAN Finite Element Simulations that do not fit the experimental β-field: (a) PAN Simulation#2, parameters: $q = 1.0$, $\tau_s/\tau_0 = 5$, $h_0/\tau_0 = 1$; (b) PAN Simulation#3, parameters: $q = 1.0$, $\tau_s/\tau_0 = 2$, $h_0/\tau_0 = 10$; (c) PAN Simulation#4, parameters: $q = 1.0$, $\tau_s/\tau_0 = 2$, $h_0/\tau_0 = 1$.

order to find the components of the net Burgers Density Vector. Combination of the filtered $\alpha_{13}^{'}$ and $\alpha_{23}^{'}$ components form the net Burgers Density Vector, which is shown in Fig. 2.12(a). The streamtraces represent the directions of the net Burgers Density Vector across the deformed surface. For the finite element simulations associated with PAN Hardening Model, the vectors $\alpha_{13}^{'}$ and $\alpha_{23}^{'}$ were directly calculated by employing the rotation field obtained through Finite Element Method. The directions of the net Burgers density vector across the deformed surface in both experimental and PAN simulations are illustrated in Fig. 2.12.

2.5.4 Comparison of the Experimental and BW Simulation Results

A similar comparative analysis has been performed for the Finite Element Simulations associated with Bassani and Wu (BW) Model. The simulation parameters associated with the BW Hardening Model are listed in Table 2.4. For this comparative analysis, whereas the experimental $\beta-$field has good agreement with simulation #5 and simulation #6 as illustrated in Fig. 2.13, it has no agreement with the simulations #1, #2, #3 and #4 as shown in Fig. 2.14. Diagonal hardening was considered for each simulation, and the results obtained from the simulations having $q = 0$, $\tau_s/\tau_0 = 1.24$, $h_0/\tau_0 = 0.7$, $h_s/\tau_0 = 38.7$, $\gamma_0 = 0.001$, $f_0 = 7.2$ and $q = 0$, $\tau_s/\tau_0 = 1.3$, $h_0/\tau_0 = 1.5$, $h_s/\tau_0 = 90$, $\gamma_0 = 0.001$, $f_0 = 7.2$ parameter sets are consistent with the experimental results.

A streamtace analysis was performed also for the BW simulation results by analogy with the objective outlined in Subsection 2.5.3. Similarly, the directions of the net Burgers density vector across the deformed surface in both experimental and BW simulations are illustrated in Fig. 2.15.

2.5.5 Analysis of the $\beta-$fields Along Arcs (β vs. θ)

The β-variable is extracted from the $\beta-$fields along the 90-degree arcs, C_1, C_2, C_3, and C_4 as shown in Fig. 3.1 in order to get detailed information about the state of the material. This analysis is called β vs. θ analysis, and represents the finer analysis of 2D plane strain

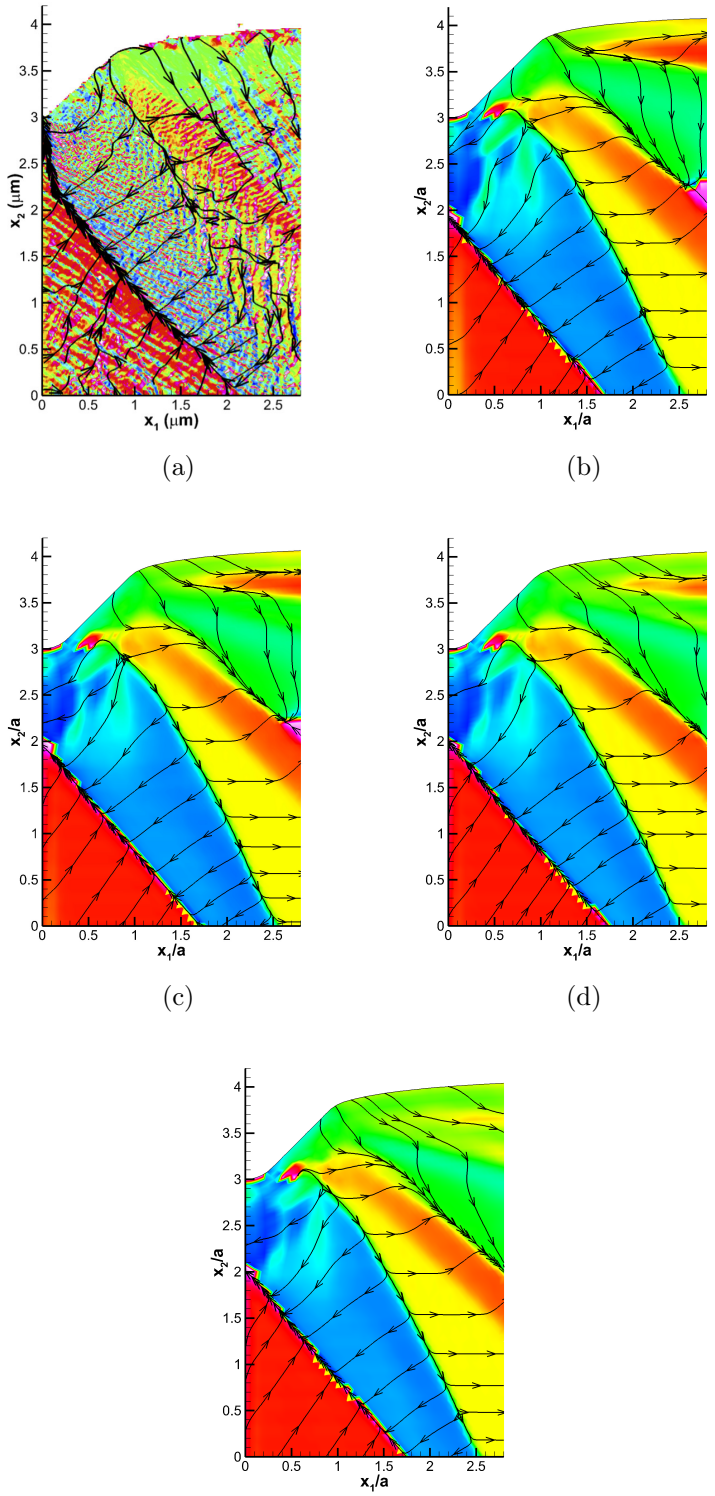

Figure 2.12: $\beta-$fields with the directions of the net Burgers density vector: (a) Net Burgers Density Vector on the experimental $\beta-$field; (b) PAN Simulation#1; (c) PAN Simulation#5; (d) PAN Simulation#6; (e) PAN Simulation#7.

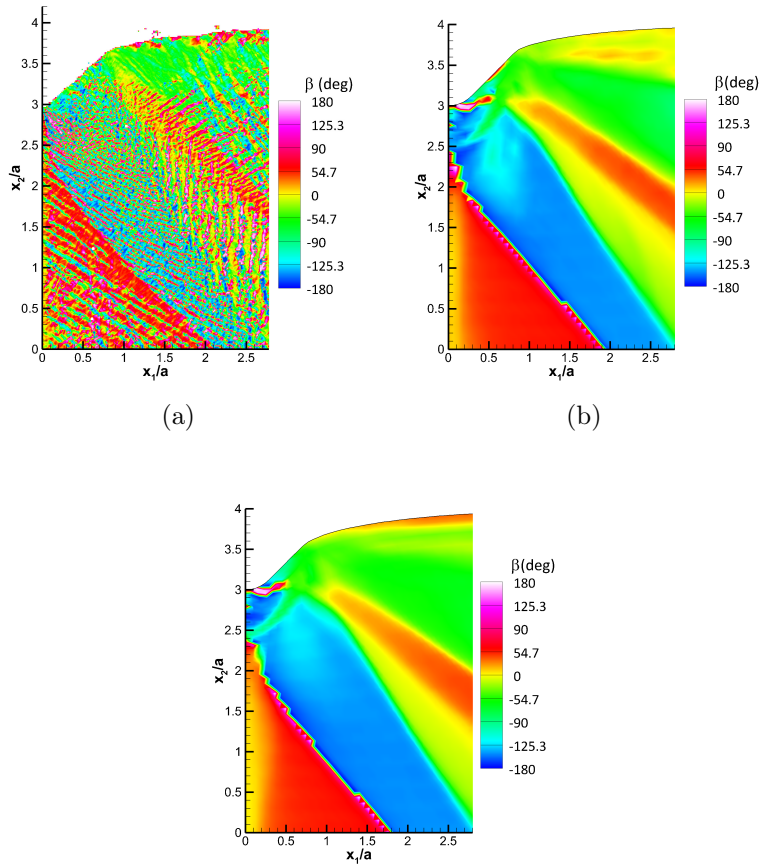

Figure 2.13: Comparison of the experimental $\beta-$field and the $\beta-$field associated with Finite Element Simulations employing BW Hardening Model: (a) Right half portion of experimental $\beta-$field. The axes are normalized by a, maximum depth of indentation; (b) BW Simulation#5, parameters: $q = 0$, $\tau_s/\tau_0 = 1.24$, $h_0/\tau_0 = 0.7$, $h_s/\tau_0 = 38.7$, $\gamma_0 = 0.001$, $f_0 = 7.2$; (c) BW Simulation#6, parameters: $q = 0$, $\tau_s/\tau_0 = 1.3$, $h_0/\tau_0 = 1.5$, $h_s/\tau_0 = 90$, $\gamma_0 = 0.001$, $f_0 = 7.2$.

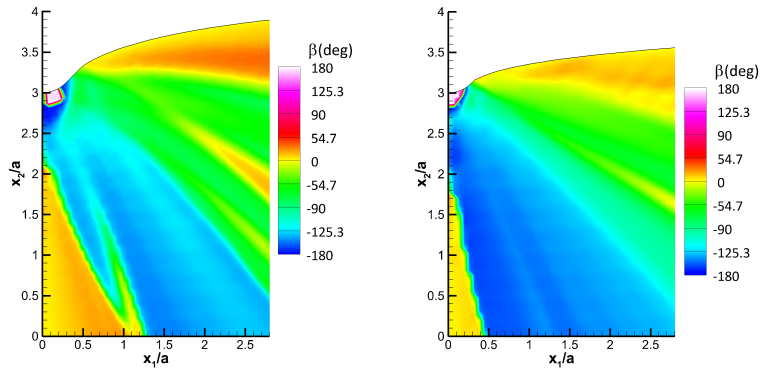

(a) (b)

(c) (d)

Figure 2.14: β-fields obtained from BW Finite Element Simulations that do not fit the experimental $\beta-$field: (a) BW Simulation#1, parameters: $q = 0$, $\tau_s/\tau_0 = 2$, $h_0/\tau_0 = 2$, $h_s/\tau_0 = 1$, $\gamma_0 = 0.001$, $f_0 = 7.2$; (b) BW Simulation#2, parameters: $q = 0$, $\tau_s/\tau_0 = 5$, $h_0/\tau_0 = 11$, $h_s/\tau_0 = 1$, $\gamma_0 = 0.001$, $f_0 = 7.2$; (c) BW Simulation#3, parameters: $q = 0$, $\tau_s/\tau_0 = 2$, $h_0/\tau_0 = 11$, $h_s/\tau_0 = 1$, $\gamma_0 = 0.001$, $f_0 = 7.2$; (d) BW Simulation#4, parameters: $q = 0$, $\tau_s/\tau_0 = 5$, $h_0/\tau_0 = 2$, $h_s/\tau_0 = 1$, $\gamma_0 = 0.001$, $f_0 = 7.2$.

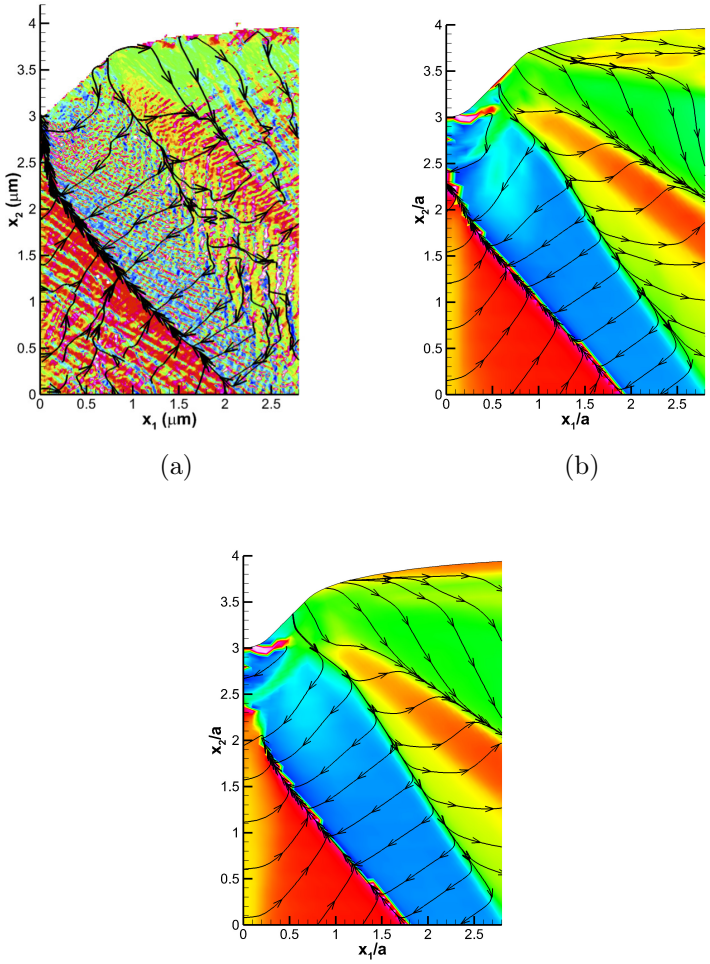

(a) (b)

(c)

Figure 2.15: β-fields with the directions of the net Burgers density vector: (a) Net Burgers Density Vector on experimental β-field; (b) Net Burgers Density Vector on the β-field obtained from BW Simulation#5; (c) Net Burgers Density Vector on the β-field obtained from BW Simulation#6.

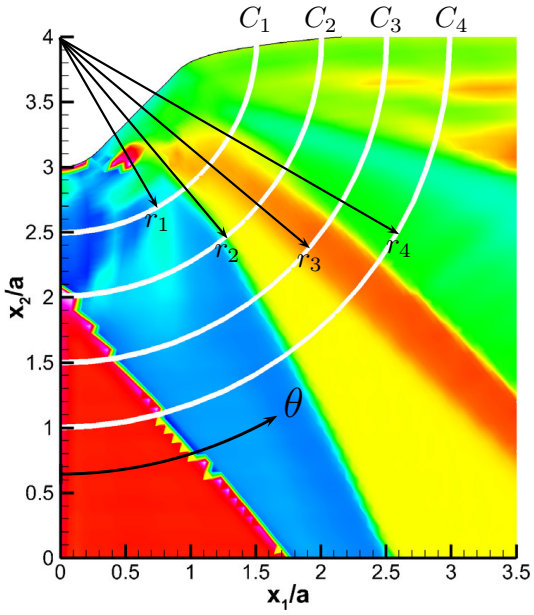

Figure 2.16: Construction of β vs. θ Analysis: $r_1 = 1.5a$, $r_2 = 2a$, $r_3 = 2.5a$, and $r_4 = 3a$.

deformation state. θ is the angle as shown in Fig. 3.1, and it is in the range of $[-90^\circ\ 0^\circ]$. The axes are normalized by a which is the maximum depth of indentation. As previously discussed, the maximum depth of indentation was measured as $160\mu m$. The r values in the Fig. 3.1, r_1, r_2, r_3, and r_4, are the radii of the 90-degree arcs, C_1, C_2, C_3, and C_4, respectively. A comparative analysis was performed in order to monitor the variation of the β along C_1, C_2, C_3, and C_4. Filtered experimental data was extracted and compared to PAN Simulation #1 in Fig. 2.17 as an example case. Whereas the as-filtered β-values along the 90-degree arcs, C_1, C_2, which are close to the tip of the wedge indenter as shown in Fig. 2.17(a) and Fig. 2.17(b) do not have a good agreement with the β-values obtained from FEM simulations, the β-values along the 90-degree arcs, C_3, C_4, have a good agreement with those obtained from FEM simulations as illustrated in Fig. 2.17(c) and Fig. 2.17(d). This is attributed to the relatively large rotations occurred in the area in between the indenter tip and C_2, whose radius is twice as much as maximum depth of indentation (i.e. $r = 2a$).

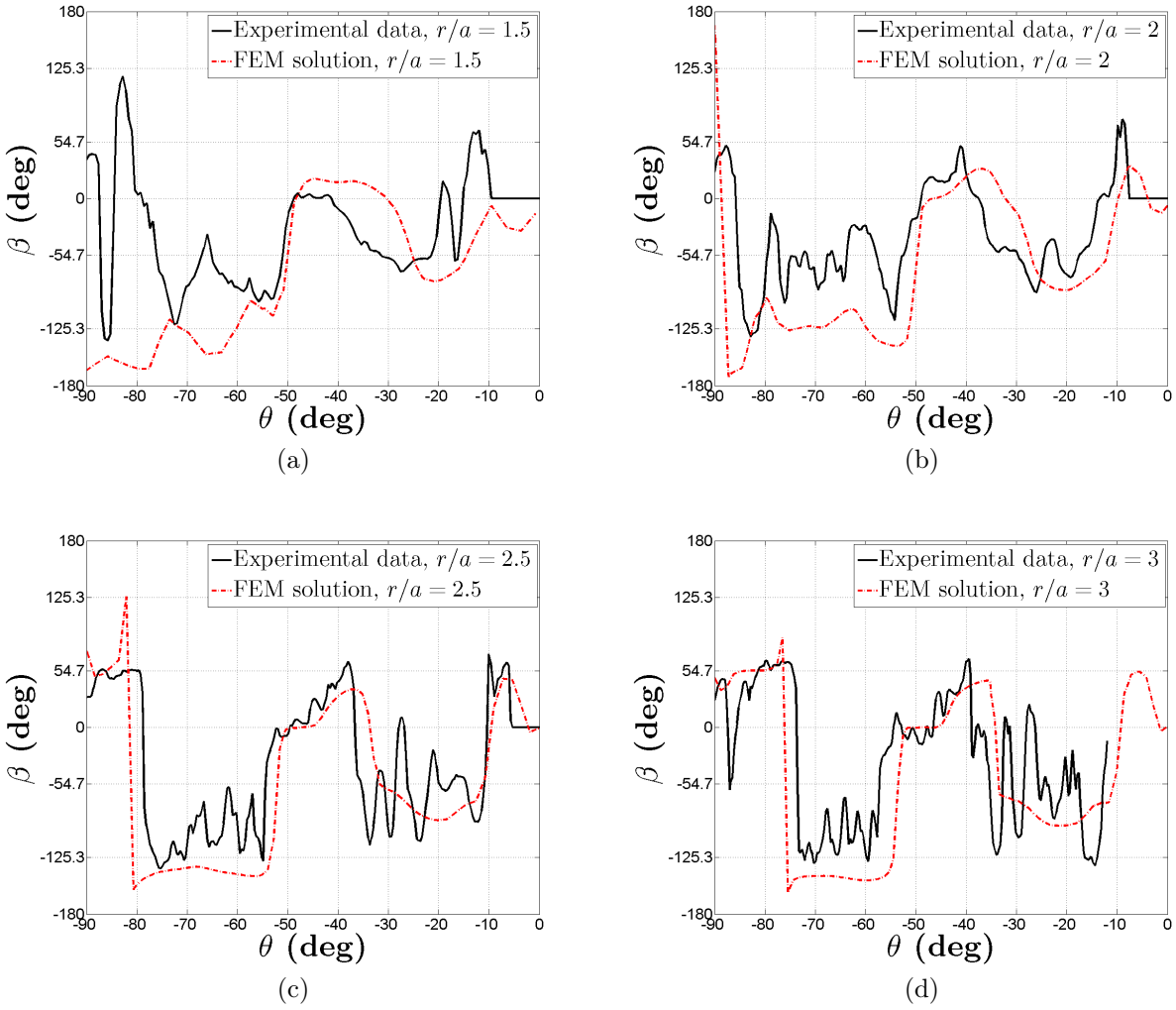

Figure 2.17: Variations of the β along C_1, C_2, C_3, and C_4: (a) β vs. θ for $r/a = 1.5$; (b) β vs. θ for $r/a = 2.0$; (c) β vs. θ curves for $r/a = 2.5$; (d) β vs. θ for $r/a = 3.0$.

2.6 Conclusions

A line load parallel to the [110] direction of a rectangular parallelepiped nickel single crystal was applied into (001) surface of the nickel single crystal resulting two dimensional plane-stress deformation state. Only three effective in-plane slip systems were activated on the deformed single crystal experiencing zero out-of-plane lattice rotation. In-plane lattice orientations were measured experimentally through recently developed HR-EBSD, and also calculated through single crystal plasticity simulations. Lattice curvatures were calculated by taking the numerical differentiation of the in-plane lattice orientations on the deformed non-uniform grid. Nye's dislocation density tensor was then formed by the non-zero components of the lattice curvature tensor. Transformation rules were applied to the Nye's dislocation density tensor, which serves as a link between elastic and plastic deformation states, in order to calculate the magnitude and the direction of the net Burgers density vector, which is a continuum manifestation of the Burgers circuit. A new variable, β, which is the representation of the orientation of the net Burgers density vector, was introduced to capture the activity of the effective slip systems on the deformed single crystal. β-fields were then obtained through both experimentally and finite element simulations employing two hardening rules. β-fields obtained from the experiment was compared to the single crystal plasticity simulations, and the activity of the slip systems were investigated for both experimental case and FEM solutions.

Existing experimental methods characterize the average response of an elastic-plastic system. The distribution of spatially resolved net Burgers density vector in a deformed single crystal was analyzed to measure the state of the material after extensive plastic deformation. Experimental β-fields were obtained using rotation fields with a spatial resolution of $2.5\mu m$. The β-fields were obtained as an experimental benchmark for validation of elastic-plastic constitutive relations. The directions of the net Burgers density vector through the streamtraces across the surface of a deformed single crystal was also presented in this study.

Chapter 3

Parametric Analysis

3.1 Introduction

The present work is a follow-up study of the paper which is presented in Chapter 2. In this chapter, a detailed analysis was carried out in order to monitor the β quantity along the arcs across the surface of the deformed nickel single crystal. Our objective is to analyze the influence of the hardening parameters on the β-variable and the β-field. The parameters in question are the latent hardening ratio, initial hardening modulus, and the saturation stress. The results pertaining to the each analysis are given in Section 3.3. To be able to get a finer information about the state of the deformed single crystal, variations of the individual plastic slips and slip rates along the arcs were investigated through finite element simulations. In the end of this work, the yield surface analysis was performed to capture elastic-plastic behavior of the deformed single crystal. The yield surfaces were generated after obtaining the stress space, which also gives information about the activity of the slip systems.

3.2 Analysis of the Variables Along Arcs

The analysis consists of four complementary parts in order to probe four different variables along arcs. The objective of the analysis is to present a finer analysis of two-dimensional

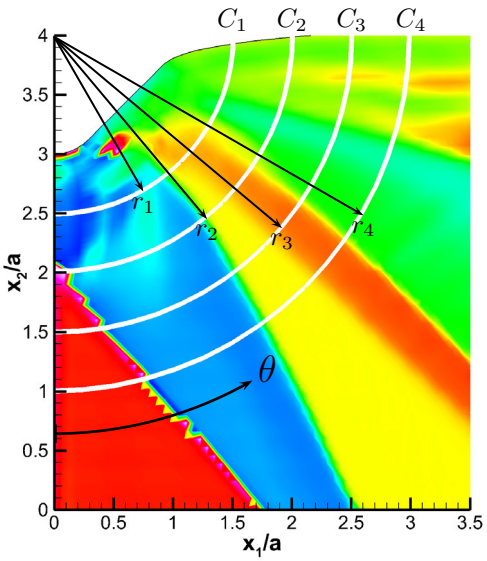

Figure 3.1: Construction of β vs. θ Analysis: $r_1 = 1.5a$, $r_2 = 2a$, $r_3 = 2.5a$, and $r_4 = 3a$.

plane strain deformation state of the indented single crystal.

First part of the analysis is the investigation of the β-variable as a function of θ (i.e. β vs. θ). The β-variable was extracted from the β-field along 90-degree arcs, C_1, C_2, C_3, and C_4 as shown in Fig. 3.1. The direction of θ is shown in Fig. 3.1, and taken in the range of $[-90^\circ\ 0^\circ]$. The axes in the figure are normalized by a, which is the maximum depth of indentation. As previously discussed in Chapter 2, the maximum depth of indentation was measured as $160\mu m$ in experiments. The r values, r_1, r_2, r_3, and r_4, are the radii of the 90-degree arcs, C_1, C_2, C_3, and C_4, respectively. The results given in Subsection 3.3.1, 3.3.2 and 3.3.3 were generated based on β vs. θ analysis to be able to analyze the influence of the hardening parameters on the β-variable and accordingly spatially resolved net Burgers density vector fields.

Second and third part of the analysis were performed to probe the plastic strains, γ and the dimensionless normalized slip rate, $\dot{\gamma}(a/\dot{a})$ along 90-degree arcs respectively. γ vs. θ and $\dot{\gamma}(a/\dot{a})$ vs. θ curves were obtained in order to determine the variations of the slips and slip rates associated with each slip system along 90-degree arcs, and the results are illustrated in

Subsection 3.3.4 and 3.3.5. Activity regions of the slip systems were marked on γ vs. θ and $\dot{\gamma}(a/\dot{a})$ vs. θ plots, which were obtained from the finite element simulations. As discussed in Chapter 2, the finite element simulations were performed by employing two hardening models (i.e. the Pierce-Asaro-Needleman (PAN) and Bassani-Wu (BW)), and the simulation results are presented in Subsection 3.3.4 and 3.3.5.

Fourth part of the analysis is performed to obtain the yield surfaces along 90-degree arcs to be able to understand the elastic-plastic behavior of the material under small scale yielding conditions, and the results are illustrated in Subsection 3.3.6.

3.3 Results and Discussion

The results pertaining to the analysis explained in detail in Section 3.2 are presented below. The first three subsections deal with the effects of the hardening parameters on the β-variable. The hardening parameters (i.e. latent hardening ratio, initial hardening modulus, and saturation stress) were chosen by considering the hardening relations that were set in Chapter 2. Seven sets of parameters associated with the PAN Hardening Model were used for seven finite element simulations, and the other six sets of parameters were used in the finite element simulations that employ the BW Hardening Model. Therefore, totally thirteen simulations were performed to capture the effect of the hardening parameters on the β-variable, in other words, the effect of the hardening parameters on the activity regions of the effective slip systems. The next two subsections deal with the variations of the plastic strains and the slip rates along the arcs. The results were analyzed to determine the boundaries of the activity regions of the slip systems by marking the boundaries on the plots. In the end of this section, the results pertaining to the stress space along the arcs are also presented to analyze the elastic-plastic behavior of the deformed single crystal.

3.3.1 Effect of Latent Hardening Ratio (q) on the $\beta-$variable

The results associated with four different finite element simulations were compared in order to figure out the influence of the latent hardening ratio, q, on the β-variable and β-field. The finite element simulations were performed considering four sets of parameters correspond to the PAN Hardening Model. The PAN Simulations #1, #5, #6, and #7 were compared due to only the latent hardening ratios of the simulations are different. Whereas the saturation stress ratios (τ_s/τ_0) and initial hardening modulus ratios (h_0/τ_0) are the same, the latent hardening ratios selected for the simulations are 1.0, 1.2, 1.4 and 1.6 respectively. The results of the simulations were probed along 90-degree arcs (i.e. C_1, C_2, C_3, C_4) and the plots were generated as shown in Fig. 3.2 to illustrate the variation of β-variable as a function of θ. The values on the axis of β-variable (i.e. $-125.3°$, $-54.7°$, $0°$, $54.7°$, $125.3°$, $180°$) are the characteristic angles of the slip systems. The active slip systems can be distinguished by monitoring these characteristic angles. One can easily observe from the Fig. 3.2 that there is no significant change on the plots corresponding to different 90-degree arcs. In other words, there is no significant effect of latent hardening ratio, q, on the $\beta-$variable and accordingly the activity region of the effective slip systems. However, there can be observed some changes in β as the θ angles are less than $-20°$. This small change after $-20°$ is away from the indenter tip that we do not expect extreme plastic deformation. This will be shown in the later section by probing the stress space along the arcs in order to analyze elastic-plastic behavior of the material.

3.3.2 Effect of Initial Hardening Modulus (h_0) on the $\beta-$variable

Two pairs of finite element simulations were performed, and the results of the simulations were compared to be able to understand how the β-variable and the β-field change while the initial hardening modulus alters. While the saturation stress ratios (τ_s/τ_0) and the latent hardening ratios (q) corresponding to the PAN Simulation #1 and #2 were taken as 5 and 1.0, respectively, the initial hardening modulus ratios were taken as 10 and 1. As

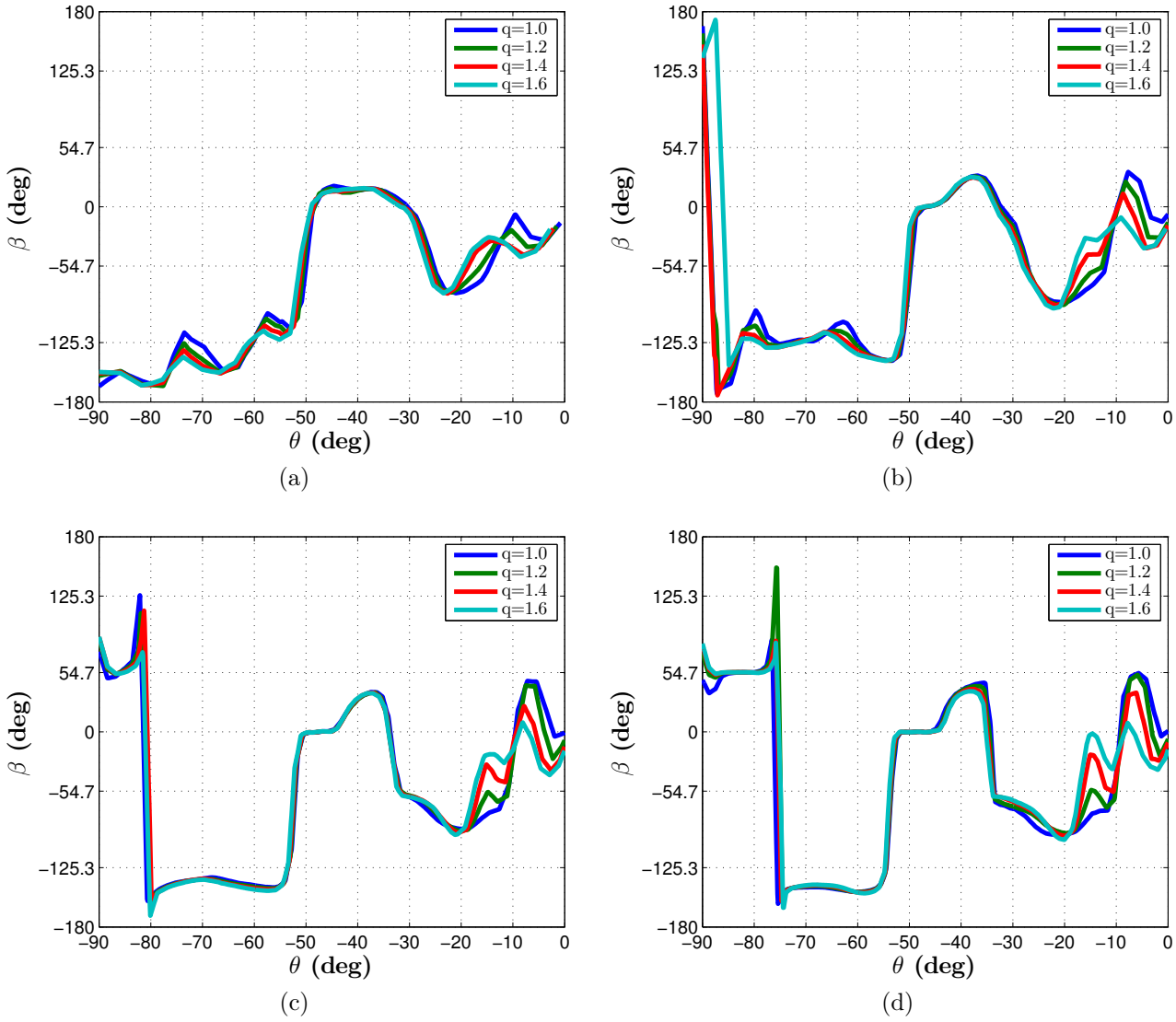

Figure 3.2: Effect of latent hardening ratio (q) on β-variable (Four finite element simulations were performed by employing PAN hardening model, where $\tau_s/\tau_0 = 5$, $h_0/\tau_0 = 10$): (a) β as a function of θ along C_1; (b) β as a function of θ along C_2; (c) β as a function of θ along C_3; (d) β as a function of θ along C_4.

shown in Fig. 3.3, a change in the initial hardening modulus leads to a significant change on the β-variable and β-field, and it can be seen that the boundaries of the slip activity regions are moving to the right or left as h_0 is varying. The amount of boundary shifts observed for C_1, C_2, C_3 and C_4 is nearly same. This shows that the boundary shifts in the direction of θ angle. The boundary shift is observed nearly 5°, which is almost 30% of the initial slip activity region (i.e. the area of the slip activity region in terms of the θ angle). The boundary shifts, which are greater than 10% of the initial slip activity region, are considered as significant change in the parametric analysis. The influence of the initial hardening modulus on the β-field in the large scale can be discerned by assessing the β-fields associated with the the PAN Simulations #1 and #2.

Similarly, the effect of the initial hardening modulus was investigated by comparing the PAN Simulations #3 and #4, in which the saturation stress ratios (τ_s/τ_0) and the latent hardening ratios (q) are 2 and 1.0, respectively. The initial hardening modulus ratios correspond to the PAN simulations #3 and #4 are 10 and 1, and are as same as in the PAN Simulations #1 and #2. As illustrated in Fig. 3.4, whereas the change in the $\beta-$variable is small, the boundaries of the slip activity regions remained nearly same.

3.3.3 Effect of Saturation Stress (τ_s) on the β-variable

The variations of the β-variable were investigated for different values of the saturation stress. The variations, which are illustrated in Fig. 3.5, show the comparison of the results obtained by the PAN Simulations #1 and #3, in which the saturation stresses correspond to the simulations #1 and #3 are 5 MPa and 2 MPa, respectively. It can be seen that the saturation stress is a significant parameter that has an influence on the β-variable as well as the β-field. The boundaries of the slip activity regions alter significantly as the saturation stress changes as a factor of 2.5. Therefore, the saturation stress and the initial hardening modulus have relatively high influence on the β-variable compared to the latent hardening ratio.

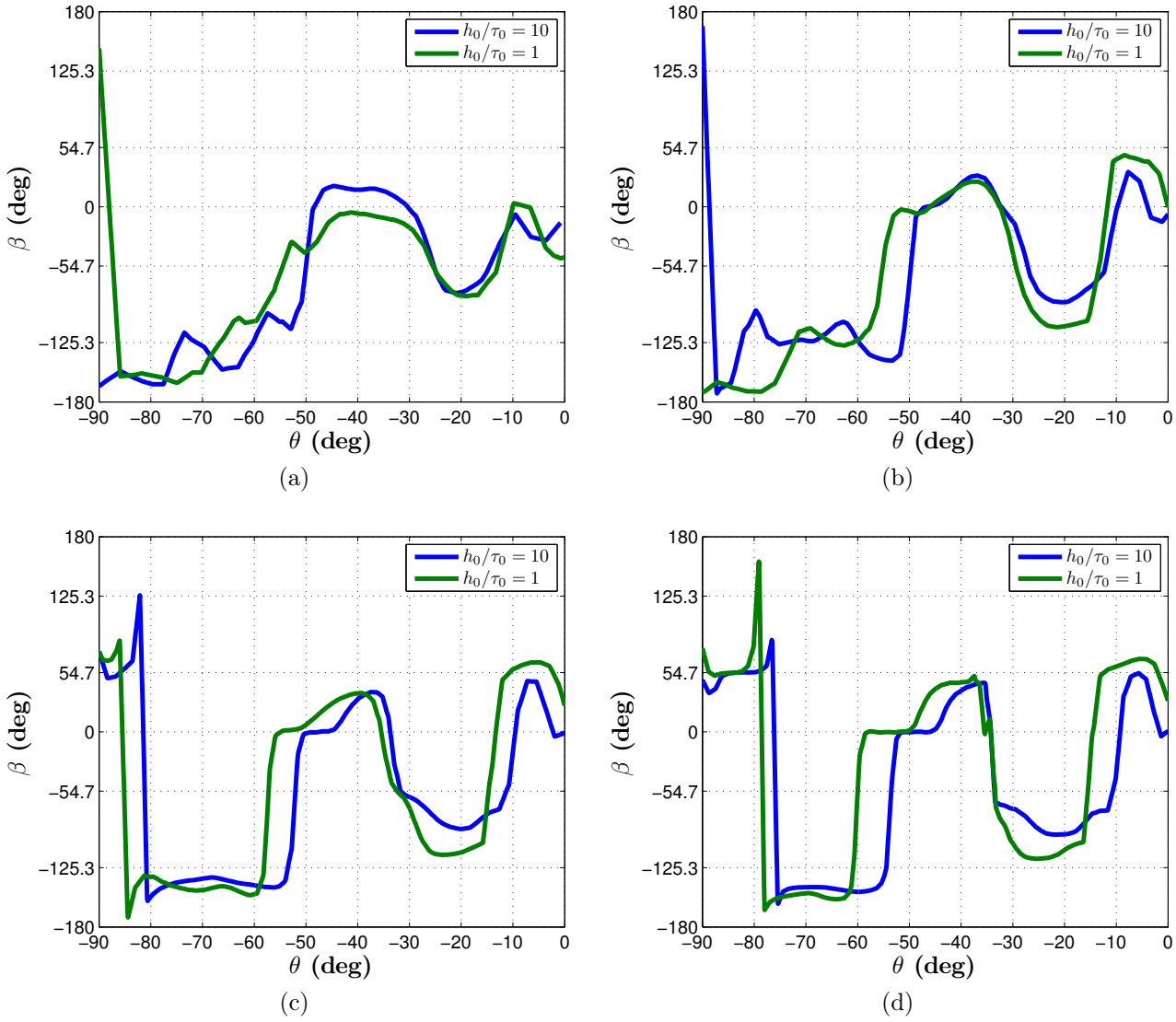

Figure 3.3: Effect of initial hardening modulus (h_0) on the β-variable (Two finite element simulations were compared by employing PAN hardening model, where $\tau_s/\tau_0 = 5$, $q = 1.0$): (a) β as a function of θ along C_1; (b) β as a function of θ along C_2; (c) β as a function of θ along C_3; (d) β as a function of θ along C_4.

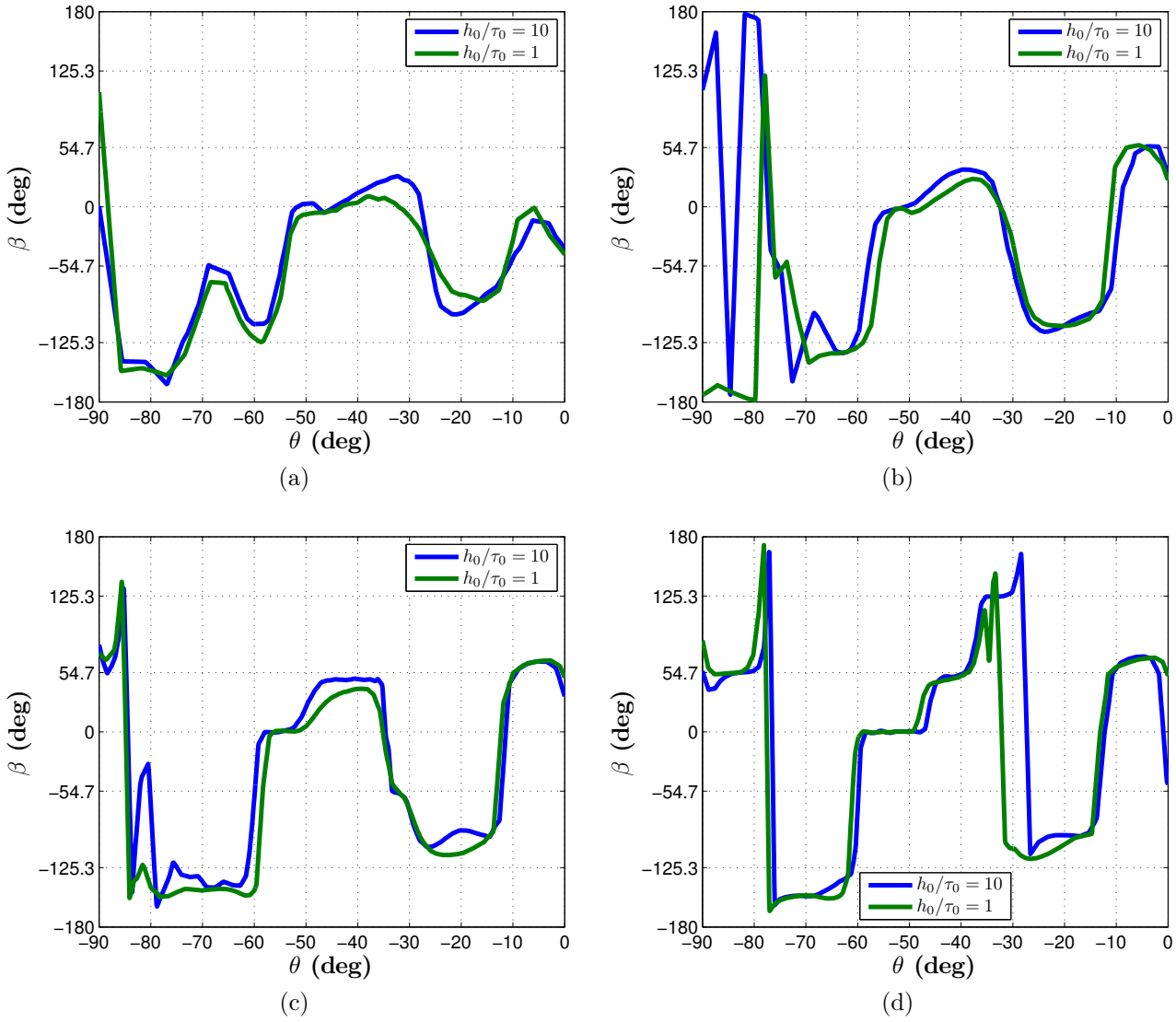

Figure 3.4: Effect of initial hardening modulus, h_0 on β-variable (Two finite element simulations were compared by employing PAN hardening model, where $\tau_s/\tau_0 = 2$, $q = 1.0$): (a) β as a function of θ along C_1; (b) β as a function of θ along C_2; (c) β as a function of θ along C_3; (d) β as a function of θ along C_4.

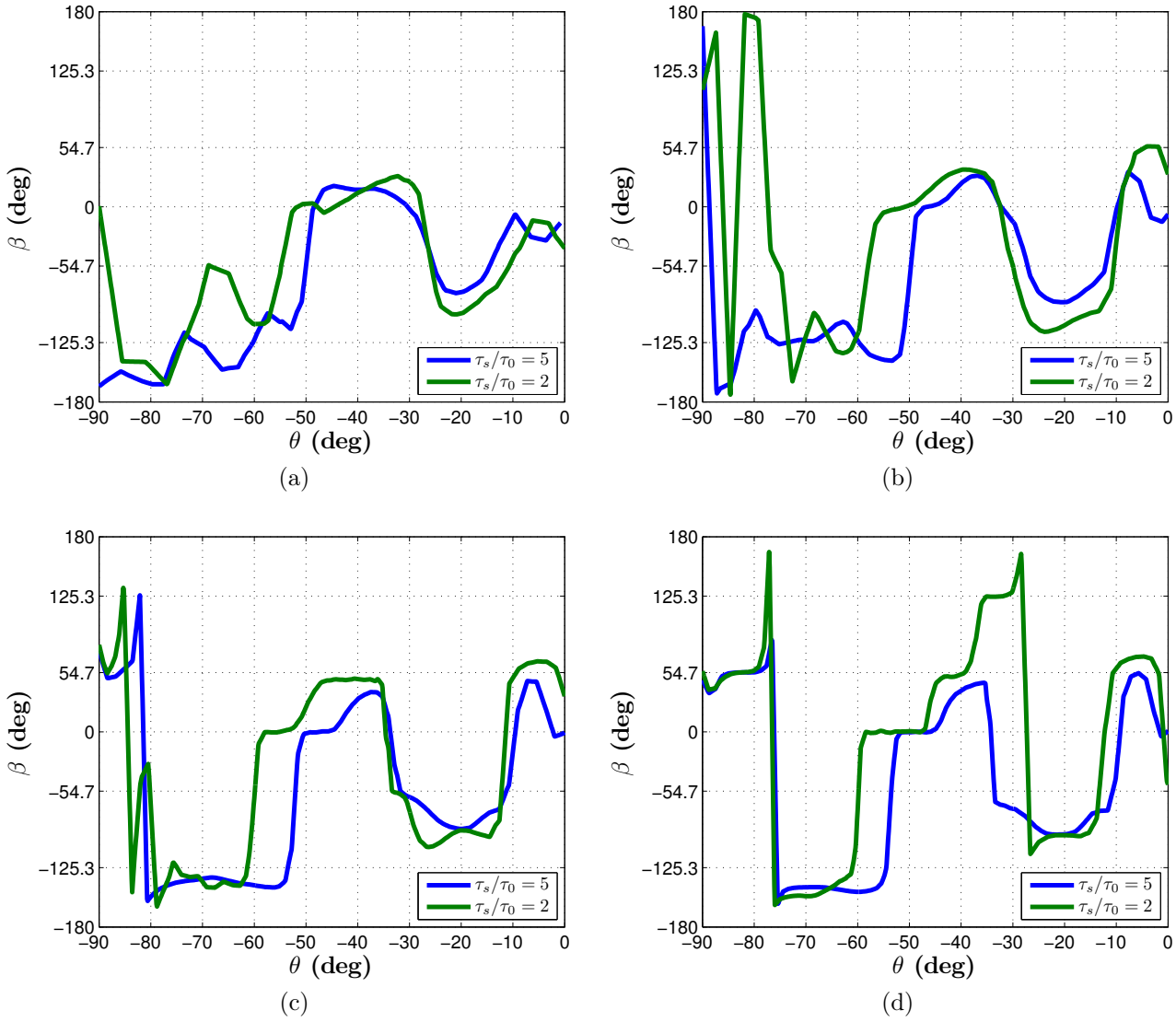

Figure 3.5: Effect of saturation stress (τ_s) on β-variable (Two finite element simulations were compared by employing PAN hardening model, where $h_0/\tau_0 = 10$, $q = 1.0$): (a) β as a function of θ along C_1; (b) β as a function of θ along C_2; (c) β as a function of θ along C_3; (d) β as a function of θ along C_4.

3.3.4 Variations of Plastic Strains and Slip Rates Associated with the PAN Hardening Model

The β-fields obtained from the finite element simulations (i.e. the PAN simulations #6 and #7) have a good agreement with those obtained from the experiment that can be found in Chapter 2. To get the finer information about the β-fields, the plastic strains and normalized slip rates corresponding to the Simulations #6 and #7 are investigated along the 90-degree arcs. The normalized slip rates can be used to characterize the slip activity regions.

Plastic Strains and Slip Rates Associated with the PAN Simulation #6

The slips associated with each effective slip system were calculated by employing the PAN Hardening Model, where $q = 1.4$, $\tau_s = 5$ MPa and $h_0/\tau_0 = 10$. The plastic strains are getting smaller as moving from C_1 to C_4, and the plastic slips take the minimum values on C_4 as shown in Fig. 3.6. Total plastic strains along the arcs were calculated by adding up the all individual plastic slips, $\gamma^{(1)}$, $\gamma^{(2)}$, and $\gamma^{(3)}$ (i.e. $\gamma_{total} = \gamma^{(1)} + \gamma^{(2)} + \gamma^{(3)}$).

The normalized slip rates were calculated to determine the slip activity regions as illustrated in Fig. 3.7. After investigating the normalized slip rates along the arcs, the boundaries of the slip activity regions were detected. The activity regions were separated from each other by using the dashed lines. The regions were then numbered to show which slip system is dominantly active in that particular region. For instance, Fig. 3.7(d) that shows the variations of the normalized slip rates along C_4, is divided into six regions, where the boundaries of the regions are expressed by the range of the θ angle. The ranges of the θ for the boundaries of the regions I, II, III, IV, and V are $[-90°, -78°]$, $[-78°, -52°]$, $[-52°, -38°]$, $[-38°, -35°]$, and $[-35°, -10°]$, respectively. The material deforms elastically in the region which is limited by the angle less than $-10°$. Therefore, only the effective *Slip System 1* is active in I, the effective *Slip System 1* and *2* are active together in II, only the effective *Slip System 2* is active in III, the effective *Slip System 2* and *3* are active together in IV, and only the effective *Slip System 3* is active in V.

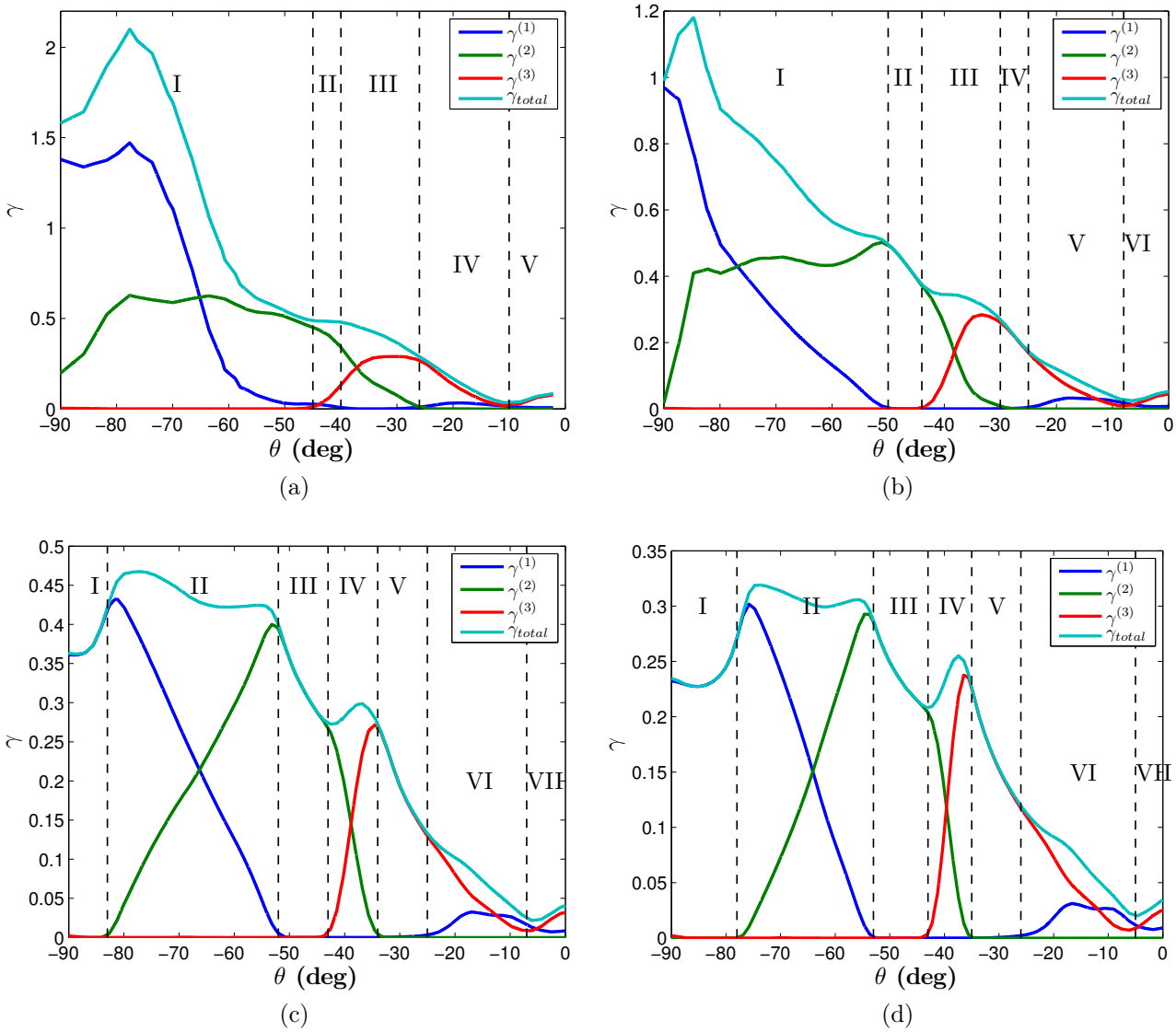

Figure 3.6: Total plastic strain (γ_{total}) and the plastic strain on each effective slip system ($\gamma^{(1)}$, $\gamma^{(2)}$, and $\gamma^{(3)}$) obtained by PAN hardening simulations, where $q = 1.4$, $\tau_s/\tau_0 = 5$, $h_0/\tau_0 = 10$: (a) Plastic strain, γ along C_1; (b) Plastic strain, γ along C_2; (c) Plastic strain, γ along C_3; (d) Plastic strain, γ along C_4.

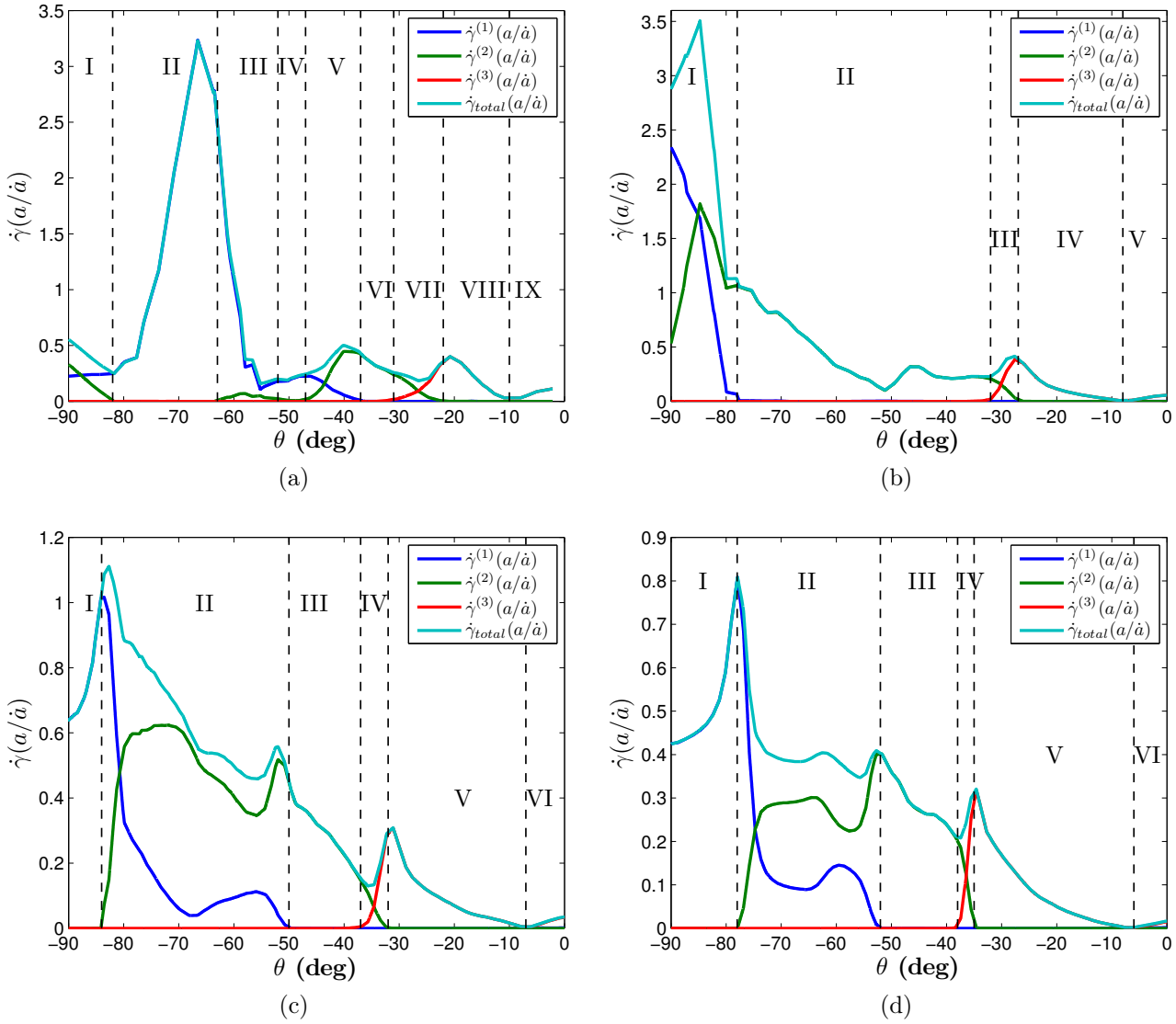

Figure 3.7: Total normalized slip rate ($\dot{\gamma}_{total}(a/\dot{a})$) and the normalized slip rate of each effective slip system ($\dot{\gamma}^{(1)}(a/\dot{a})$, $\dot{\gamma}^{(2)}(a/\dot{a})$, and $\dot{\gamma}^{(3)}(a/\dot{a})$) obtained from PAN hardening model, where $q = 1.4$, $\tau_s/\tau_0 = 5$, $h_0/\tau_0 = 10$: (a) Normalized slip rate, $\dot{\gamma}(a/\dot{a})$ along C_1; (b) Normalized slip rate, $\dot{\gamma}(a/\dot{a})$ along C_2; (c) Normalized slip rate, $\dot{\gamma}(a/\dot{a})$ along C_3; (d) Normalized slip rate, $\dot{\gamma}(a/\dot{a})$ along C_4.

Plastic Strain and Slip Rates Associated with the PAN Simulation #7

The plastic strains associated with each effective slip system (i.e. $\gamma^{(1)}, \gamma^{(2)}, \gamma^{(3)}$) and total slips (i.e. γ_{total}) along the arcs are illustrated in Fig. 3.8. The results were generated by employing the PAN Hardening Model, where $q = 1.6$, $\tau_s = 5$ MPa and $h_0/\tau_0 = 10$. The amount of total slips in the vicinity of the indented region are larger than the slips that are away from the indented region. In other words, the total slips associated with C_1 and C_2 as illustrated in Fig. 3.8(a) and Fig. 3.8(b) are greater than those associated with C_3 and C_4 as illustrated in Fig. 3.8(c) and Fig. 3.8(d). Whereas the maximum total slip on C_3 is approximately 45%, and the minimum total slip is occurred nearly at -7° as shown in Fig. 3.8(c); the maximum total slip on C_4 is approximately 32%, and the minimum total slip is observed at -5° as shown in Fig. 3.8(d). However, it can be seen that the slip patterns shifted to the right in Fig. 3.8(d), the slip patterns associated with C_3 and C_4 as illustrated in Fig. 3.8(c) and Fig. 3.8(d) are very similar.

The normalized slip rates were also obtained as displayed in Fig. 3.9 to discern the slip activity regions. It can be seen that only the single slips and the double slips were occurred on the deformed single crystal as shown in Fig. 3.9(c) and Fig. 3.9(d). Similar to the case in the PAN Simulation #6, only the *Slip System 1* is active in I, the *Slip System 1* and *2* are active together in II, only the *Slip System 2* is active in III, the *Slip System 2* and *3* are active together in IV, and finally only the *Slip System 3* is active in V. The boundaries of the slip activity regions can be given by the range of θ, in this case, the θ ranges associated with the regions in Fig. 3.9(d) are $[-90^\circ, -78^\circ]$, $[-78^\circ, -52^\circ]$, $[-52^\circ, -38^\circ]$, $[-38^\circ, -35^\circ]$, and $[-35^\circ, -10^\circ]$, respectively. It can be observed that the outcomes of the PAN Simulation #6 and the PAN Simulation #7 are very similar in terms of the plastic strains and the normalized slip rates in the finer scale. Hence, the similarities of the simulations in the large scale are also seen in the finer scale analysis. The only difference between the parameters of two finite element simulations is latent hardening ratio. The slip and the slip rate variations present that the latent hardening ratio has very small influence on the slip activity regions

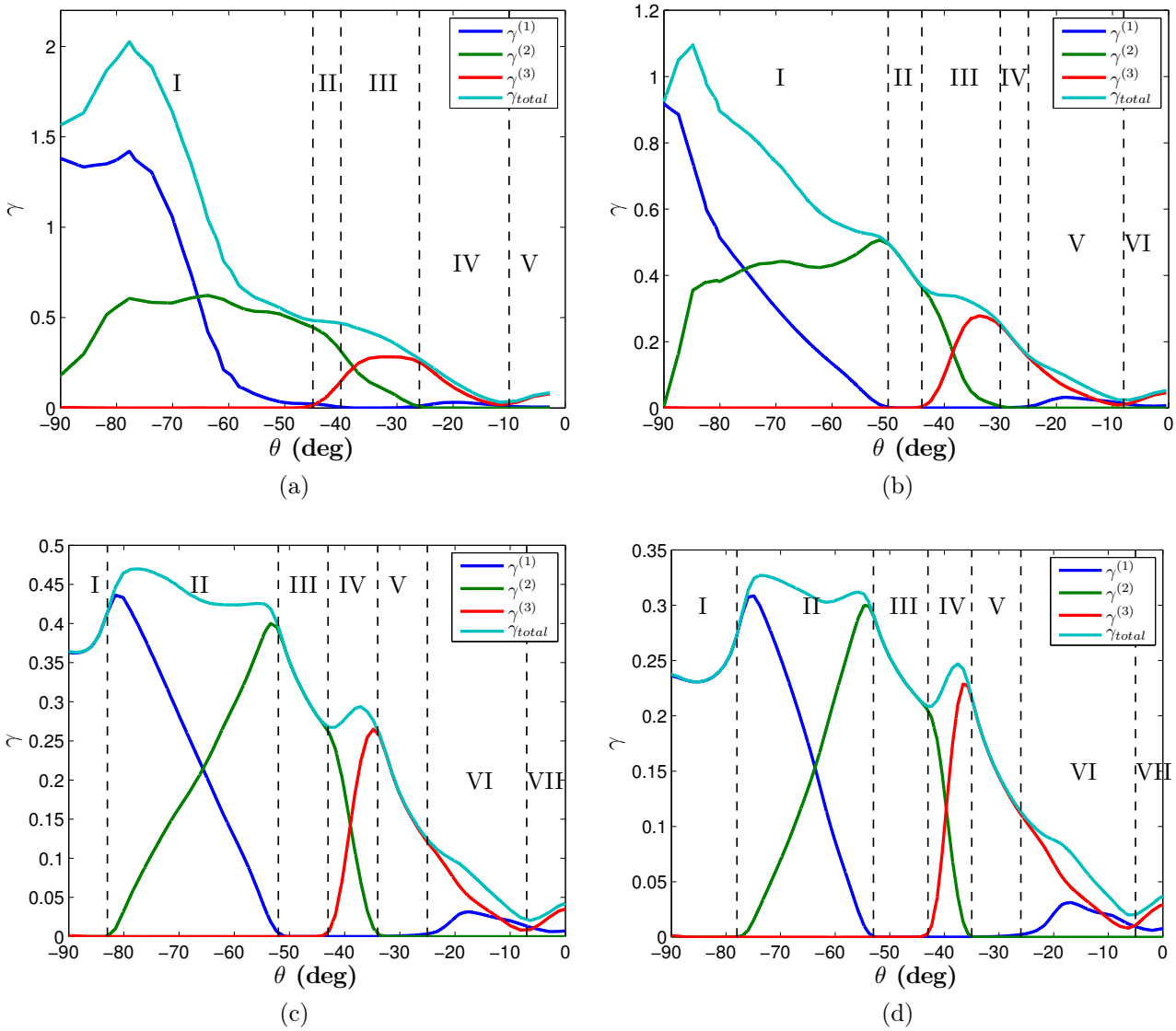

Figure 3.8: Total slip (γ_{total}) and the slip on each effective slip system ($\gamma^{(1)}$, $\gamma^{(2)}$, and $\gamma^{(3)}$) obtained from PAN hardening model, where $q = 1.6$, $\tau_s/\tau_0 = 5$, $h_0/\tau_0 = 10$: (a) Plastic strain, γ along C_1; (b) Plastic strain, γ along C_2; (c) Plastic strain, γ along C_3; (d) Plastic strain, γ along C_4.

and their boundaries.

3.3.5 Variations of Plastic Strains and Slip Rates Associated with the BW Hardening Model

Variations of the plastic strains and the normalized slip rates were also monitored by employing the BW Hardening Model. The analysis that is similar to the one in Section 3.3.4 was performed for the BW Simulations #5 and #6, where the $\beta-$fields have a good agreement with the experimental $\beta-$fields in large scale as shown in Chapter 2. The plastic strain and the normalized slip rate patterns were obtained, and the activity regions of slips were investigated to compare the results obtained from the PAN Simulations #6 and #7 to those obtained from the BW Simulations #5 and #6. Comparing to the PAN Hardening Model, there are two additional parameters (i.e. h_s, hardening modulus during easy glide; and f_0, strength of the slip interactions) in the BW Hardening Models to simulate the three stages of the face centered cubic single crystals.

Plastic strains and Slip Rates Associated with the BW Simulation #5

The plastic strains, $\gamma^{(1)}$, $\gamma^{(2)}$, $\gamma^{(3)}$, γ_{total}, were obtained by employing the BW Simulation #5 in which $q = 0$, $\tau_s/\tau_0 = 1.24$, $h_0/\tau_0 = 0.7$, $h_s/\tau_0 = 38.7$, $\gamma_0 = 0.001$, $f_0 = 7.2$. The plastic strains were calculated using the diagonal hardening rule, and the total slips along the arcs were computed by adding up the individual plastic strains. The slip patterns along the arcs, C_1, C_2, C_3, C_4, which are very similar to those obtained from the PAN Simulations #6 and #7, are illustrated in Fig. 3.10. The significant difference between the BW and the PAN results is that the Slip System 3 is also active in the range of $[-90^0 - 80^0]$. In addition, the variations of the total slips as shown in Fig. 3.10 are almost 2% less than those obtained from the PAN Simulation #6.

The normalized slip rates are shown in Fig. 3.11 to investigate the slip activity regions for the BW Simulation #5. Similar to the PAN Simulation #6 and #7, double slips and

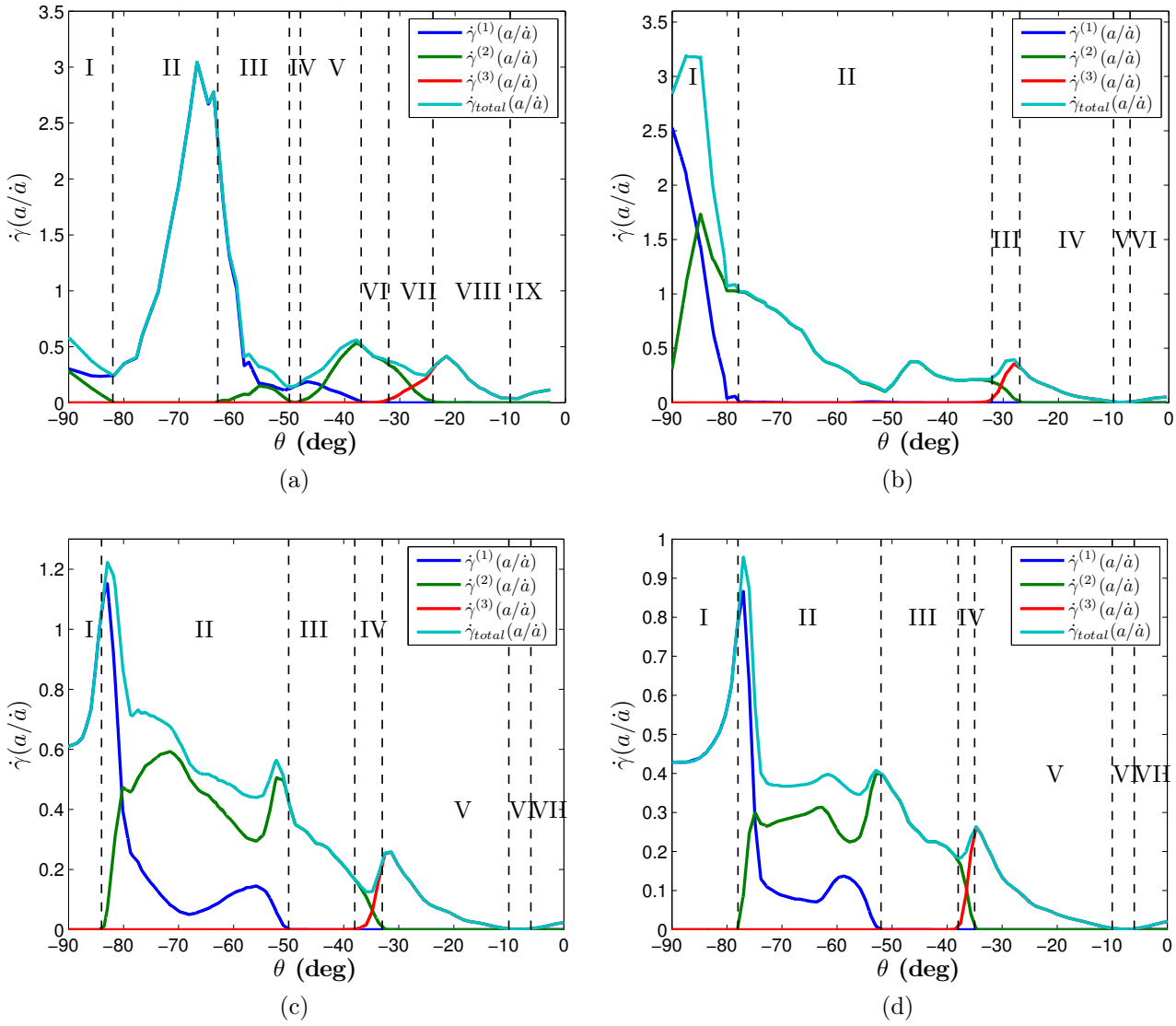

Figure 3.9: Total normalized slip rate ($\dot{\gamma}_{total}(a/\dot{a})$) and the normalized slip rate of each effective slip system ($\dot{\gamma}^{(1)}(a/\dot{a})$, $\dot{\gamma}^{(2)}(a/\dot{a})$, and $\dot{\gamma}^{(3)}(a/\dot{a})$) obtained from PAN hardening model, where $q = 1.6$, $\tau_s/\tau_0 = 5$, $h_0/\tau_0 = 10$: (a) Normalized slip rate, $\dot{\gamma}(a/\dot{a})$ along C_1; (b) Normalized slip rate, $\dot{\gamma}(a/\dot{a})$ along C_2; (c) Normalized slip rate, $\dot{\gamma}(a/\dot{a})$ along C_3; (d) Normalized slip rate, $\dot{\gamma}(a/\dot{a})$ along C_4.

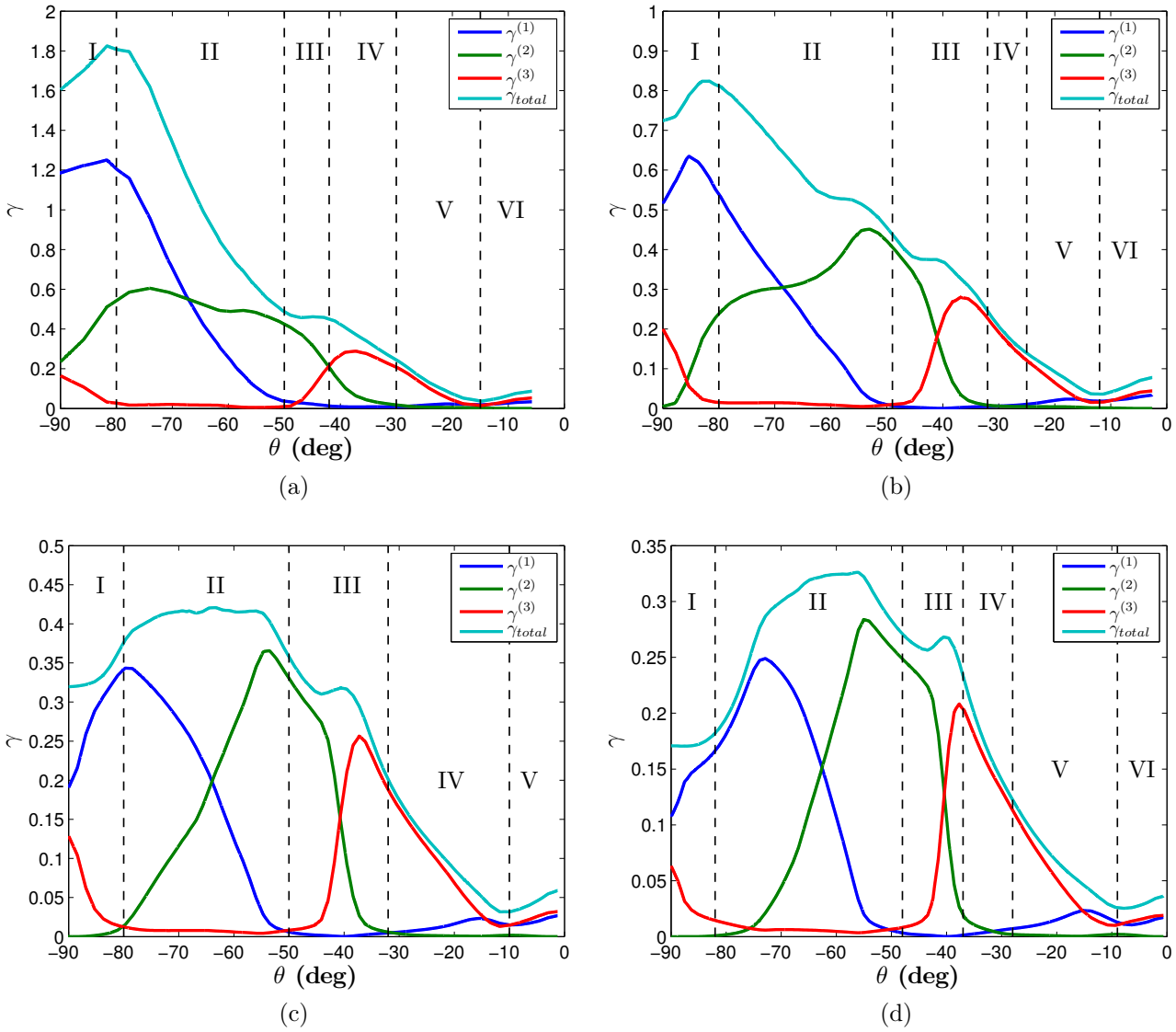

Figure 3.10: Total plastic strain (γ_{total}) and the plastic strain on each effective slip system ($\gamma^{(1)}$, $\gamma^{(2)}$, and $\gamma^{(3)}$) obtained from BW hardening model, where $q = 0$, $\tau_s/\tau_0 = 1.24$, $h_0/\tau_0 = 0.7$, $h_s/\tau_0 = 38.7$, $\gamma_0 = 0.001$, $f_0 = 7.2$: (a) Plastic strain, γ along C_1; (b) Plastic strain, γ along C_2; (c) Plastic strain, γ along C_3; (d) Plastic strain, γ along C_4.

single slips are observed in the deformed single crystal. In this case, the *Slip System 1* and *3* are active together in I, and the *Slip System 1* and *2* are active together in II, only the *Slip System 2* is active in III, the *Slip System 2* and *3* are active together in IV, and only the *Slip System 3* is active in V. The significant difference between the BW and the PAN Hardening Models occurs in the first region. Whereas only the *Slip System 1* was active in the PAN Simulations, the *Slip System 1* and *3* is active in region I. This is valid for Fig. 3.11(c) and Fig. 3.11(d). Since there are some variations in Fig. 3.11(a) and Fig. 3.11(b) where the 90-degree arcs are close to the highly deformed indented region, the information obtained from the Fig. 3.11(c) and Fig. 3.11(d) is utilized to compare the slip activity regions.

Plastic Strains and Slip Rates Associated with the BW Simulation #6

An analysis, which is similar to the one in Subsection 3.3.5, was carried out to interpret the outcomes of the BW Simulation #6, where $q = 0$, $\tau_s/\tau_0 = 1.3$, $h_0/\tau_0 = 1.5$, $h_s/\tau_0 = 90$, $\gamma_0 = 0.001$, $f_0 = 8$. The variations of the plastic strains along the arcs are shown in Fig. 3.12, where the amount of the total plastic strains are nearly 2% less than those obtained from the BW Simulation #5 as illustrated in Fig. 3.10.

Similarly, the normalized slip rates are illustrated in Fig. 3.13 to investigate the activity regions of the slip systems. It can be seen that the *Slip System 1* and *3* are active together in I, and the *Slip System 1* and *2* are active together in II, only the *Slip System 2* is active in III, the *Slip System 2* and *3* are active together in IV, and finally, only the *Slip System 3* is active in V.

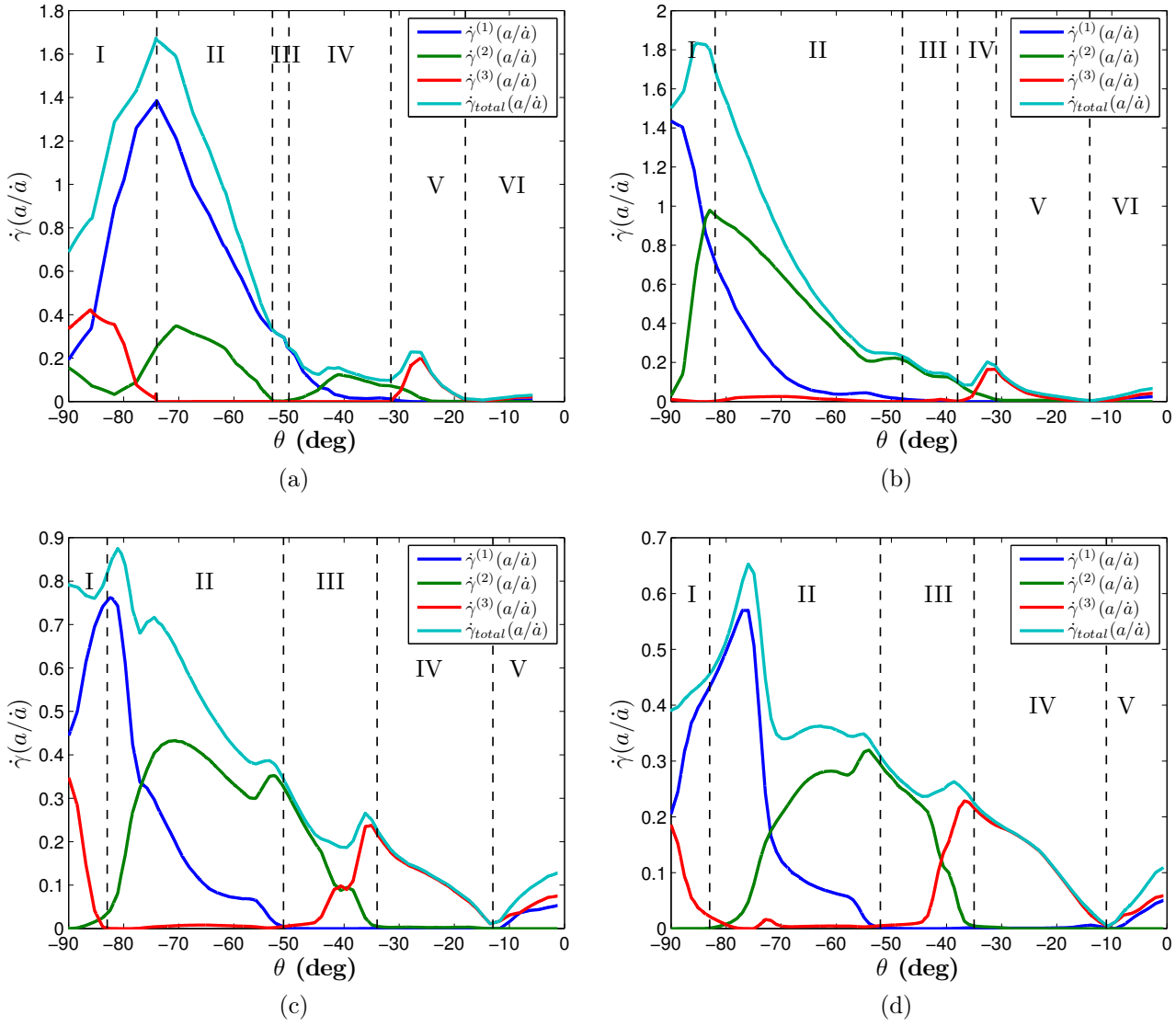

Figure 3.11: Total normalized slip rate ($\dot{\gamma}_{total}(a/\dot{a})$) and the normalized slip rate of each effective slip system ($\dot{\gamma}^{(1)}(a/\dot{a})$, $\dot{\gamma}^{(2)}(a/\dot{a})$, and $\dot{\gamma}^{(3)}(a/\dot{a})$) obtained from BW hardening model, where $q = 0$, $\tau_s/\tau_0 = 1.24$, $h_0/\tau_0 = 0.7$, $h_s/\tau_0 = 38.7$, $\gamma_0 = 0.001$, $f_0 = 7.2$: (a) Normalized slip rate, $\dot{\gamma}(a/\dot{a})$ along C_1; (b) Normalized slip rate, $\dot{\gamma}(a/\dot{a})$ along C_2; (c) Normalized slip rate, $\dot{\gamma}(a/\dot{a})$ along C_3; (d) Normalized slip rate, $\dot{\gamma}(a/\dot{a})$ along C_4.

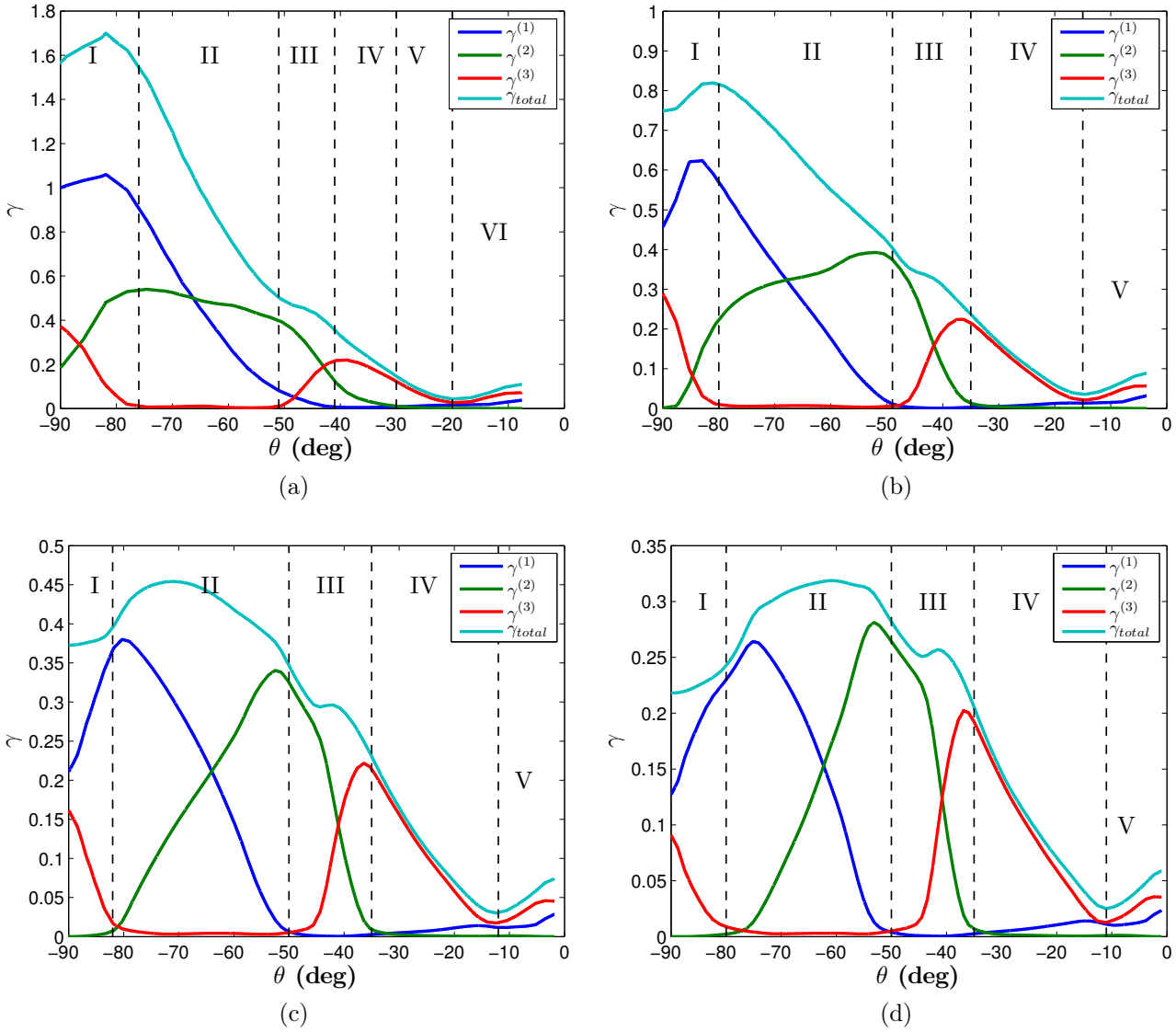

Figure 3.12: Total plastic strain (γ_{total}) and the plastic strain on each effective slip system ($\gamma^{(1)}$, $\gamma^{(2)}$, and $\gamma^{(3)}$) obtained by BW hardening model, where $q = 0$, $\tau_s/\tau_0 = 1.3$, $h_0/\tau_0 = 1.5$, $h_s/\tau_0 = 90$, $\gamma_0 = 0.001$, $f_0 = 8$: (a) Plastic strain, γ along C_1; (b) Plastic strain, γ along C_2; (c) Plastic strain, γ along C_3; (d) Plastic strain, γ along C_4.

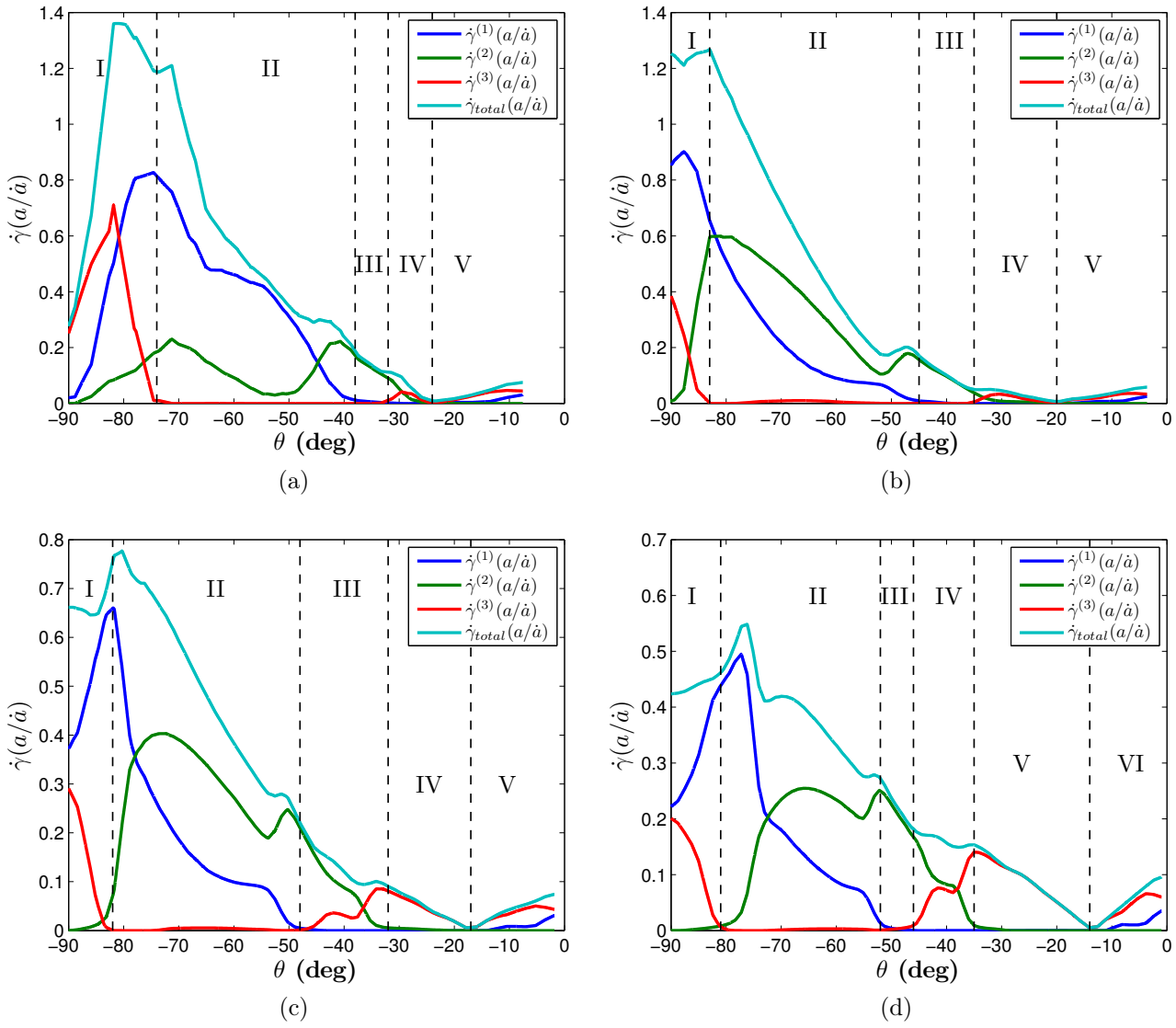

Figure 3.13: Total normalized slip rate ($\dot{\gamma}_{total}(a/\dot{a})$) and the normalized slip rate of each effective slip system ($\dot{\gamma}^{(1)}(a/\dot{a})$, $\dot{\gamma}^{(2)}(a/\dot{a})$, and $\dot{\gamma}^{(3)}(a/\dot{a})$) obtained from BW hardening model, where $q = 0$, $\tau_s/\tau_0 = 1.3$, $h_0/\tau_0 = 1.5$, $h_s/\tau_0 = 90$, $\gamma_0 = 0.001$, $f_0 = 8$: (a) Normalized slip rate, $\dot{\gamma}(a/\dot{a})$ along C_1; (b) Normalized slip rate, $\dot{\gamma}(a/\dot{a})$ along C_2; (c) Normalized slip rate, $\dot{\gamma}(a/\dot{a})$ along C_3; (d) Normalized slip rate, $\dot{\gamma}(a/\dot{a})$ along C_4.

3.3.6 Yield Surface Analysis

An anisotropic material that undergoes the plane strain deformation, the yield condition can be represented by the stress space (Rice [63]). In other words, the stress space is defined by the relation between $\left(\sigma_{11}^{'} - \sigma_{22}^{'}\right)/2$ and $\sigma_{12}^{'}$, and for plane strain deformation state, the relation can be expressed as

$$\mid -2S_1^{(\alpha)}S_2^{(\alpha)}\left(\frac{\sigma_{11}^{'} - \sigma_{22}^{'}}{2}\right) + \left(S_1^{(\alpha)}S_1^{(\alpha)} - S_2^{(\alpha)}S_2^{(\alpha)}\right)\sigma_{12}^{'} \mid = \tau_{CRSS}^{(\alpha)}, \tag{3.1}$$

where S_1 and S_2 are the components of the slip direction of a slip system α, and τ_{CRSS} is the critical resolved shear stress associated with each slip system. Eq. 3.1 denotes that if the resolved shear stress on a slip system reaches a critical value, then that specific slip system is activated. For the first slip system (i.e. $\alpha = 1$), the Eq. 3.1 can be rewritten as

$$\left(S_1N_2 + S_2N_1\right)\sigma_{12}^{'} + 2S_1N_1\frac{\left(\sigma_{11}^{'} - \sigma_{22}^{'}\right)}{2} = \pm\lambda_1\tau_{CRSS}, \tag{3.2}$$

by taking into account that $S_1 = \cos\phi$, $S_2 = \sin\phi$, $N_1 = -S_2$, and $N_2 = S_1$. λ_1 in the Eq. 3.2 is the geometric parameter for *Slip System 1*, which was defined in Chapter 2. The Eq. 3.2 can be reduced to a linear equation, which can be expressed as

$$\sigma_{12}^{'} = \tan 2\phi\left[\frac{\sigma_{11}^{'} - \sigma_{22}^{'}}{2}\right] \pm \frac{\lambda_1\tau_{CRSS}}{\cos 2\phi}, \tag{3.3}$$

where $\sigma_{12}^{'}$ and $\left(\sigma_{11}^{'} - \sigma_{22}^{'}\right)/2$ are the stresses in the global coordinate frame. In this study, we constructed the yield surfaces in the local crystallographic coordinate frame by means of the trigonometric relations and the two-dimensional stress transformation rules as follows:

$$\sigma_{11} = \sigma_{11}'\cos^2\omega_3 + \sigma_{22}'\sin^2\omega_3 + 2\sigma_{12}'\cos\omega_3\sin\omega_3, \tag{3.4a}$$

$$\sigma_{22} = \sigma_{22}'\cos^2\omega_3 + \sigma_{11}'\sin^2\omega_3 - 2\sigma_{12}'\cos\omega_3\sin\omega_3, \tag{3.4b}$$

$$\sigma_{12} = (\sigma_{22}' - \sigma_{11}')\cos\omega_3\sin\omega_3 + \sigma_{12}'(\cos^2\omega_3 - \sin^2\omega_3). \tag{3.4c}$$

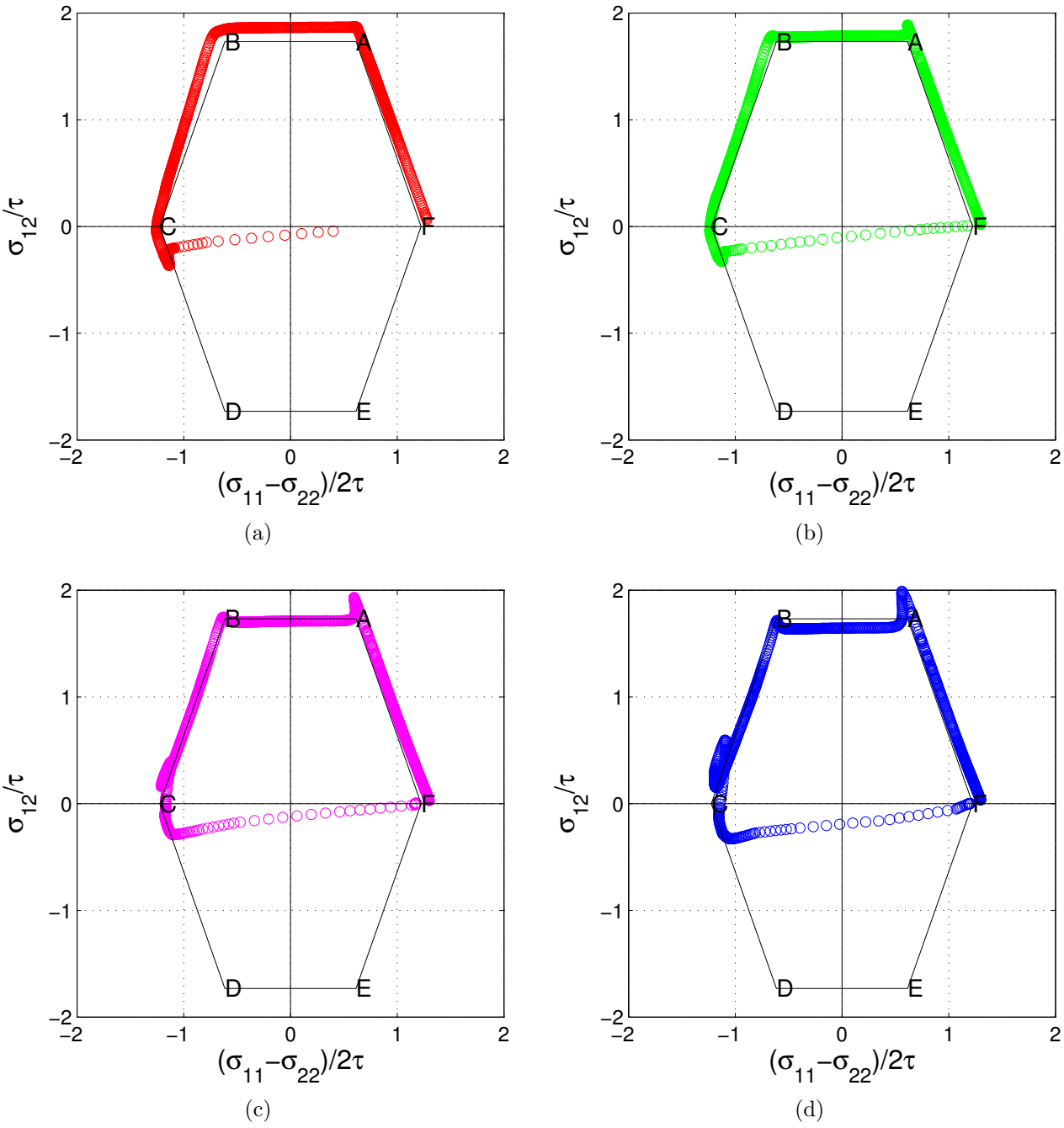

Figure 3.14: Yield surfaces along C_1 : (a) PAN Simulation#1, where $q = 1.0$, $\tau_s/\tau_0 = 5$, $h_0/\tau_0 = 10$; (b) PAN Simulation#5, where $q = 1.2$, $\tau_s/\tau_0 = 5$, $h_0/\tau_0 = 10$; (c) PAN Simulation#6, where $q = 1.4$, $\tau_s/\tau_0 = 5$, $h_0/\tau_0 = 10$; (d) PAN Simulation#7, where $q = 1.6$, $\tau_s/\tau_0 = 5$, $h_0/\tau_0 = 10$.

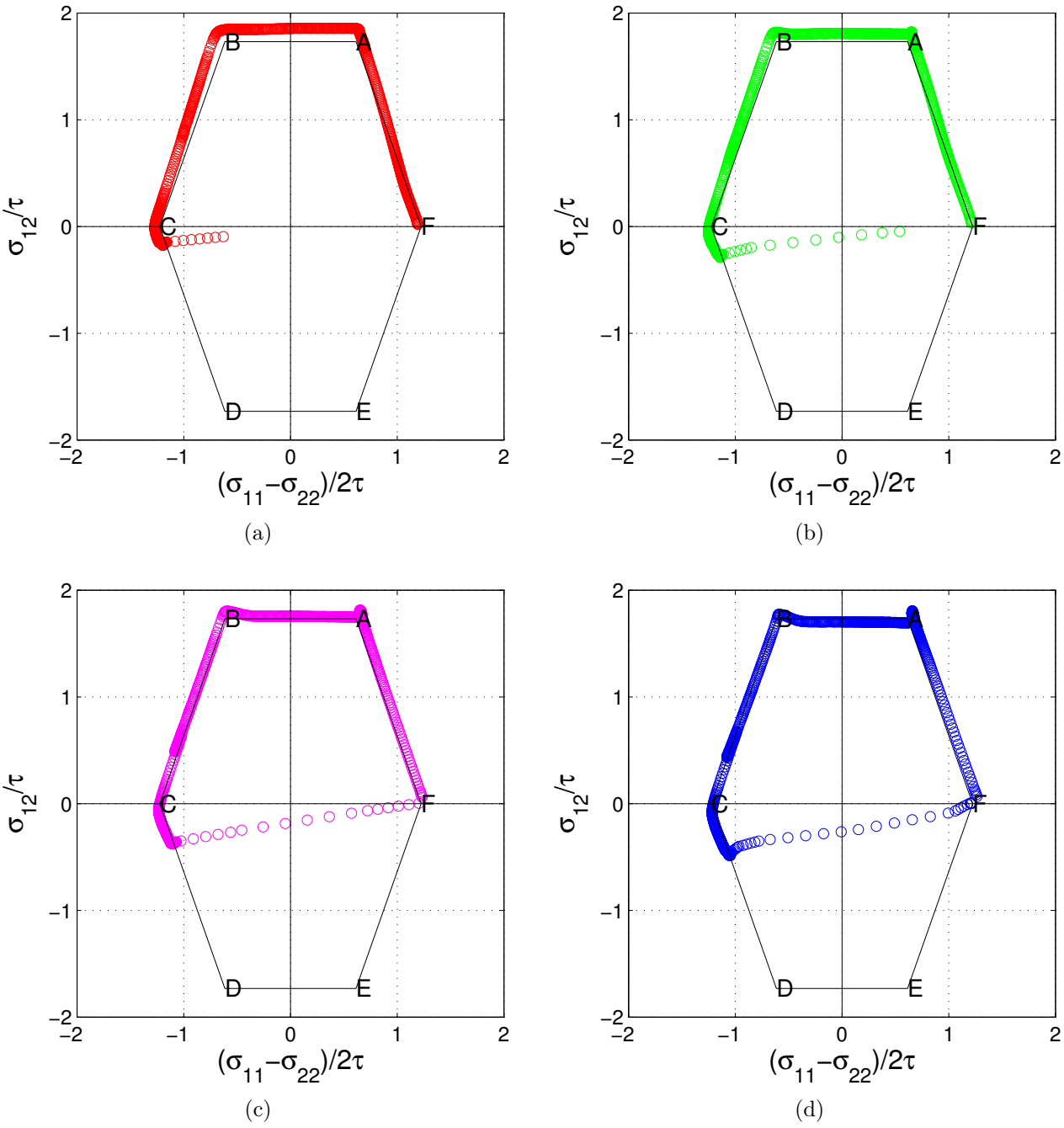

Figure 3.15: Yield surfaces along C_2: (a) PAN Simulation#1, where $q = 1.0$, $\tau_s/\tau_0 = 5$, $h_0/\tau_0 = 10$; (b) PAN Simulation#5, where $q = 1.2$, $\tau_s/\tau_0 = 5$, $h_0/\tau_0 = 10$; (c) PAN Simulation#6, where $q = 1.4$, $\tau_s/\tau_0 = 5$, $h_0/\tau_0 = 10$; (d) PAN Simulation#7, where $q = 1.6$, $\tau_s/\tau_0 = 5$, $h_0/\tau_0 = 10$.

The yield surfaces were constructed by taking $(\sigma_{11} - \sigma_{22})/2\tau$ as horizontal axis and σ_{12}/τ as vertical axis, and the variations of the stresses along C_1, C_2, C_3, and C_4 were calculated to create yield surfaces as shown in Fig. 3.14, Fig. 3.15, Fig. 3.16, and Fig. 3.17, respectively. If the variations of the stresses are located on the facets or the outside of the yield surface, then slip systems become activated due to the resulting shear stress, which is greater than the critical resolved shear stress. The other points, which are located inside the yield surfaces, experience elastic deformation and the resulting shear stresses are smaller than the critical resolved shear stress. The yield surfaces analyzed in Fig. 3.14, Fig. 3.15, Fig. 3.16, and Fig. 3.17 are associated with the PAN Simulations #1, #5, #6 and #7, which have a good agreement with the experimental β-fields. Whereas the stress variations along the yield surfaces, which are illustrated in Fig. 3.14, Fig. 3.15, are a bit off the facets of the yield surfaces, those illustrated in Fig. 3.16, and Fig. 3.17 are located on the facets of the yield surfaces. This can be attributed to the extensive plastic deformation occurred in the vicinity of the indenter tip.

Fig. 3.14, Fig. 3.15, Fig. 3.16, and Fig. 3.17 show that we obtain limited information about the state of the material through yield surface analysis. In other words, we do not know what material points are located at the vertices (A, B, C, D, E, F) of the yield surface, where the double slip occurs. The vertices F, A, B, and C indicate the locations of the double slips, where *Slip Systems 1 and 3*, *Slip Systems 1 and 2*, *Slip Systems 2 and 3*, and *Slip Systems 3 and 1*, are activated respectively. Fig. 3.14, Fig. 3.15, Fig. 3.16, and Fig. 3.17 do not give the yield response of the individual material points, which are located on the 90-degree arcs. In order to get the state of the material points at different θ angles, a new analysis was performed by dividing the yield surface into nine line segments. Each line segment is in between the two letters (a, b, c, d, e, f, g, h, i, j), and each letter represents an angle value from -90°to 0°as shown in Fig. 3.18 and Fig. 3.19. For instance, for the material point which is located at $\theta = -90^0$, point a indicates the location of that material point on

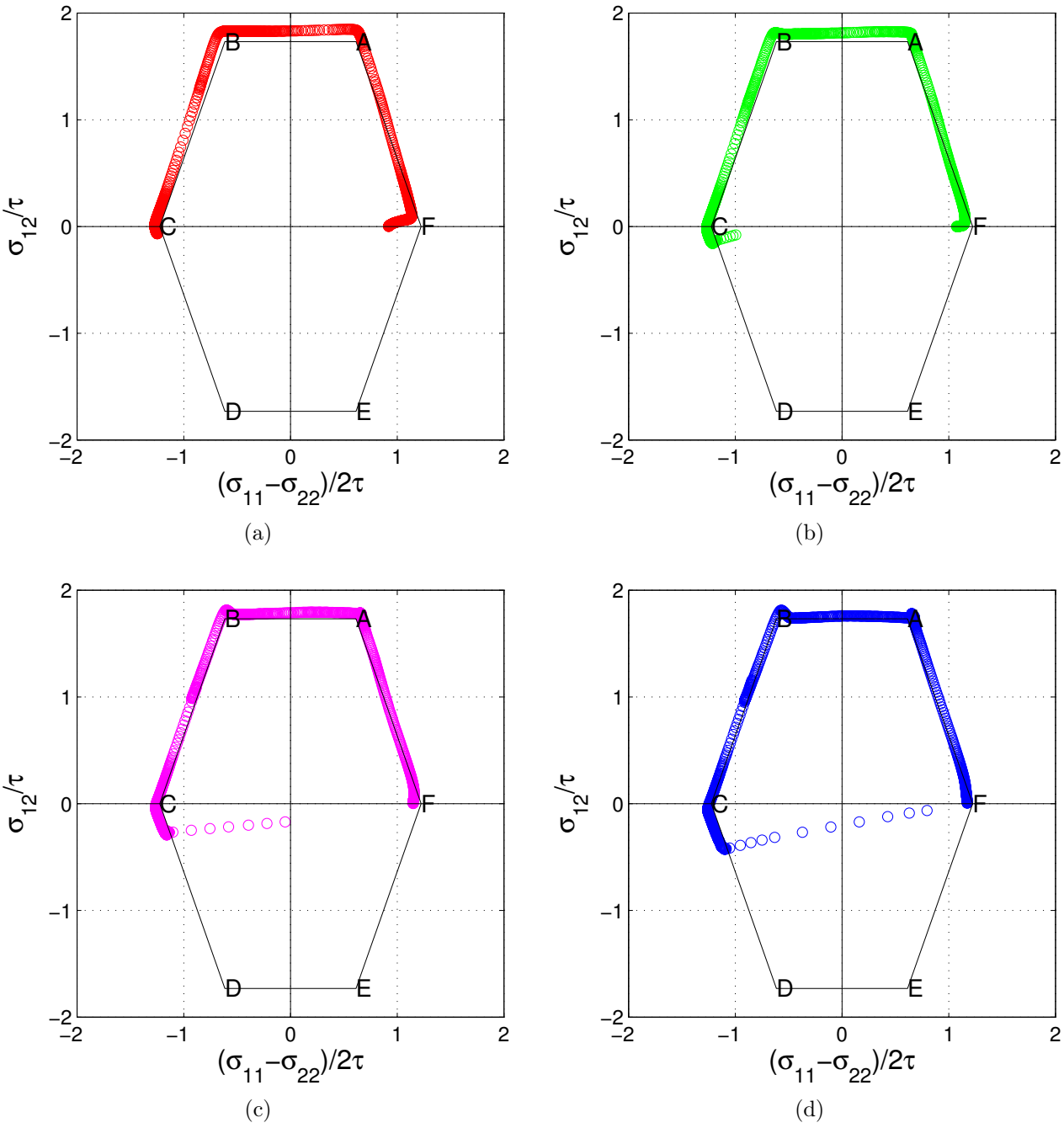

Figure 3.16: Yield surfaces along C_3 : (a) PAN Simulation#1, where $q = 1.0$, $\tau_s/\tau_0 = 5$, $h_0/\tau_0 = 10$; (b) PAN Simulation#5, where $q = 1.2$, $\tau_s/\tau_0 = 5$, $h_0/\tau_0 = 10$; (c) PAN Simulation#6, where $q = 1.4$, $\tau_s/\tau_0 = 5$, $h_0/\tau_0 = 10$; (d) PAN Simulation#7, where $q = 1.6$, $\tau_s/\tau_0 = 5$, $h_0/\tau_0 = 10$.

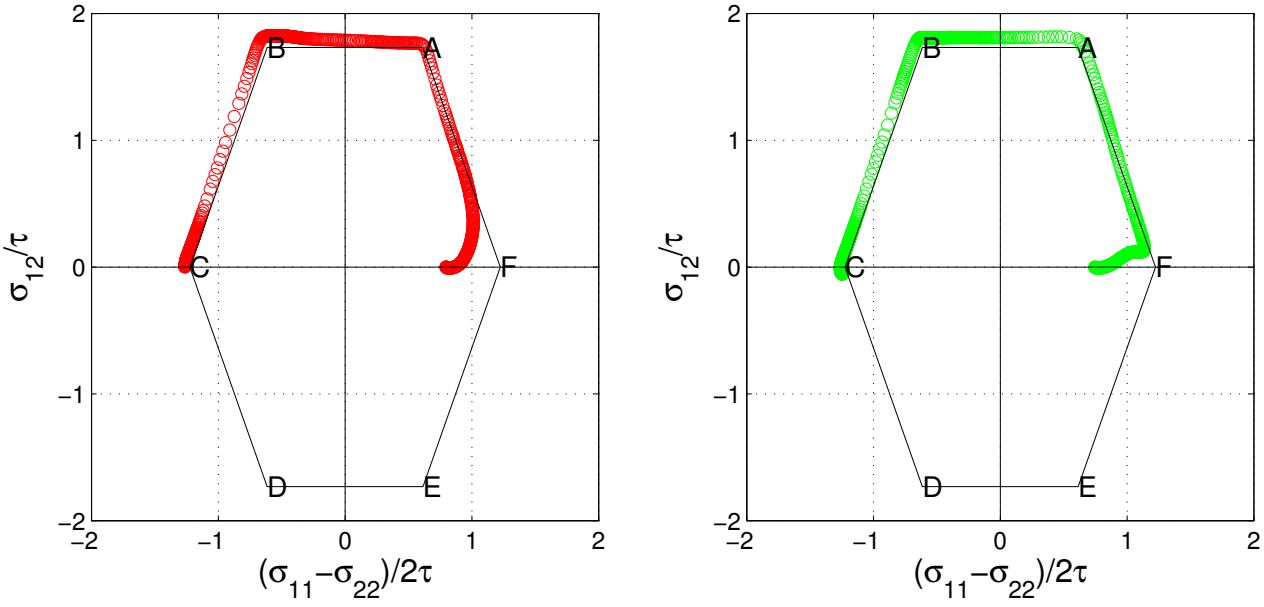

(a)

(b)

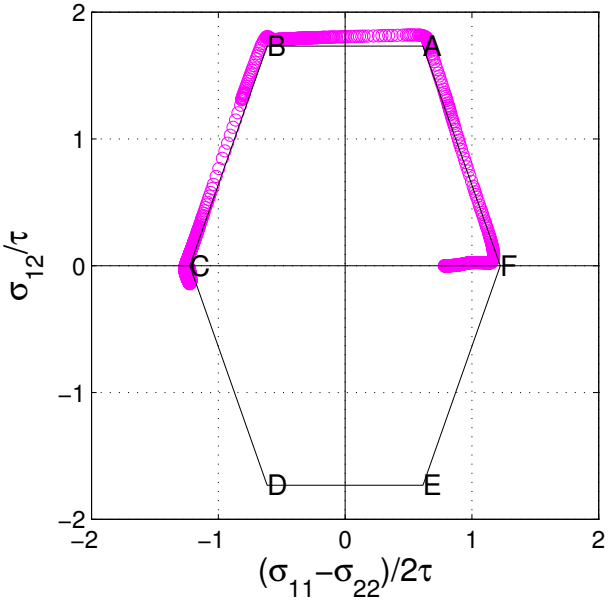

(c)

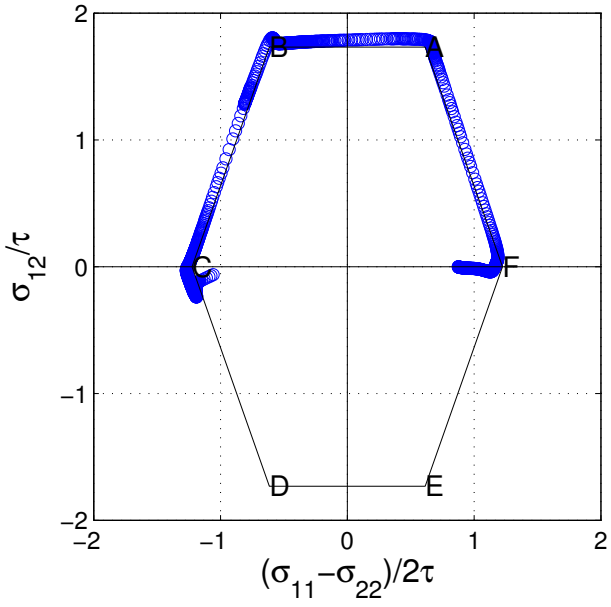

(d)

Figure 3.17: Yield surfaces along C_4 : (a) PAN Simulation#1, where $q = 1.0$, $\tau_s/\tau_0 = 5$, $h_0/\tau_0 = 10$; (b) PAN Simulation#5, where $q = 1.2$, $\tau_s/\tau_0 = 5$, $h_0/\tau_0 = 10$; (c) PAN Simulation#6, where $q = 1.4$, $\tau_s/\tau_0 = 5$, $h_0/\tau_0 = 10$; (d) PAN Simulation#7, where $q = 1.6$, $\tau_s/\tau_0 = 5$, $h_0/\tau_0 = 10$.

yield surface, and we can get direct information about the elastic-plastic behavior associated with that material point. This analysis allows us to get finer information about the material state by analyzing the mechanical behavior of 10 different material points.

The ratio of the individual slip to the total slip (i.e. $\gamma^{(1)}/\gamma_{total}$, $\gamma^{(2)}/\gamma_{total}$, $\gamma^{(3)}/\gamma_{total}$) were calculated, and the ratios were obtained along C_1, C_2, C_3, and C_4 for PAN Simulation #6 and #7. An approach recently presented by Dahlberg et al. [16] was used in order to determine the activity regions of the slip systems by evaluating the ratios, $\gamma^{(1)}/\gamma_{total}$, $\gamma^{(2)}/\gamma_{total}$, and $\gamma^{(3)}/\gamma_{total}$. According to the approach, if the ratio associated with a particular slip system is greater than 95%, then that particular slip system is predominantly active, and if any of the ratios are less than 5%, the activation of the slip system is assumed to be negligible. If the ratios vary between 0.95 and 0.05, then double slips are active so that 0.95 and 0.05 are set as upper and lower limits as shown in Fig. 3.20 and Fig. 3.21. Fig. 3.20(a) shows that there are four different slip activity regions, where *Slip System 1* and *Slip System 2* are active in region I, only *Slip System 2* is active in region II, *Slip System 2* and *Slip System 3* are active in region III, and *Slip System 1* and *Slip System 3* are active in region IV. Fig. 3.20(b) illustrates that one additional activity region (region IV), where only the *Slip System 3* is active. And finally, it can be seen that Fig. 3.20(c) and Fig. 3.20(d) indicates that there are six different slip activity regions away from the indenter tip. This also points out that whereas the characteristics of the slip systems (*Slip System 1*, *Slip System 1 and 2*, *Slip System 2*, *Slip System 2 and 3*, *Slip System 3*, *Slip System 1 and 3*) are similar, the boundaries of the activity regions (i.e. the areas of the activity regions) are different for the cases which are shown in Fig. 3.20(c) and Fig. 3.20(d). Same activity regions can be seen in Fig.3.21(a), Fig.3.21(b), Fig.3.21(c), and Fig.3.21(d), but the boundaries of the activity regions are slightly different.

Now we can turn our attention back to the Fig. 3.18 and Fig. 3.19 to obtain a detailed information about the state of the material by comparing the activity maps as shown in Fig. 3.20 and Fig. 3.21, which are generated by employing the approach described above,

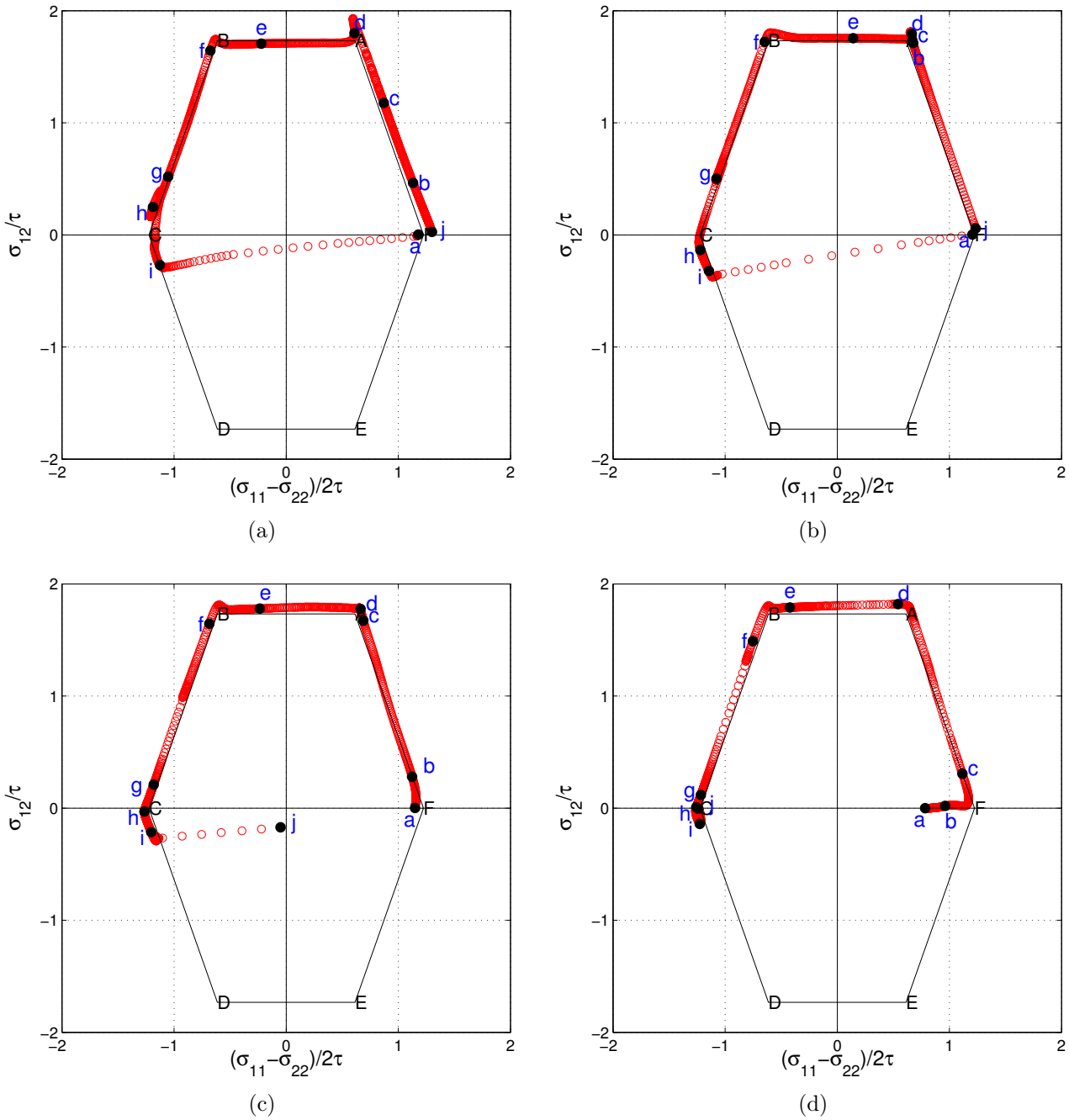

Figure 3.18: Yield surfaces along C_1, C_2, C_3, C_4 for PAN Simulation#6, where $q = 1.4$, $\tau_s/\tau_0 = 5$, $h_0/\tau_0 = 10$. Yield surfaces along each 90-degree arc-length are divided into nine line segments. Each line segment is in between the two letters (a,b,c,d,e,.....j), and each letter represents an angle value from -90 to 0°; (a) Yield surface along C_1; (b) Yield surface along C_2; (c) Yield surface along C_3; (d) Yield surface along C_4.

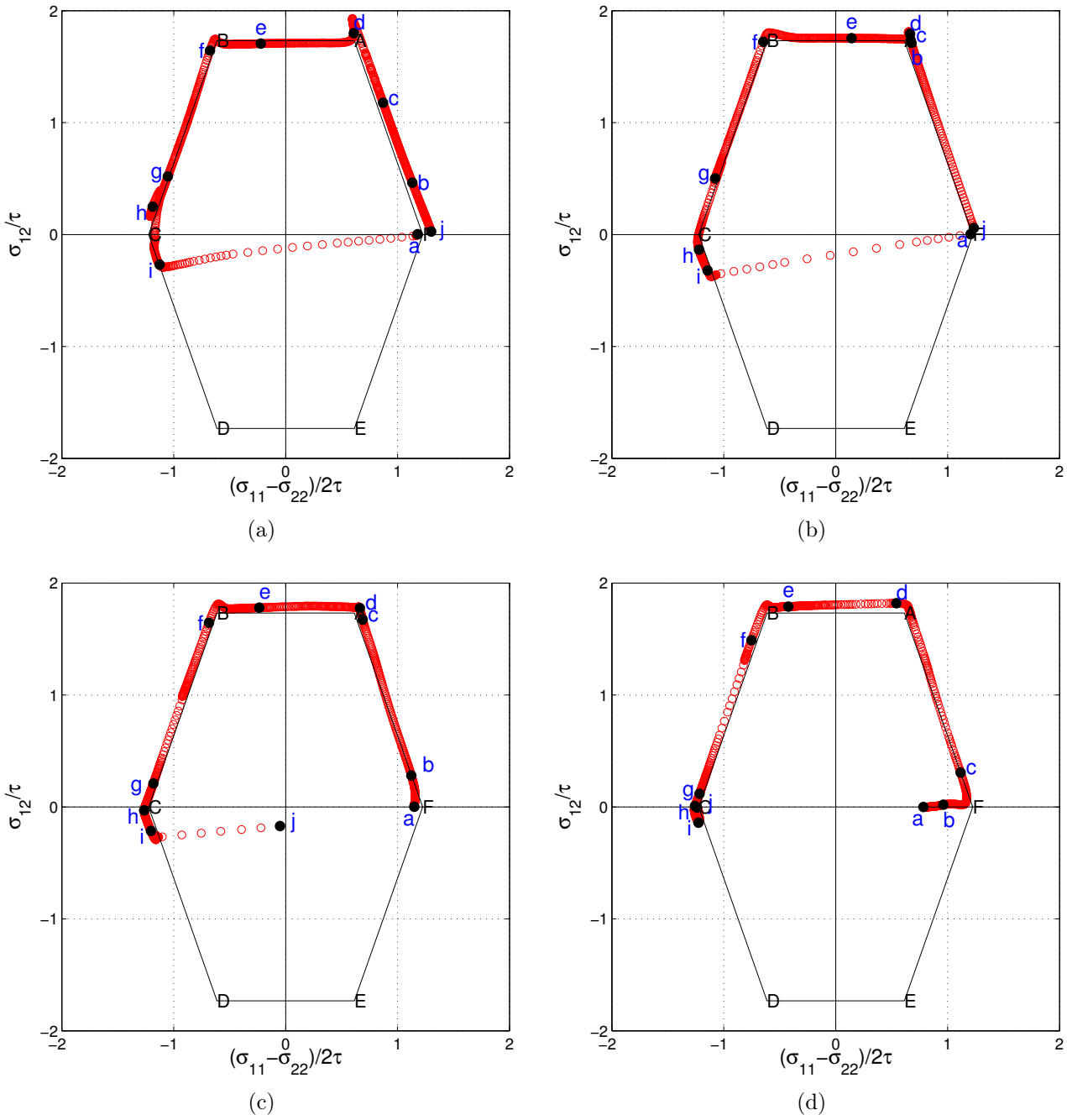

Figure 3.19: Yield surfaces along C_1, C_2, C_3, C_4 for PAN Simulation#7, where $q = 1.6$, $\tau_s/\tau_0 = 5$, $h_0/\tau_0 = 10$. Yield surfaces along each 90-degree arc-length are divided into nine line segments. Each line segment is in between the two letters (a,b,c,d,e,.....j), and each letter represents an angle value from -90 to 0°; (a) Yield surface along C_1; (b) Yield surface along C_2; (c) Yield surface along C_3; (d) Yield surface along C_4.

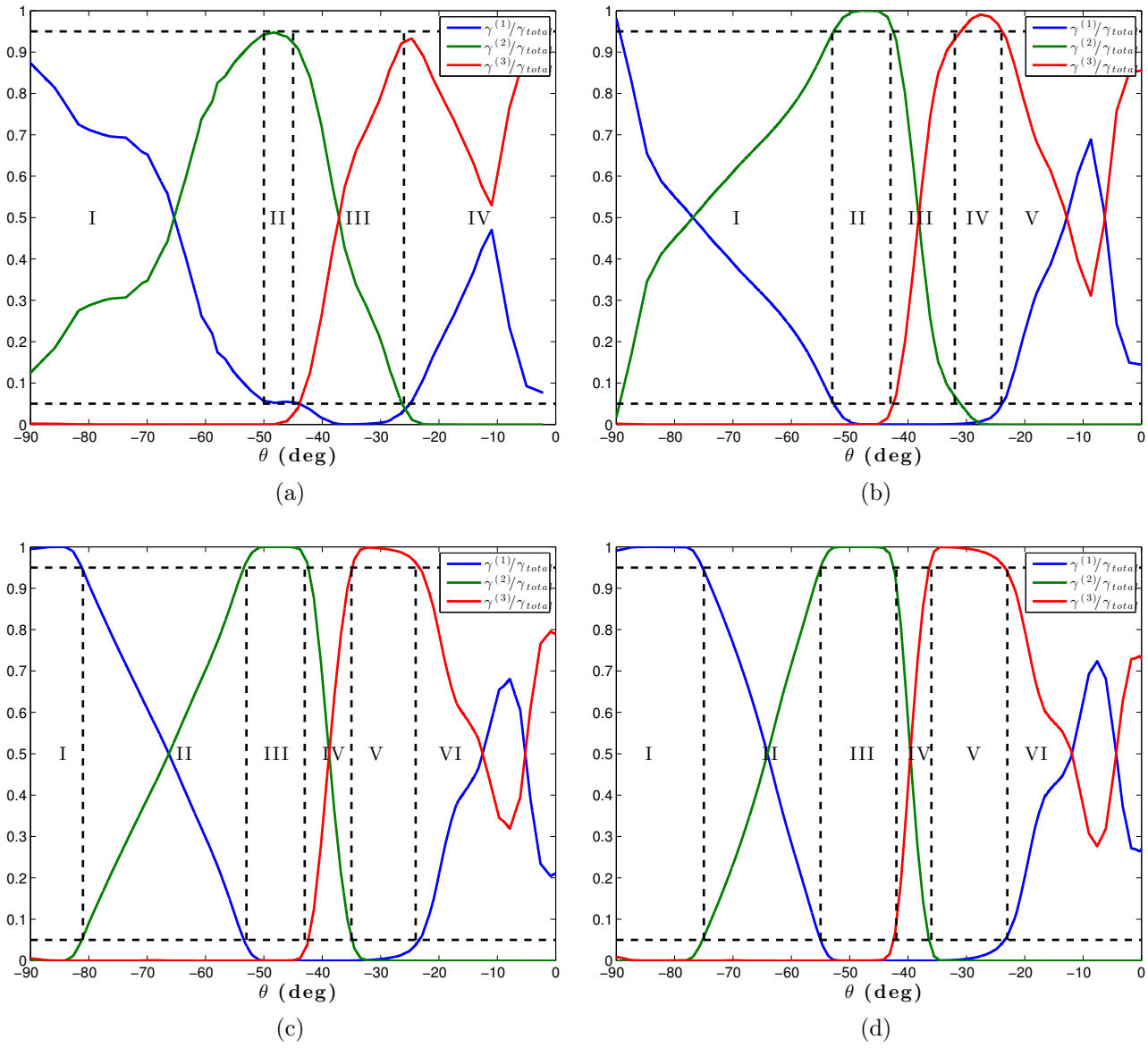

Figure 3.20: Comparison of percentages of plastic strains associated with PAN Simulation#6. Upper and lower limits marked on the vertical axis are 0.95, and 0.05, respectively: (a) Percentage of plastic strains along C_1; (b) Percentage of plastic strains along C_2; (c) Percentage of plastic strains along C_3; (d) Percentage of plastic strains along C_4

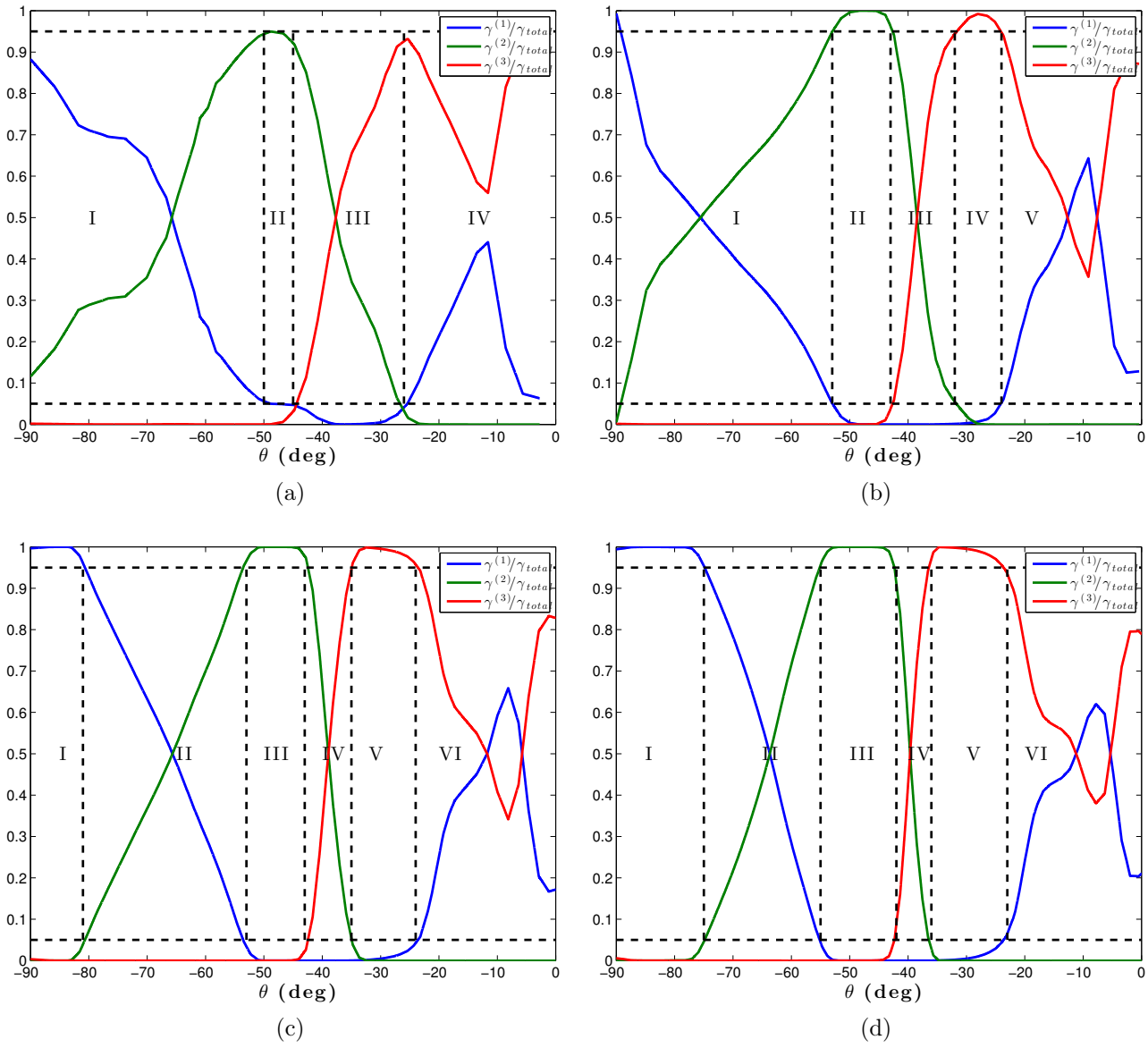

Figure 3.21: Comparison of percentages of plastic strains associated with PAN Simulation#7. Upper and lower limits marked on the vertical axis are 0.95, and 0.05, respectively: (a) Percentage of plastic strains along C_1; (b) Percentage of plastic strains along C_2; (c) Percentage of plastic strains along C_3; (d) Percentage of plastic strains along C_4

with the yield surfaces as shown in Fig. 3.18 and Fig. 3.19. Let take the Fig. 3.19 and Fig. 3.21 for comparison. Point a represents the stress state of the material point at $\theta = -90°$, and it can be seen that only the *Slip System 1* is active associated with the material point at $\theta = -90°$ as shown in Fig. 3.21(c). Points b and c associated with the material points located at $\theta = -80°$ and $\theta = -70°$, where *Slip System 1* is dominantly active as shown in Fig. 3.21(c). Point d represents the stress state of the material point located at $\theta = -60°$, and *Slip System 2* is dominantly active for that material point. Therefore, a, b, c, and d are located on the one facet of the yield surface, where *Slip System 1* is dominantly active. Point e represents the yielding response of the material point located at $\theta = -50°$, where only *Slip System 2* is active, and point f belongs to the stress variation associated with the material point at $\theta = -40°$, where *Slip System 3* is dominantly active. For point g only *Slip System 3* is active, for point h at the vertex of the yield surface *Slip System 3 and 1* are active together. Point i indicates that only *Slip System 1* is active associated with the material point located at $\theta = -10°$. It can be seen that point j is inside the yield surface so that the material point is undergoing an elastic deformation.

The state of the material can be understood by employing the ten-degree yield surface analysis as illustrated in Fig. 3.18 and Fig. 3.19, and the slip activity maps as shown in Fig. 3.20 and Fig. 3.21. These illustrations give us very detailed information about the state of the material, where the stress spaces obtained along C_3 and C_4 represent the elastic-plastic behavior of the single crystal away from the indenter tip. C_3 and C_4 represent the distances, where we cannot observe the effect of the shape of the indenter tip Dahlberg et al. [16]. This verifies the results associated with the analysis of the slip activity regions obtained from the β-fields.

3.4 Conclusions

A parametric analysis was performed to understand how β-variable is sensitive to the hardening parameters such as latent hardening ratio, saturation stress, and initial hardening modulus, and how $\beta-$variable alters when the hardening parameters change. The results were given for two hardening rules, which are employed in Finite Element Simulations. β-variable was monitored on the β-fields along the 90-degree arcs that have the radii of 1.5, 2.0, 2.5, 3.0 times the maximum depth of indentation. In order to get a detailed information about the state of the material, dimensionless slip rates, ten-degree yield surface analysis, and finally slip activity mapping were performed. The results obtained from the analysis associated with the slip activity regions point out that the $\beta-$variable can be used as a validation parameter in elastic-plastic constitutive models.

Chapter 4

Length Scale for Dislocation Cell Size and Cell Wall Width using SEM-based Continuum Methods and Fourier Transform

4.1 Introduction

The studies conducted up to this point is basically on the understanding of the state of the deformed nickel single crystal, under specific loading condition such that a line load parallel to the [110] direction of the crystal specimen was applied into the (001) surface of the specimen by a tungsten carbide wedge indenter with an included angle of 90°. Three effective in-plane slip systems were activated through the indentation process maintaining 2-D plane-strain conditions after the indentation of 160 μm. A well-defined spatially resolved net Burgers density vector was obtained to analyze the activity of the slip systems to get finer and detailed information about the single crystal under the small scale yielding and two dimensional plane strain conditions. A validation parameter, β, which was previously

introduced in order for the elastic-plastic constitutive relations, was utilized to monitor the activity of the slip systems. This parameter chiefly represents the orientation of the net Burgers density vector on a deformed surface as explained in detail in Chapter 2. After obtaining the mechanical behavior of the material using β-fields, the next question is what the dislocation densities will be inside the material in the small scale, and what length scale best describes the relationship between the dislocation mean free path and the thickness of the dislocation cell wall that can be identified as shown in Fig. 4.1.

Our objective in this study is to define a length scale parameter between the dislocation cell size and cell wall width using the data obtained with 2500 nm, 500 nm, and 100 nm spatial resolutions through HR-EBSD (High Resolution Electron Back-Scattered Diffraction). Dislocation cell sizes were measured via TEM (Transmission Electron Microscopy) previously by Griffiths and Riley [28], Pratt [62], Langford and Cohen [47], Staker and Holt [67], Murr [52], Moin and Murr [51], Knoesen and Kritzinger [38], Koneva et al. [40], and a relation between the dislocation cell size and the dislocation density was investigated. According to the TEM micrographs obtained through these studies, the maximum cell wall width was about hundreds of nanometers in the small scale. This study presents a new technique to define a length scale for dislocation cell size and the cell wall width by performing meso-scale measurements, which cannot be obtained by TEM methods.

The dislocation characteristics pertaining to each effective slip system were obtained through SEM and HR-EBSD, and the Geometrically Necessary Dislocation (GND) densities for three effective slip systems were calculated using SEM-based continuum methods through the experimental lower bound solution [46]. To obtain the lower bound solution for geometrically necessary dislocation densities, Nye's tensor components, which serve as a link between elastic-plastic constitutive relations, were calculated. The non-zero components of the Nye's dislocation density tensor are utilized to obtain both β-fields and lower bound solution for geometrically necessary dislocation densities corresponding to three effective slip systems so that one can easily get the overall information about the state of the material in meso-scale

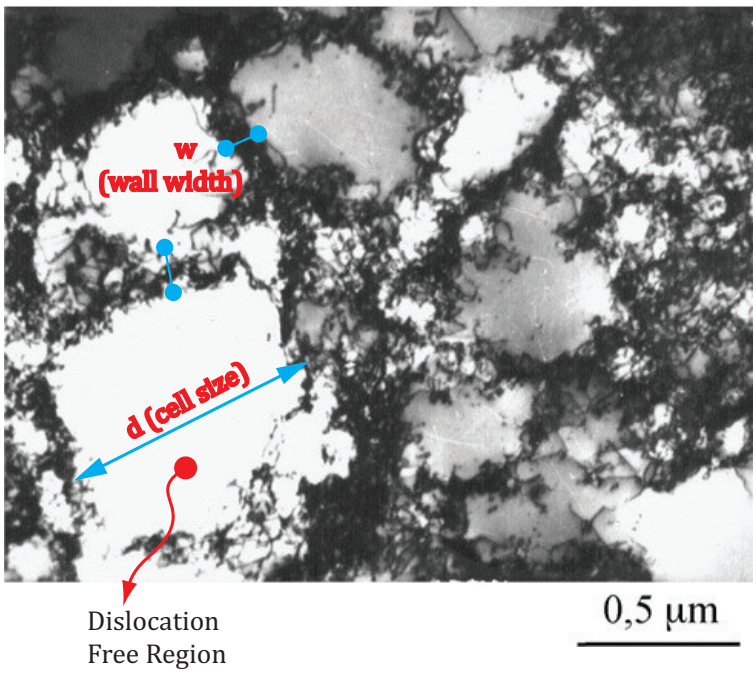

Figure 4.1: Dislocation cell size and cell wall width in a deformed Nickel Single Crystal ($\varepsilon = 0.16$, $T = 293K$) based upon Koneva et al. [40]

that cannot be determined via TEM methods.

The dislocation clusters inside the deformed nickel single crystal were obtained, and their quasi-periodic arrangements by forming the dislocation cells were observed. The dislocation-free paths, or dislocation free regions are separated by the walls of these dislocation cells, which are formed by the dislocation tangles. Fourier Transform (FT) is employed to calculate the dislocation cell size (dislocation cell mean diameter) and cell wall width by considering the quasi-periodic arrangement of dislocation densities. This process was carried out through four steps. First, the dislocation (geometrically necessary) density distributions as a function of position were collected along the as-deformed slip directions from experimental lower bound solution. Second, the density distributions were truncated, and interpolated according to the spatial resolutions or step sizes, which are 2500 nm, 500 nm, and 100 nm, respectively. Third, a bandpass filtering process was applied to the dislocation density distribution functions to filter out the undesired variations. The Fourier Transform was finally

applied to obtain the relation between the magnitude of the GND density and the spatial frequency. After applying the Fourier Transform solution, the peak geometrically necessary dislocation densities were obtained corresponding to the spatial period for each data set. The spatial period, where the peak geometrically necessary dislocation density observed, is twice the dislocation cell size or dislocation mean free path length that can be determined from the quasi-periodic arrangement of the GND densities. The dislocation cell sizes were calculated using Fourier Transform for each data set obtained along the slip directions. The relationship between the peak dislocation density and the dislocation cell size for each data was plotted in logarithmic scale for the spatial resolutions of 2500 nm, 500 nm, and 100 nm. The reciprocal square root of the peak dislocation density, which is also called dislocation spacing, was calculated for each data set. A relationship between the dislocation cell size and the dislocation spacing was determined. A linear relationship between these two variables was observed. The slope of the linear curve was calculated, and compared to the values, which were previously obtained by TEM micrographs. The results of the Fourier Transform analysis was utilized again to calculate the width of the dislocation cell walls, and by using a mathematical analogy for periodic functions, a length scale parameter was defined between the dislocation cell size and the dislocation cell wall width. A linear relationship was obtained between the dislocation cell size and the cell wall width.

The paper is organized as follows. The theoretical background is given in Section 4.2 along with an explanation of the terminology and a review of the previous studies. The measurements of the dislocation cell mean diameter and the thickness of the dislocation cell walls, which are presented in the studies listed in this section, were obtained through TEM, and the length scales derived from these measurements serve as a benchmark for the present study. Section 4.3, experimental background, mainly deals with the experimental setup and the loading conditions of the specimen including the measurement of the geometrically necessary dislocation densities. The calculations of the dislocation spacing, dislocation cell size and cell wall width using Fourier Transform of quasi-periodic arrangement of dislocation

density distributions are given in Section 4.4, and the results pertaining to the different spatial resolutions (2500 nm, 500 nm and 100 nm) are presented in Section 4.5. The linear relationships between the dislocation density and dislocation cell size, the dislocation spacing and dislocation cell size, and the dislocation cell size and cell wall width are also illustrated in this section. Concluding remarks are given in Section 4.6.

4.2 Theoretical Background

Holt [36] conducted a study to analyze the relationship between the dislocation cell size and dislocation-dislocation interaction distance. In the study, the driving force for the clustering of the dislocations was attributed to the minimum elastic energy of the dislocations in clustering regions. Holt analyzed a distribution function, which is a function of the position and dislocation density on the deformed surface of the metal, and only considered the parallel screw dislocations for an idealized case. The positive and negative sense of dislocations were assumed to be equal and no annihilation among them was taken for granted. A critical radial distance, where the dislocation distribution function beyond this position is zero, was taken. Holt evaluated the dominant wavelength of the density fluctuation using the elastic interaction energy and the velocity of the dislocations. The dominant wavelength of the density fluctuation was found to be proportional to the reciprocal square root of the dislocation density, $\rho^{-1/2}$, and its magnitude is approximately equal to the dislocation-dislocation interaction distance. Holt concluded that this dominant wavelength persists until the dislocation cells are well formed so that the cell diameter is assumed to be equal to the dominant wavelength. He compared his results to the cell size measurements obtained by TEM micrographs for Copper, Iron, and Aluminum. These measurements showed that the cell size, d, is proportional to the reciprocal square root of the dislocation density, $\rho^{-1/2}$. The study also evaluated the TEM measurements taken by several investigators to define a relationship between the normalized flow stress, σ/Gb, and the dislocation cell diameter, d.

A linear relationship was obtained between these variables.

Staker and Holt [67] investigated a relationship between the dislocation cell size and dislocation density in copper by deforming through tensile loading with varying temperatures such as 25, 250, 400, 500, 550, 600, 650, and 700°C. TEM measurements in this study revealed that while the dislocation cell size increases with increasing temperature, the dislocation density and the cell wall thickness decrease. Following the previous study (Holt [36]), a relationship between the cell diameter and the dislocation density was proposed for the pure metals. This relationship is given by $d = K\rho^{-1/2}$, where d is the dislocation cell size or dislocation cell diameter, $\rho^{-1/2}$ is the reciprocal square root of the dislocation density, and K is a constant. The relationship between the cell diameter and the dislocation density indicates a linear relationship on a plot having logarithmic axes, and the slope corresponding to this linear relationship was calculated as -0.5. In order to get the constant K in the equation above, the cell diameter and the reciprocal square root of the dislocation density results are presented in scatter plot indicating the linear relationship between these two variables by calculating K as 16. The relationship between the normalized flow stress, τ/Gb, and the cell size, d was also investigated in the study These variables obtained by TEM measurements of several investigators were plotted in a logarithmic scaled scatter plot. A linear relationship with a slope of approximately -1 was found such that the flow stress is inversely proportional to the dislocation cell size. They concluded that the results supported the *principle of similitude* proposed by Kuhlmann-Wilsdorf [41].

Knoesen and Kritzinger [38] performed a study to analyze the dislocation cell wall width and dislocation cell size in copper deformed by applying a tensile load. They utilized the TEM to measure the dislocation cell wall width for different cell sizes to investigate a relationship between the dislocation cell wall width and dislocation cell size. The circular thin specimens were cut perpendicular to the tensile axis to analyze the dislocation cell structure. A cut-off method was used to measure the dislocation cell size and cell wall width by drawing random lines on the TEM micrograph of dislocation cells. The average cell sizes and cell wall

width were obtained through the known length of these random lines. The measurements for cell wall width, w and cell size (diameter), d corresponding to annealed and strained, unannealed, and unannealed and strained specimens were plotted to extract a relationship between the two variables. A linear relationship, which is given by $w = 0.29d + 22$, was determined between the cell wall width and the cell diameter, which were measured in nm. Another set of measurements were also performed for the well formed cells, and a linear relationship, $w = 0.19d + 19$, was obtained, as well. They concluded that the dislocation cell wall width is approximately 30% of the dislocation cell diameter.

Koneva et al. [40] performed a quantitative analysis to investigate the dislocation cell size and the thickness of the cell wall of face-centred cubic metals and solid solutions. The study also investigated the influence of the grain size, temperature, and the strain on the dislocation substructures. They presented a quantitative relationship between the cell size and the dislocation density, and tabulated these relationships for three types of materials such as pure metal, solid solutions, and ordered solid solutions. The dislocation substructures of the Nickel Single Crystals at 77, 293, and 673K were also measured in order to determine a relationship between the cell size and the width of dislocation cell wall. Tensile and compression loads were applied to introduce deformation, and the dislocation structure was measured by utilizing a Transmission Electron Microscope to measure dislocation densities in the cell walls and their interiors. The dislocation cell size and the width of the cell walls were also measured. It was concluded that the cell wall width can decrease, increase or remain constant for different materials with an increase in strain. The coefficient of K was calculated in the range of $10-15.3$ for pure metals, and was calculated as 15 for Nickel Single Crystal at room temperature. The increase of K was observed in the range of $16-24$ with increasing temperature for pure metals. While the widths of the cell walls were measured in the range of $0.1-0.6$ μm, the cell sizes were measured in the range of $0.2-1.8$ μm for Nickel single crystal at 77, 293, and 673K. A linear relationship was obtained such that $H = \beta D$, where H is the width of the dislocation cell wall, D is the cell size, and β is a coefficient. The

β coefficient was calculated for Nickel single crystals in between 0.46 and 0.17 at different temperatures. They derived another quantity, C to express the relationship between the width of the cell wall, H and the reciprocal square root of dislocation density, $\rho^{-1/2}$. The linear relationship, which is given by $H = C\rho^{-1/2}$, was obtained after the measurements, and C was calculated as 3.5 and 6.2 for the temperatures of 673K and 77K, respectively.

The present study aims to investigate the relationship between the dislocation cell size and the cell wall width in meso-scale by employing SEM-based continuum methods and Fourier Transform. As can be seen from the previous studies explained in this section, the relationships were extracted using TEM-based discrete methods in the small length scale, and the GND densities cannot be distinguished from each other. Whereas the GND densities associated with individual slip systems, $\rho_{gnd}^{(1)}$, $\rho_{gnd}^{(2)}$ and $\rho_{gnd}^{(3)}$ can be identified and characterized by SEM-based continuum methods, they cannot be distinguished by the TEM-based discrete methods.

4.3 Experimental Background

The deformation was induced to a rectangular parallelepiped nickel single crystal specimen through tungsten carbide wedge indenter with a tip of 90° angle by applying a compressive line load. The line load, which is parallel to the [110] direction of the specimen, was applied quasistatically into (001) surface of the nickel single crystal, where three pairs of slip systems were activated under small scale yielding by maintaining two dimensional plane strain deformation state. The applied load as a function of displacement is shown in Fig. 2.3. The details of the experimental procedure in a broad sense can be found in Chapter 2. The single crystal specimen before and after the deformation including three effective slip systems along with the local crystallographic directions is shown in Fig. 2.4. After the indentation of the specimen of $\sim 160\mu$m, the mid-section of the specimen, which is (220) surface of the specimen, was exposed by Electronic Discharge Machine (EDM). The exposed surface of the

specimen was then mechanically and electrochemically polished to have a surface quality which is necessary to get high accuracy measurements of HR-EBSD.

After mechanical and electrochemical polishing of the single crystal specimen, the lattice rotations were measured by HR-EBSD with spatial resolutions of 2500 nm, 500 nm, and 100 nm. Whereas the in-plane lattice rotations about the x_3-axis, ω_3, are in the range of $-30°$ and $30°$, the out-of-plane lattice rotations, ω_{out}, was measured as zero on the exposed surface of the specimen. The deformation state of the single crystal specimen with local crystallographic and global coordinate frame is presented in Chapter 2. The lattice curvatures were then calculated using lattice rotation measurements. The lattice curvatures are basically the lattice rotation gradients that can be calculated via numerical differentiation of the lattice rotation measurements with respect to the reference coordinate frame. The lattice curvature can be denoted as

$$\kappa_{ij} = \frac{\partial \omega_i}{\partial x_j} \qquad i, j = 1, 2, 3. \tag{4.1}$$

Two non-zero components, which are denoted as κ_{31} and κ_{32} and are defined by Eq. 4.1, were calculated by taking the gradient of the in-plane lattice rotations, ω_3. The other lattice rotations about x_1 and x_2, ω_1 and ω_2, respectively, are zero. The Nye's dislocation density tensor can then be calculated in reference or global coordinate frame using the relation between the Nye's dislocation densities and the lattice curvatures. The relation between these variables can be reduced to

$$\alpha_{ji} \approx -\kappa_{ij} \tag{4.2}$$

by taking into account that the elastic strain gradient is very small under the plane strain deformation state and the finite deformation kinematics. The calculated components of the Nye's dislocation density in global coordinates can be expressed in local crystallographic coordinate frame using the coordinate transformation rules. Finally, the Nye's dislocation

density in local crystallographic frame, $\alpha_{ij}^{'}$, can be expressed as

$$\alpha_{13}' = \alpha_{13}\cos\omega_3 + \alpha_{23}\sin\omega_3, \tag{4.3a}$$

$$\alpha_{23}' = -\alpha_{13}\sin\omega_3 + \alpha_{23}\cos\omega_3. \tag{4.3b}$$

Geometrically necessary dislocations accommodate the lattice curvature and contribute to the work hardening of the material (Gao and Huang [26]). The relationship between the Nye's dislocation density tensor and the GND densities on individual slip systems is given by

$$\alpha_{ij} = \sum_{\alpha=1}^{N} \rho_{gnd}^{(\alpha)} b^{(\alpha)} s_i^{(\alpha)} t_j^{(\alpha)}, \tag{4.4}$$

where $b^{(\alpha)}$ is the magnitude of the Burgers vector, $s^{(\alpha)}$ is the unit vector in the slip direction, and $t^{(\alpha)}$ is the unit tangent vector (Nye [55]; Arsenlis and Parks [7]; Fleck et al. [24]).

The lower bound of geometrically necessary dislocation densities for each effective slip system (*Slip System 1, Slip System 2,* and *Slip System 3*) can now be calculated using the lower bound solution proposed by Kysar et al. [46]. They expressed the Eq. 4.4 in local crystallographic frame for face-centred cubic single crystal as

$$\begin{bmatrix} \alpha_{13}^{'} \\ \alpha_{23}^{'} \end{bmatrix} = \begin{bmatrix} \frac{\sqrt{3}}{4} & \frac{\sqrt{3}}{3} & -\frac{\sqrt{3}}{4} \\ \frac{\sqrt{6}}{4} & 0 & \frac{\sqrt{6}}{4} \end{bmatrix} \begin{bmatrix} \rho_{gnd}^{(1)} b^{(1)} \\ \rho_{gnd}^{(2)} b^{(2)} \\ \rho_{gnd}^{(3)} b^{(3)} \end{bmatrix}.$$

The L^1 minimization scheme was used to calculate the lower bounds of GND densities for individual slip systems. L^1 minimization scheme can be expressed as

$$L^1 = \mid Q_1 \mid + \mid Q_2 \mid + \mid Q_3 \mid, \tag{4.5}$$

where $Q_1 = \rho_{gnd}^{(1)} b^{(1)}$, $Q_2 = \rho_{gnd}^{(2)} b^{(2)}$, and $Q_3 = \rho_{gnd}^{(3)} b^{(3)}$. It can be seen from the Eq. 4.5,

$| Q_1 | + | Q_3 |$ can be defined in terms of Q_2, and the minimization scheme then becomes

$$L^1 = F(Q_2) + | Q_2 | . \tag{4.6}$$

To determine the behavior of the Q_2 along the L^1 minimization scheme, Q_1 and Q_3were calculated in terms of the α'_{23}, α'_{13} and Q_2. The Q_2 quantity was investigated for the cases, where the Q_1 and Q_3 have opposite signs, Q_1 and Q_3 have same signs, and either Q_1 or Q_3 is equal to 0. The minimum of the L^1 function was found by searching for the sign change in the slope of the function. And finally, the minimums of L^1 function were calculated for three different intervals by utilizing the normalized quantities P and R that can be defined as

$$P = \sqrt{3}\left[\frac{\alpha'_{13}}{b} - \left|\frac{\alpha'_{23}}{\sqrt{2}b}\right|\right], \tag{4.7a}$$

$$R = \sqrt{3}\left[\frac{\alpha'_{13}}{b} + \left|\frac{\alpha'_{23}}{\sqrt{2}b}\right|\right]. \tag{4.7b}$$

For the case of $P \leq R < 0$, the lower bounds for GND densities can be expressed as

$$\rho^{(1)}_{gnd} = \frac{2}{\sqrt{3}}\left[\frac{\alpha'_{23}}{\sqrt{2}b} - \left|\frac{\alpha'_{23}}{\sqrt{2}b}\right|\right], \tag{4.8a}$$

$$\rho^{(2)}_{gnd} = \sqrt{3}\left[\frac{\alpha'_{13}}{b} + \left|\frac{\alpha'_{23}}{\sqrt{2}b}\right|\right], \tag{4.8b}$$

$$\rho^{(3)}_{gnd} = \frac{2}{\sqrt{3}}\left[\frac{\alpha'_{23}}{\sqrt{2}b} + \left|\frac{\alpha'_{23}}{\sqrt{2}b}\right|\right]. \tag{4.8c}$$

If $P \leq 0 \leq R$, then the lower bounds for GND densities are given as

$$\rho^{(1)}_{gnd} = \frac{2}{\sqrt{3}}\left[\frac{\alpha'_{23}}{\sqrt{2}b} + \frac{\alpha'_{13}}{b}\right], \tag{4.9a}$$

$$\rho^{(2)}_{gnd} = 0, \tag{4.9b}$$

$$\rho^{(3)}_{gnd} = \frac{2}{\sqrt{3}}\left[\frac{\alpha'_{23}}{\sqrt{2}b} - \frac{\alpha'_{13}}{b}\right]. \tag{4.9c}$$

And if $0 < P \leq R$, then the set of GND densities can be calculated as

$$\rho_{gnd}^{(1)} = \frac{2}{\sqrt{3}} \left[\frac{\alpha'_{23}}{\sqrt{2}b} + \left| \frac{\alpha'_{23}}{\sqrt{2}b} \right| \right], \tag{4.10a}$$

$$\rho_{gnd}^{(2)} = \sqrt{3} \left[\frac{\alpha'_{13}}{b} - \left| \frac{\alpha'_{23}}{\sqrt{2}b} \right| \right], \tag{4.10b}$$

$$\rho_{gnd}^{(3)} = \frac{2}{\sqrt{3}} \left[\frac{\alpha'_{23}}{\sqrt{2}b} - \left| \frac{\alpha'_{23}}{\sqrt{2}b} \right| \right]. \tag{4.10c}$$

The details of the calculation procedures of the GND densities can be found in Kysar et al. [46]. Since the objective of this study is to define a length scale for dislocation substructures, only the final calculation form of GND densities is presented herein.

4.4 Data Collection and Analysis

The GND densities associated with the three effective slip systems, $\rho_{gnd}^{(1)}$, $\rho_{gnd}^{(2)}$ and $\rho_{gnd}^{(3)}$, were measured by utilizing lower bound solution as described in Sec. 4.3. We can now extract the GND densities along the directions of crystallographic traces of the effective slip systems. Chapter 2 and Chapter 3 showed that the activity of effective slip systems, which are activated in a deformed single crystal, can be monitored by using β-fields. The β-fields are contour plots consisting of β-variable, which is essentially the orientation of the net Burgers density vector. The β-fields in this study were obtained for 2500 nm, 500 nm and 100 nm spatial resolutions as shown in Fig. 4.2 to distinguish the GND densities along the slip direction of particular effective slip system. For instance, the right place to collect the $\rho_{gnd}^{(1)}$ is expected to be along the direction of effective *Slip System 1*, of which activity is represented by $\beta = 54.7^\circ$ in the β-field. Similarly, the $\rho_{gnd}^{(2)}$ was extracted along the crystallographic traces, where the *Slip System 2* is activated, and the $\rho_{gnd}^{(3)}$ was extracted along the traces, where the *Slip System 3* is activated. The distance between the data points is 2500 nm in Fig. 4.2(a), which illustrates the traces on the β-field, where GND densities were obtained. Similarly, Fig. 4.2(b) and Fig. 4.2(c) illustrate the data collection paths for 500 nm and 100

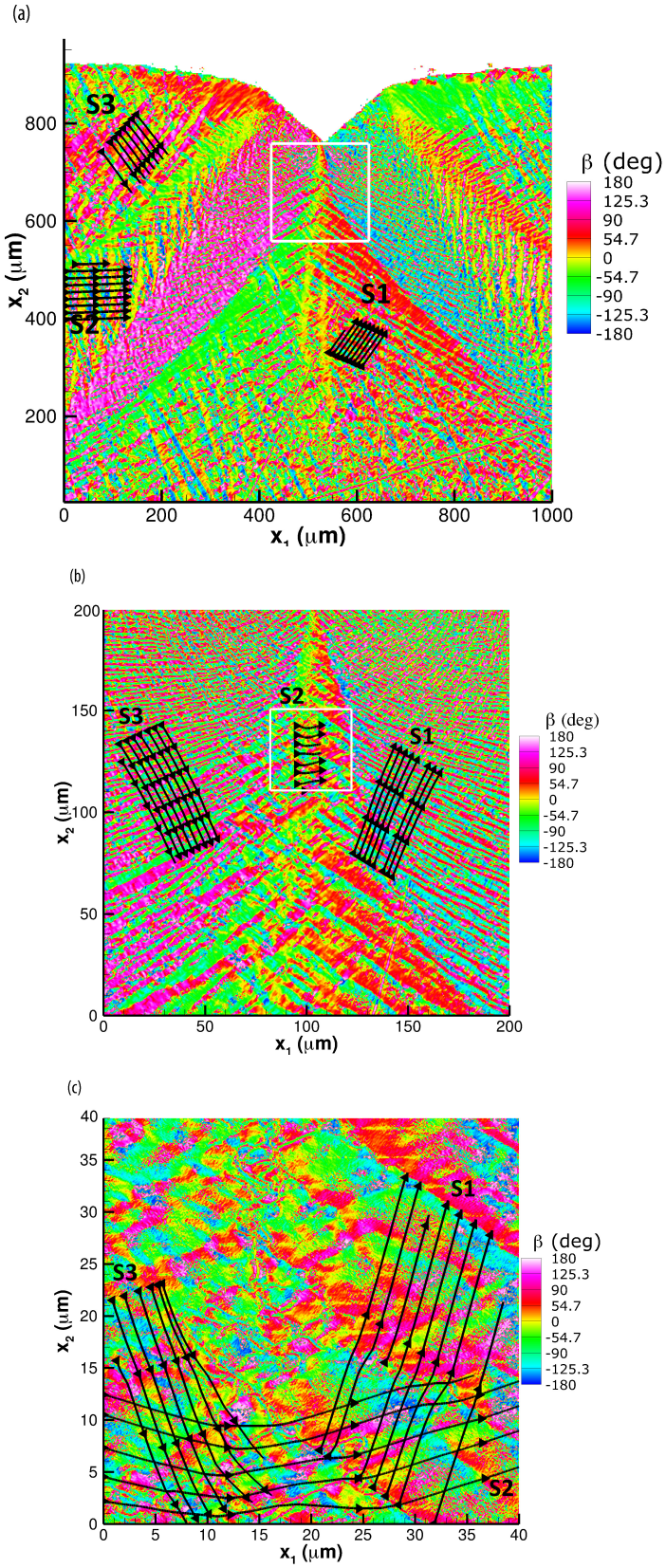

Figure 4.2: As-deformed crystallographic traces, where the GND densities were collected (a): 2500 nm spatial resolution (b): 500 nm spatial resolution (c): 100 nm spatial resolution.

Table 4.1: The extracted data sets associated with the GND densities

Spatial Resolution	Effective Slip System	Extracted GND Density
2500 nm	*Slip System 1*	$\rho_{gnd}^{(1)}$
	Slip System 2	$\rho_{gnd}^{(2)}$
	Slip System 3	$\rho_{gnd}^{(3)}$
500 nm	*Slip System 1*	$\rho_{gnd}^{(1)}$
	Slip System 2	$\rho_{gnd}^{(2)}$
	Slip System 3	$\rho_{gnd}^{(3)}$
100 nm	*Slip System 1*	$\rho_{gnd}^{(1)}$
	Slip System 2	$\rho_{gnd}^{(2)}$
	Slip System 3	$\rho_{gnd}^{(3)}$

nm spatial resolutions, respectively. Fig. 4.2(b) shows a rectangular area of $200\mu m$X$200\mu m$ obtained from Fig. 4.2(a), and Fig. 4.2(c) is a detailed figure depicting the magnification of the rectangular area of $40\mu m$X$40\mu m$ obtained from Fig. 4.2(b). *S1* is the data collection path of the $\rho_{gnd}^{(1)}$ along the as-deformed crystallographic directions of *Slip System 1, S2* is the data collection path of the $\rho_{gnd}^{(2)}$ along the as-deformed crystallographic directions of *Slip System 2,* and *S3* is the data collection path of the $\rho_{gnd}^{(3)}$ along the as-deformed crystallographic directions of *Slip System 3.*

We can now turn our attention to the analysis of the extracted data associated with GND densities along the directions of the effective slip systems. To show the steps of the analysis, a single set of data for $\rho_{gnd}^{(1)}$ obtained along the direction of *Slip System 1* was analyzed as a sample case. The same analysis methodology was repeated for each data set. The data sets were obtained according to the Table 4.1 and β-fields, which are illustrated in Fig. 4.2. The sample data set having 2500 nm spatial resolution was extracted along the as-deformed crystallographic traces of the *Slip System 1* and the GND densities ($\rho_{gnd}^{(1)}$, $\rho_{gnd}^{(2)}$, $\rho_{gnd}^{(3)}$ and total GND density) are illustrated in Fig. 4.3. The GND density patterns revealed a significant information that the dislocation density functions have quasi-periodic arrangements along the slip directions. This enables us to define the dislocation cell parameters using Fourier Methods.

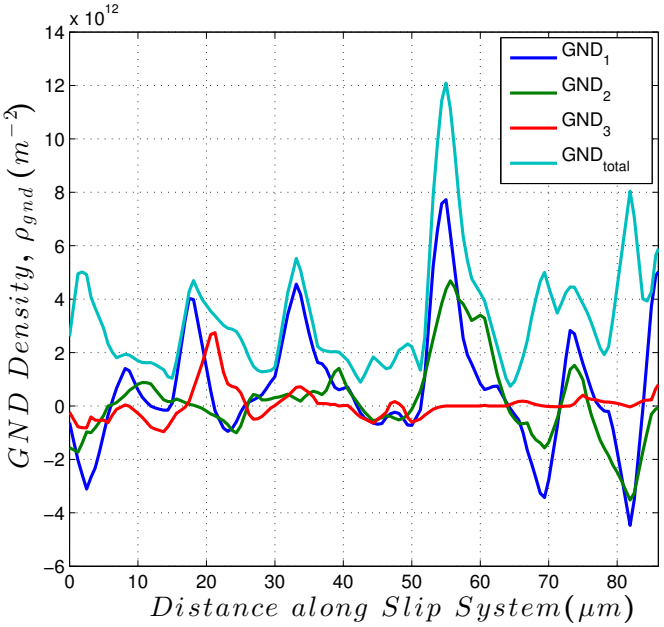

Figure 4.3: Extracted GND densities ($\rho_{gnd}^{(1)}$, $\rho_{gnd}^{(2)}$, $\rho_{gnd}^{(3)}$ and total GND density) along the as-deformed crystallographic direction of the *Slip System 1*. The step size of the data is 2500 nm.

After the extraction of data associated with $\rho_{gnd}^{(1)}$, the GND density function along the slip direction was then truncated properly from both ends to maintain the periodicity of the GND density function. The truncated function was interpolated to maintain the step size (that is, the spatial resolution, and for this case it is 2500 nm) equal to the step size used to obtain data from HR-EBSD. The truncated and interpolated function is shown in Fig. 4.4.

To eliminate the undesired variations on the $\rho_{gnd}^{(1)}$ function, a bandpass filtering process was applied to remove the low and high frequency data from the GND density function. For a few cases low pass filter was also applied. MATLAB commercial software was used in bandpass and lowpass filtering with particular parameters. A graphical user interface was also designed to interactively see the influence of the filtration parameters. The filtration of the $\rho_{gnd}^{(1)}$ function along with the truncation and interpolation is shown in Fig. 4.5. The filtration process is the final step applied to the GND density function before applying the Fourier Methods to define the sizes of the dislocation substructures.

To define the length scale for the dislocation substructures, we introduced a new method

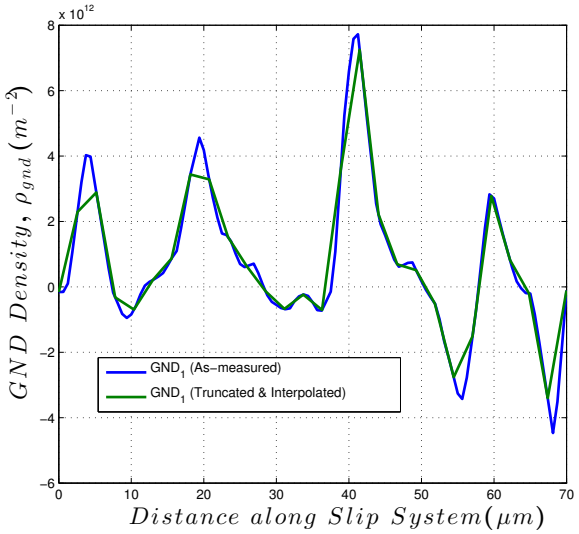

Figure 4.4: Truncation and the interpolation of the $\rho_{gnd}^{(1)}$ along as-deformed crystallographic direction of *Slip System 1.*

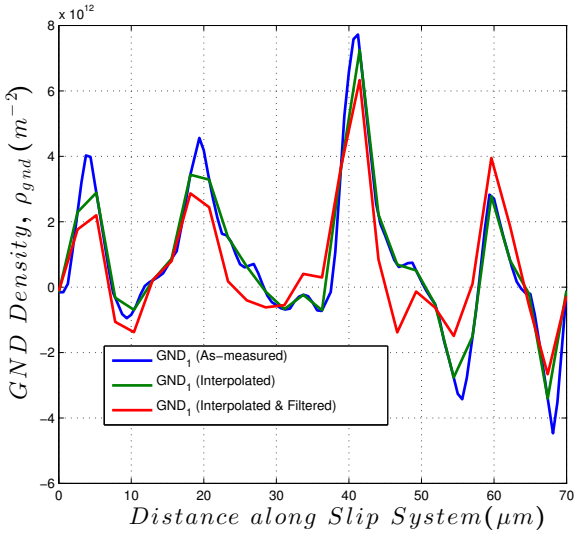

Figure 4.5: Truncation, interpolation, and filtration of the $\rho_{gnd}^{(1)}$ along as-deformed crystallographic direction of *Slip System 1.*

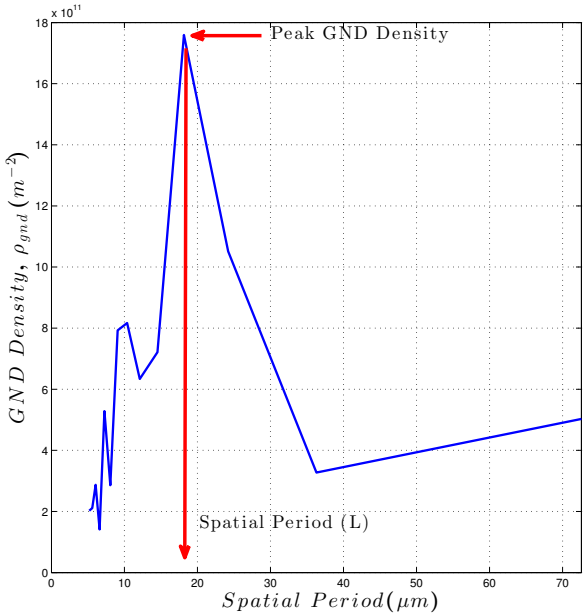

Figure 4.6: Magnitude of the GND density as a function of spatial period

using the quasiperiodic arrangement of the dislocation cell walls, where the dislocation density is mostly concentrated. The quasiperiodicity of the dislocation density by employing the Fourier Transform Methods is the basis of the present study to calculate the dislocation cell size and cell wall width. Fourier Analysis was applied to the filtered GND density function to get the magnitude of the GND density as a function of spatial frequency. The FFT (Fast Fourier Transform) function in MATLAB commercial software was employed to perform the Fourier Analysis. Taking into account the quasiperiodic arrangement of the dislocation density function, the spatial period where the peak GND density found is twice the distance between two dislocation cell walls, which is essentially the dislocation cell size or dislocation mean free path. Therefore, to calculate the dislocation cell size, we used the relationship between the magnitude of the GND density and the spatial period as shown in Fig. 4.6. The peak GND density and the spatial period corresponding to the peak GND density can be easily found as shown in Fig. 4.6. The half of the spatial period calculated here gives the dislocation cell size or cell diameter, and the reciprocal square root of the peak GND density gives the dislocation spacing.

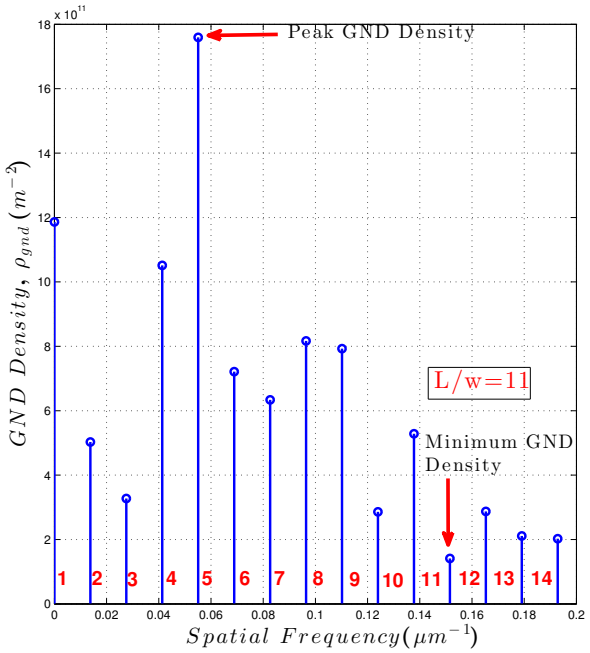

Figure 4.7: Magnitude of the GND density as a function of spatial frequency

To calculate the dislocation cell wall width, or the thickness of the dislocation cell wall, the analogy with the periodic functions was employed. The relationship between the spatial period and the pulse width of a periodic function was investigated to find the similar relationship between the spatial period of the GND density function and the dislocation cell wall width. To determine this kind of relationship, two periodic functions that show similar pattern with the GND density functions in our data sets, were taken. The first function was rectangular pulse having a spatial period of L and a pulse width of w as shown in Fig. 4.8a. The function is symmetric about $y-$axis so that it is an even function. Fourier coefficients of this rectangular function were calculated to plot its power spectral density as a function of spatial frequency as illustrated in Fig. 4.8b. While the Fourier coefficient A_n, is a *sine function* containing the $\frac{w}{L}$ term, the other Fourier coefficients, namely B_n and A_0 were calculated as zero. Therefore, the power spectral density is basically determined by coefficient A_n. Consequently, it was found that the number of intervals between the zeros of the power spectral density function is equal to the ratio between the spatial period and pulse width,

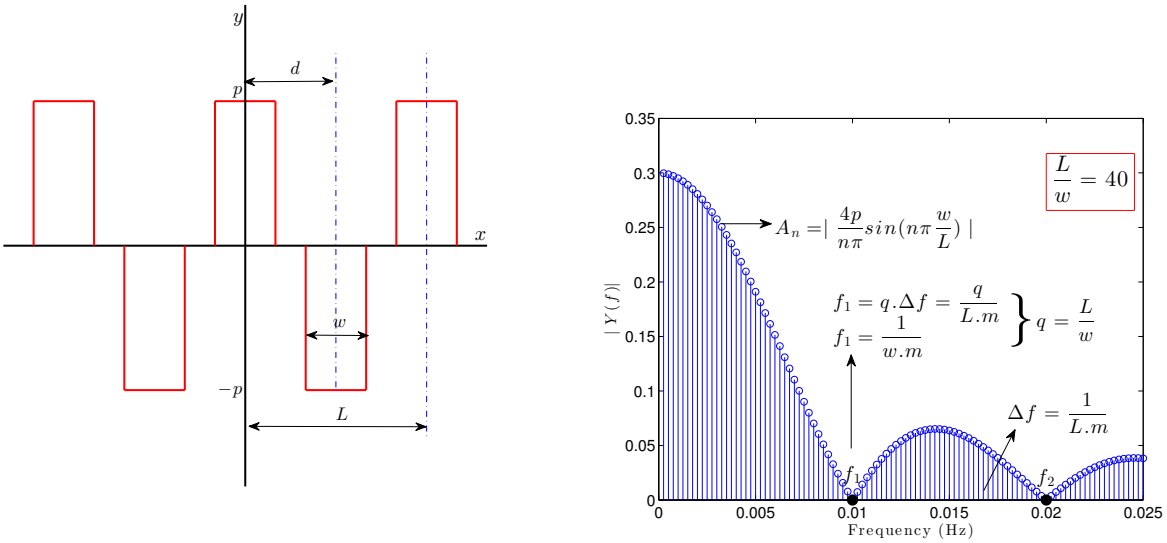

(a) (b)

Figure 4.8: (a):A rectangular periodic function, where L is the spatial period, w is the pulse width, and p is the maximum value of function $y(x)$, (b):Fourier Transform of this rectangular periodic function for $L/w = 40$ and calculation of the parameters, where f_1 and f_2 are the zeros of $\mid Y(f) \mid = \mid A_n \mid$, $q = L/w$ is the number of frequency intervals and Δf is the frequency interval. (The plot is generated for $m = 100$, $w = 1$, $p = 3$ and $L = 40$.)

which is given by $\frac{L}{w}$. The similar analysis was applied to an even triangular pulse having a spatial period of L and a pulse width of w. Similar results were observed for triangular periodic function. By using the analogy described here for the periodic functions, we can find the ratio of spatial period to cell wall width when we assume the minimum GND density to be the zero of the power spectral density in our case. The number of intervals between initial frequency, which is $f_1 = 0$, and the frequency at min GND density found, gives the ratio between the spatial period and the dislocation cell wall width, which is denoted by q and expressed as $\frac{L}{w}$. As can be seen in the Fig. 4.7, the ratio q is found as 11. By using the fact that the spatial period is twice the dislocation cell size, we can finally express the relationship between the spatial period, dislocation cell size and dislocation cell wall width as

$$d = \frac{L}{2} = \frac{qw}{2}, \tag{4.11}$$

where L is the spatial period, d is the dislocation cell size, w is the dislocation cell wall width, and q is the number of intervals between $f_1 = 0$ and the frequency at min GND density found. Therefore, for the value of q=11 calculated here using Fourier Analysis, the cell wall width is calculated as $w = \frac{2d}{q} \cong 0.18d$. The process explained here in detail is repeated for other data sets associated with the GND density functions. After the calculation of the sizes of dislocation substructures, which are d and w, the next step is to define a length scale for these variables.

4.5 Results and Discussion

The data sets associated with each GND density were processed according to the procedure described in Sec. 4.4. The dislocation cell sizes and peak GND densities obtained from the Fourier Analysis were plotted in logarithmic scale as shown in Fig. 4.9. It can be seen in Fig. 4.9 that the peak GND densities change in the range of 10^{12} and 10^{15} m^{-2}, and the

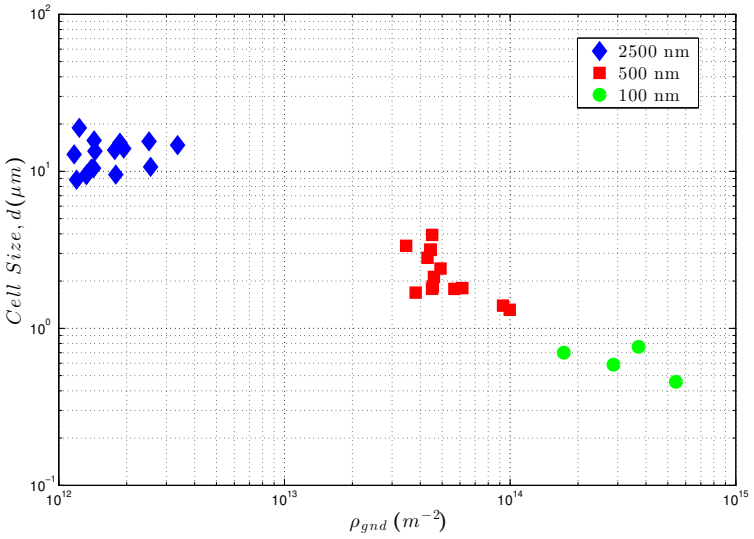

Figure 4.9: The variation of the dislocation cell size (d) with peak GND densities obtained from Fourier Analysis

calculated cell sizes for the GND densities of 2500 nm spatial resolution are larger than those of 500 nm and 100 nm spatial resolution. This analysis is a basis for the relationship between the dislocation cell size and the dislocation spacing.

To define a relationship between the dislocation spacing and the dislocation cell size, the reciprocal square root of the peak GND densities were calculated. The variation of the dislocation cell size with the calculated reciprocal square root of GND densities, or dislocation spacing is shown in Fig.4.10. It can be seen from the graph that there is a linear relationship between these variables with a linear constant of approximately 16. The maximum calculated dislocation cell size is 19 μm, and the reciprocal square root of the GND densities is in the range of 0 and 1 μm. The present study proved the relationship of $d = K \cdot \rho^{-1/2}$, where K was calculated as 16. This constant was compared with the linear constants obtained via TEM micrographs for Nickel by Staker and Holt [67] and Koneva et al. [40]. The analysis shows that the linear constant, K, calculated in the present study using SEM-based continuum methods and Fourier methods is consistent with the results obtained by Staker and Holt [67] and Koneva et al. [40].

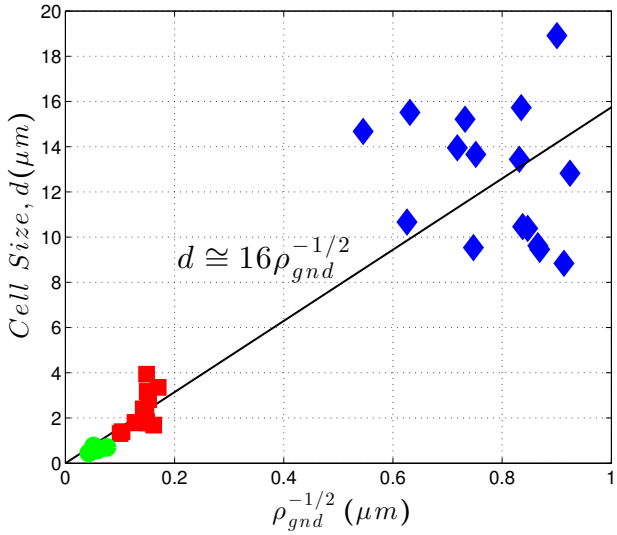

Figure 4.10: The variation of Dislocation Cell Size with Dislocation Spacing, $\rho_{gnd}^{-1/2}$

In the present study, finally, a length scale was developed between the dislocation cell size and the dislocation cell wall width, which were calculated using Fourier Analysis and plotted to find a relationship between them as illustrated in Fig. 4.11. A linear relationship with a slope of 0.16 was determined between the dislocation cell wall width and the dislocation cell size. The result was compared to those obtained by Knoesen and Kritzinger [38] and Koneva et al. [40]. The linear constant found in the present study is consistent with the results presented by the studies, where Knoesen and Kritzinger [38] found 0.19 for pure Copper, and Koneva et al. [40] found the similar results for the Nickel Single Crystal as discussed in Sec. 4.2.

4.6 Conclusions

A length scale was investigated for the dislocation substructures (dislocation cells and dislocation cell boundaries) using SEM-based continuum methods and Fourier Transform under the extremely high strain conditions induced by a compressive line load through a wedge indenter. A quasi-periodic arrangement of dislocation substructures was observed on the

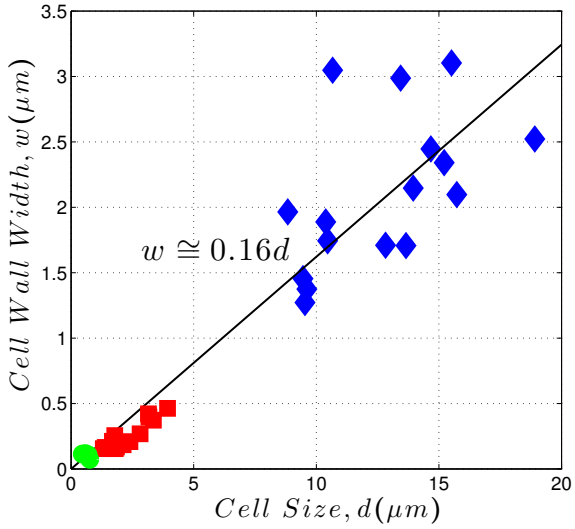

Figure 4.11: Dislocation Cell Wall Width(w) as a function of Dislocation Cell Size(d)

surface of deformed Nickel Single Crystal. The spatial period of the dislocation density function, the dislocation cell size and dislocation cell wall width were calculated using Fourier Transform, and the relationships between these variables were investigated. The dislocation cell size was found to be proportional to the reciprocal square root of dislocation density, and a linear relationship, which is expressed as $d = 16\rho_{gnd}^{-1/2}$, was obtained from the data sets. The dislocation cell wall width was found to be 16% of the dislocation cell size, or dislocation mean free path. These results support the results obtained through TEM-based discrete methods. It is concluded that whereas TEM-based discrete methods characterize the dislocation densities only in a small length scale, the SEM-based continuum method used in the present study is ideal for multiscale characterization. The present study show that the dislocation densities can be distinguished between different slip systems.

Chapter 5

Conclusions and Future Work

Experimental methods currently in use aim to define the elastic-plastic constitutive behavior of a material in terms of stress vs. strain, force vs. displacement, torsion vs. twist and moment vs. curvature relations. These methods are insufficient to completely characterize the deformed state of the material. In this thesis, a new parameter (β) has been introduced to validate the existing constitutive models. The β-variable is the orientation angle of the net Burgers density vector, obtained as the net signed dislocations per enclosed area.

Spatially resolved net Burgers density vector fields and corresponding characteristic length scales have been obtained by introducing a new validation parameter, β. The analysis presented in Chapters 2 through 4 gives direct information about the state of a single crystal undergoing extreme plastic deformation. The study presented herein gives a full description of the deformation state of the material in light of the spatially resolved net Burgers density vector (magnitude and direction) fields and the spatially resolved defect densities. In particular, the deformation state of a nickel single crystal has been investigated. The experimental procedure and the single crystal plasticity simulations are detailed in Chapter 2.

The net Burgers density vector and its orientation (β) are defined and derived analytically in Chapter 2, by employing the elastic incompatibility equation and Nye's dislocation density tensor. The relationships between the β-variable and characteristic slip orientation

angles are also presented. Spatially resolved net Burgers density vector fields (β-fields) have been determined by employing the spatial gradient of the in-plane lattice rotations that were measured in the range of [-30°+30°]. The out-of-plane lattice orientations were measured as zero on the deformed surface. The measurements were taken by High Resolution Electron Backscatter Diffraction method. Experimentally obtained β-fields are the contour maps having a color scheme that corresponds to the characteristic slip angles. The regions that are separated from each other by the colors represent the activity regions of the slip systems. A two dimensional median filtering and Fast Fourier Transform were applied to the experimentally obtained β-fields to remove the high spatial frequency variations that represent the discreteness of the material.

Single crystal plasticity simulations were performed by using two different hardening models representing the hardening stages of the FCC single crystal during deformation. The hardening relations and parameters are defined in Chapter 2. The β-fields have been determined through finite element simulations that serve as a benchmark against experimentally determined β-fields. The hardening models employed in the finite element simulations are called Pierce Asaro Needleman (PAN) and Bassani and Wu (BW). PAN Simulation #6, in which $q = 1.4$, $\tau_s/\tau_0 = 5$, $h_0/\tau_0 = 10$ and Simulation #7, in which $q = 1.6$, $\tau_s/\tau_0 = 5$, $h_0/\tau_0 = 10$ give consistent results with experimentally obtained β-fields. BW Simulation #5, in which $q = 0$, $\tau_s/\tau_0 = 1.24$, $h_0/\tau_0 = 0.7$, $h_s/\tau_0 = 38.7$, $\gamma_0 = 0.001$, $f_0 = 7.2$ and Simulation #6, in which $q = 0$, $\tau_s/\tau_0 = 1.3$, $h_0/\tau_0 = 1.5$, $h_s/\tau_0 = 90$, $\gamma_0 = 0.001$, $f_0 = 7.2$ give consistent results with experimentally obtained β-fields. The directions of the net Burgers density vectors were inserted to the β-fields for experimental and simulation cases. In order to get finer information about the state of the material, an analysis was performed to extract β-variable along the 90-degree arc-lengths. The filtered experimental β-variable was compared to the β-variable obtained from finite element simulations after the extraction of the data along the 90-degree arc lengths. The results are consistent for arcs C_3 and C_4 whose radii are 2.5 and 3.0, respectively, times the indentation depth.

A parametric study was carried out in Chapter 3, as a follow-up study, to investigate the effects of hardening parameters on the β-variable and β-fields. The effect of the β-variable on β-fields was monitored along the 90-degree arc lengths. This study demonstrates that the latent hardening ratio has no significant effect on the β-variable and β-fields; however, there is a small change observed in the deformed region near the indenter tip. Small plastic deformations occur in the region where $\theta = -20^{\circ}$. The β-variable and β-fields depend on the initial hardening modulus and saturation strength. A change in the initial hardening modulus causes a shift in the boundary of the slip activity regions. The saturation strength has a significant effect on the β-variable and β-fields. As the saturation strength varies, both the magnitude of the β-variable and the boundaries of the slip activity regions change.

The parametric study also includes a finer analysis that was performed to get detailed information about the deformation state of the material, by monitoring the variations of the plastic strains and plastic slip rates along the 90-degree arc lengths. The plastic strains and plastic slip rates were obtained from finite element simulations that utilize PAN and BW hardening models. Since the β-fields obtained from PAN Simulations#6-7 and BW Simulations#5-6 are consistent with the β-field obtained from experiment, variations of the plastic strains and plastic slip rates were compared for these simulations. The plastic strain variations were evaluated to find the activity regions of the slip systems. A thorough comparison of the slip activity regions shows that whereas a double slip is activated in the first activity region obtained from BW Simulations, a single slip is activated in the same region obtained from PAN Simulations.

The third and last analysis performed in the parametric study consists of monitoring the stress variations along 90-degree arc lengths to obtain the stress space. In order to determine the elastic-plastic behavior of the material, the yield surfaces were constructed for each arc length. The overall elastic-plastic behavior can be monitored by successive yield surface analyses associated with each arc length. A newly introduced ten-degree analysis was also performed to capture the state of the material data point. This analysis enables one to

get direct information about the state of the material data point by employing the stress space. The activity of the slip systems is assessed by examining data points located 10° apart from each other on the arc-lengths. The activity mapping analysis was also performed as a complementary slip activity analysis. The parametric analysis outlined in Chapter 3 indicates that the β-variable can be used as a validation parameter in elastic-plastic constitutive models.

A length scale has been defined for dislocation structures using Fourier Analysis and GND measurements to establish a link between the dislocation structures and macroscopic deformation fields. Dislocation cell size, dislocation cell width have been calculated by considering the quasi-periodic arrangement of dislocations. The study presented in Chapter 4 shows that there is a linear relationship between the dislocation cell size and the dislocation spacing. The dislocation cell size is found to be 16 times the dislocation spacing. The result was compared with the TEM micrograph result, and a consistency was observed. The maximum dislocation cell size has been calculated as 20μm, which is an order of magnitude larger than the cell size obtained by TEM micrographs. A linear relationship has also been determined between the dislocation cell size and dislocation cell wall width. The dislocation cell wall width is found to be 16% of the dislocation cell size. This result is also consistent with the result obtained by TEM micrographs of well-formed dislocation cells. The study also reveals that whereas TEM micrographs characterize dislocation on very small scale, the method presented in Chapter 4 enables the multi scale characterization.

The studies outlined in Chapters 2 through 4 show that the β-variable can be used as a validation parameter for elastic-plastic constitutive models. The spatially resolved net Burgers density vector fields have been obtained for FCC nickel single crystal. The new validation parameter can also be applied to BCC single crystal to obtain the spatially resolved net Burgers density vector fields, β-fields, to get direct information about the state of the material by monitoring the activity of the slip systems. As a future work, the analyses outlined in this thesis can also be applied to the materials deformed by tensile or compressive

loading at high temperatures in order to completely determine the elactic-plastic behavior of the material.

Bibliography

[1] R. K. Abu Al-Rub, G. Z. Voyiadjis, and D. J. Bammann. A thermodynamic based higher-order gradient theory for size dependent plasticity. *International Journal of Solids and Structures*, 44(9):2888–2923, 2007.

[2] A. Acharya and A. Roy. Size effects and idealized dislocation microstructure at small scales: Predictions of a phenomenological model of mesoscopic field dislocation mechanics: Part i. *Journal of the Mechanics and Physics of Solids*, 54(8):1687–1710, 2006.

[3] A. Acharya, A. Beaudoin, and R. Miller. New perspectives in plasticity theory: Dislocation nucleation, waves, and partial continuity of plastic strain rate. *Mathematics and Mechanics of Solids*, 13(3–4):292–315, 2008.

[4] B. L. Adams. Orientation imaging microscopy: Emerging and future applications. *Ultramicroscopy*, 67(1–4):11–17, 1997.

[5] E. C. Aifantis. The physics of plastic-deformation. *International Journal of Plasticity*, 3(3):211–247, 1987.

[6] L. Anand, M. E. Gurtin, S. P. Lele, and C. Gething. A one-dimensional theory of strain-gradient plasticity: Formulation, analysis, numerical results. *Journal of the Mechanics and Physics of Solids*, 53(8):1789–1826, 2005.

[7] A. Arsenlis and D. M. Parks. Crystallographic aspects of geometrically-necessary and statistically-stored dislocation density. *Acta Materialia*, 47(5):1597–1611, 1999.

[8] R. J. Asaro. Micromechanics of crystals and polycrystals. *Advances in Applied Micromechanics*, 23:1–114, 1983.

[9] M. Atkinson. Further analysis of the size effect in indentation hardness tests of some metals. *Journal of Materials Research*, 10(11):2908–2915, 1995.

[10] J. L. Bassani and T. Y. Wu. Latent hardening in single crystal ii: Analytical characterization and predictions. *Proceedings of the Royal Society of London Series A*, 435 (1893):21–41, 1991.

[11] C. J. Bayley, W. A. M. Brekelmans, and M. G. D. Geers. A comparison of dislocation induced back stress formulations in strain gradient crystal plasticity. *International Journal of Solids and Structures*, 43(24):7268–7286, 2006.

[12] M. R. Begley and J. W. Hutchinson. The mechanics of size-dependent indentation. *Journal of the Mechanics and Physics of Solids*, 46(10):2049–2068, 1998.

[13] U. Borg. Strain gradient crystal plasticity effects on flow localization. *International Journal of Plasticity*, 23(8):1400–1416, 2007.

[14] J. D. Clayton, D. L. McDowell, and D. J. Bammann. A multiscale gradient theory for single crystalline elastoviscoplasticity. *International Journal of Engineering Science*, 42 (5-6):427–457, 2004.

[15] A. M. Cuitino and M. Ortiz. Three-dimensional crack-tip fields in four-point-bending copper single-crystal specimens. *Journal of the Mechanics and Physics of Solids*, 44(6): 863–899, 901–904, 1996.

[16] C.F.O. Dahlberg, Y. Saito, M. S. Oztop, and J. W. Kysar. Geometrically necessary dislocation density measurements associated with different angles of indentations. *International Journal of Plasticity*, 54:81–95, 2014.

[17] A. D. Darbal, K.J. Ganesh, X. Liu, S.-B. Lee, J. Ledonne, T. Sun, B. Yao, A.P. Warren, G.S. Rohrer, A.D. Rollett, P.J. Ferreira, K.R. Coffey, and K. Barmak. Grain boundary character distribution of nanocrystalline cu thin films using stereological analysis of transmission electron microscope orientation maps. *Microscopy and Microanalysis*, 19: 111–119, 2013.

[18] M. S. De Guzman, G. Neubauer, P. Flinn, and W.D. Nix. The role of indentation depth on the measured hardness of materials. *Materials Research Society Symposium Proceedings*, 308:613–618, 1993.

[19] L. P. Evers, W. A. M. Brekelmans, and M. G. D. Geers. Non-local crystal plasticity model with intrinsic SSD and GND effects. *Journal of the Mechanics and Physics of Solids*, 52(10):2379–2401, 2004.

[20] N. A. Fleck and J. W. Hutchinson. A reformulation of strain gradient plasticity. *Journal of the Mechanics and Physics of Solids*, 49(10):2245–2271, 2001.

[21] N. A. Fleck and J. R. Willis. A mathematical basis for strain-gradient plasticity theory–Part I: Scalar plastic multiplier. *Journal of the Mechanics and Physics of Solids*, 57(1): 161–177, 2009.

[22] N. A. Fleck and J. R. Willis. A mathematical basis for strain-gradient plasticity theory. Part II: Tensorial plastic multiplier. *Journal of the Mechanics and Physics of Solids*, 57 (7):1045–1057, 2009.

[23] N. A. Fleck, G. M. Muller, M. F. Ashby, and J. W. Hutchinson. Strain gradient plasticity - Theory and experiment. *Acta Metallurgica et Materialia*, 42(2):475–487, 1994.

[24] N. A. Fleck, M. F. Ashby, and J. W. Hutchinson. The role of geometrically necessary dislocations in giving material strengthening. *Scripta Materialia*, 48:179–183, 2003.

[25] P. Franciosi, M. Berveiller, and A. Zaoui. Latent hardening in copper and aluminum single crystals. *Acta Metallurgica*, 28:273–283, 1980.

[26] H. Gao and Y. Huang. Geometrically necessary dislocation and size dependent plasticity. *Scripta Materialia*, 48:113–118, 2003.

[27] H. Gao, Y. Huang, W. D. Nix, and J. W. Hutchinson. Mechanism-based strain gradient plasticity-I. Theory. *Journal of the Mechanics and Physics of Solids*, 47(6):1239–1263, 1999.

[28] D. Griffiths and J. N. Riley. Dislocation arrangements in deformed polycrystalline 3 *Acta Metallurgica*, 14:755–773, 1966.

[29] P. Gudmundson. A unified treatment of strain gradient plasticity. *Journal of the Mechanics and Physics of Solids*, 52(6):1379–1406, 2004.

[30] M. E. Gurtin. A gradient theory of single-crystal viscoplasticity that accounts for geometrically necessary dislocations. *Journal of the Mechanics and Physics of Solids*, 50 (1):5–32, 2002.

[31] M. E. Gurtin. A finite-deformation, gradient theory of single-crystal plasticity with free energy dependent on densities of geometrically necessary dislocations. *International Journal of Plasticity*, 24(4):702–725, 2008.

[32] M. E. Gurtin, L. Anand, and S. P. Lele. Gradient single-crystal plasticity with free energy dependent on dislocation densities. *Journal of the Mechanics and Physics of Solids*, 55(9):1853–1878, 2007.

[33] C. S. Han, H. Gao, Y. Huang, and W. D. Nix. Mechanism-based strain gradient crystal plasticity - I. Theory. *Journal of the Mechanics and Physics of Solids*, 53(5):1188–1203, 2005.

[34] R. Hill. Generalized constitutive relations for incremental deformation of metals crystals by multislip. *Journal of the Mechanics and Physics of Solids*, 14:95–102, 1966.

[35] J. P. Hirth and J. Lothe. *Theory of Dislocations*. Krieger Publishing Company, Malabar, Florida, 1992.

[36] D. L. Holt. Dislocation cell formation in metals. *Journal of Applied Physics*, 41(8): 3197–3201, 1970.

[37] Y. Huang. A user-material subroutine incorporating single crystal plasticity in the abaqus finite element program: Mech. report 178. Technical report, Division of Engineering and Applied Sciences, Harvard University, Cambridge, Massachusetts, 1991.

[38] D. Knoesen and S. Kritzinger. Dislocation cell boundary widths and dislocation cell sizes in deformed copper. *Acta Metallurgica*, 30:1219–1222, 1982.

[39] U. F. Kocks. The relation between polycrystal deformation and single-crystal deformation. *Metallurgical and Materials Transactions*, 1:1121–1143, 1970.

[40] N. A. Koneva, V. A. Starenchenko, D. V. Lychagin, L. I. Trishkina, N. A. Popova, and E. V. Kozlov. Formation of dislocation cell substructure in face-centred cubic metallic solid solutions. *Materials Science and Engineering A*, 483-484:179–183, 2008.

[41] D. Kuhlmann-Wilsdorf. A critical test on theories of work-hardening for the case of drawn iron wire. *Metallurgical Transactions*, 1(11):3173–3179, 1970.

[42] M. Kuroda and V. Tvergaard. A finite deformation theory of higher-order gradient crystal plasticity. *Journal of the Mechanics and Physics of Solids*, 56(8):2573–2584, 2008.

[43] J. W. Kysar. Addendum to "a user-material subroutine incorporating single crystal plasticity in the abaqus finite element program: Mech. report 178". Technical report,

Division of Engineering and Applied Sciences, Harvard University, Cambridge, Massachusetts, 1997.

[44] J. W. Kysar. Continuum simulations of directional dependence of crack growth along a copper/sapphire bicrystal interface: Part i: Experiments and crystal plasticity background. *Journal of the Mechanics and Physics of Solids*, 49(5):1099–1128, 2001.

[45] J. W. Kysar, Y. X. Gan, and G. Mendez-Arzuza. Cylindrical void in a rigid-ideally plastic single crystal i: Anisotropic slip line theory solution for face-centered cubic crystals. *International Journal of Plasticity*, 21(8):1481–1520, 2005.

[46] J. W. Kysar, Y. Saito, M. S. Oztop, D. Lee, and W.T. Huh. Experimental lower bounds on geometrically necessary dislocation density. *International Journal of Plasticity*, 26 (8):1097–1123, 2010.

[47] G. Langford and M. Cohen. *Trans. Am. Soc. Metals*, 62:623, 1969.

[48] Q. Ma and D. R. Clarke. Size-dependent hardness of silver single-crystals. *Journal of Materials Research*, 10(4):853–863, 1995.

[49] K. W. McElhaney, J. J. Vlassak, and W. D. Nix. Determination of indenter tip geometry and indentation contact area for depth-sensing indentation experiments. *Journal of Materials Research*, 13(5):1300–1306, 1998.

[50] S. Dj. Mesarovic. Energy, configurational forces and characteristic lengths associated with the continuum description of geometrically necessary dislocations. *International Journal of Plasticity*, 21(10):1855–1889, 2005.

[51] E. Moin and L. E. Murr. Interactive effects of shock loading parameters on the substructure and mechanical properties of nickel and stainless steel. *Materials Science and Engineering*, 37:249–269, 1979.

[52] L. E. Murr. Work hardening and the pressure dependence of dislocation density and arrangements in shock loaded nickel and copper. *Scripta Metallurgica*, 12:201–206, 1978.

[53] C. F. Niordson. On higher-order boundary conditions at elastic-plastic boundaries in strain-gradient plasticity. *Philosophical Magazine*, 88(30–32):3731–3745, 2008.

[54] C. F. Niordson and J. W. Hutchinson. On lower order strain gradient plasticity theories. *European Journal of Mechanics A-Solids*, 22(6):771–778, 2003.

[55] J. F. Nye. Some geometrical relations in dislocation solids. *Acta Metallurgica*, 1(2): 153–162, 1953.

[56] T. Ohashi. Crystal plasticity analysis of dislocation emission from micro voids. *International Journal of Plasticity*, 21(11):2071–2088, 2005.

[57] T. Ohashi, M. Kawamukai, and H. Zbib. A multiscale approach for modeling scale-dependent yield stress in polycrystalline metals. *International Journal of Plasticity*, 23 (5):897–914, 2007.

[58] M. S. Oztop, J. W. Kysar, and C. F. Niordson. Length-scale effect due to periodic variation of geometrically necessary dislocation densities. *Internatinal Journal of Plasticity*, 41(1):189–201, 2013.

[59] D. Peirce, R.J. Asaro, and A. Needleman. Material rate dependence and localised deformation in crystalline solids. *Acta Metallurgica*, 31(12):1951–1976, 1983.

[60] G. R. Piercy, R.W. Cahn, and A. H. Cottrell. A study of primary and conjugate slip in crystals of alpha-brass. *Acta Metallurgica*, 3:331–338, 1955.

[61] W. J. Poole, M. F. Ashby, and N. A. Fleck. Micro-hardness of annealed and work-hardened copper polycrystals. *Scripta Materialia*, 34(4):559–564, 1996.

[62] J. E. Pratt. Dislocation substructure in strain-cycled copper as influenced by temperature. *Acta Metallurgica*, 15:319–327, 1967.

[63] J. R. Rice. Plane strain slip line theory for anisotropic rigid-plastic materials. *Journal of the Mechanics and Physics of Solids*, 21:63–74, 1973.

[64] J. R. Rice. Tensile crack tip fields in elastic-ideally plastic crystals. *Mechanics of Materials*, 6(4):317–335, 1987.

[65] A. Roy and A. Acharya. Size effects and idealized dislocation microstructure at small scales: Predictions of a phenomenological model of mesoscopic field dislocation mechanics: Part ii. *Journal of the Mechanics and Physics of Solids*, 54(8):1711–1743, 2006.

[66] Suresh S., Nieh T. G., and Choi B.W. Scr Mater 1999;41:951. Nanoindentation of copper thin films on silicon substrates. *Scripta Materialia*, 41(9):951–957, 1999.

[67] M. R. Staker and D. L. Holt. The dislocation cell size and dislocation density in copper deformed at temperatures between 25 and 700c. *Acta Metallurgica*, 20:569–579, 1972.

[68] N. A. Stelmashenko, Brown Walls, M.G., L. M., and Yu. V. Milman. Microindentations on w and mo oriented single crystals: An stm study. *Acta Metallurgica et Materialia*, 41(10):2855–2865, 1993.

[69] J. S. Stölken and A. G. Evans. A microbend test method for measuring the plasticity length scale. *Acta Materialia*, 46(14):5109–5115, 1998.

[70] T. Y. Wu, J. L. Bassani, and Laird C. Latent hardening in single crystals i: Theory and experiments. *Proceedings of the Royal Society of London Series A*, 435(1893):1–19, 1991.